

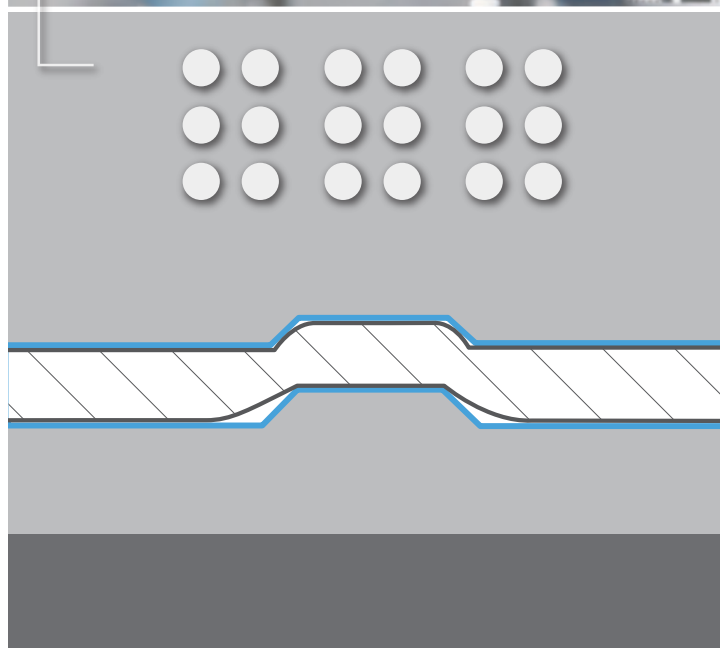
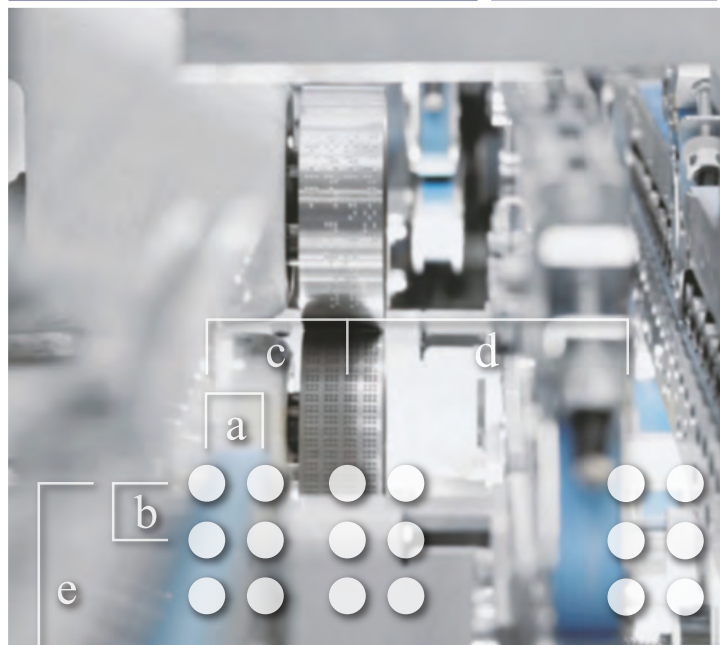


University of Novi Sad
Faculty of Technical Sciences
DEPARTMENT OF GRAPHIC
ENGINEERING AND DESIGN

Volume **12**
Number **4**
December **2021**

JGED

JOURNAL OF GRAPHIC
ENGINEERING AND DESIGN

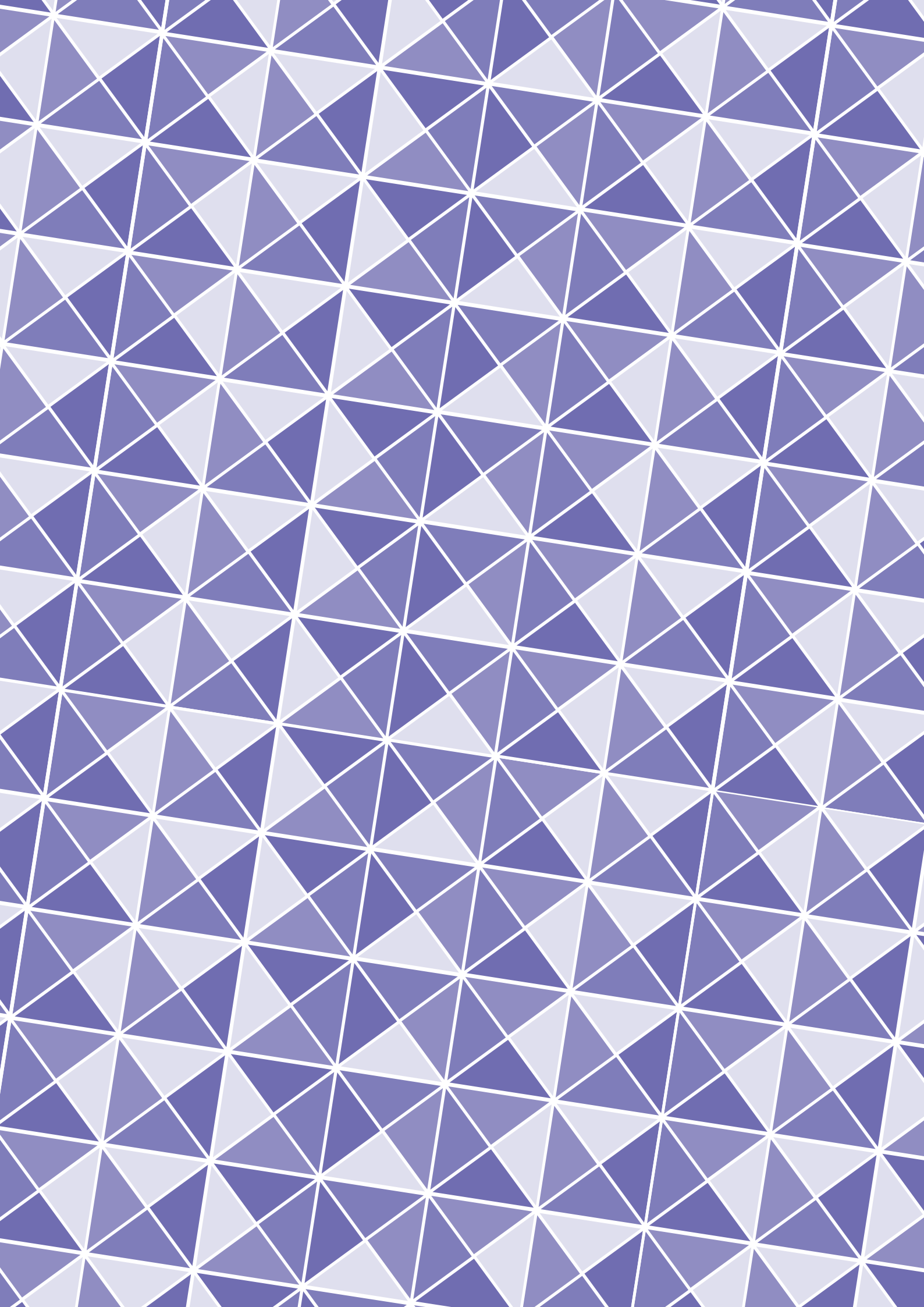


Use and analysis of UV varnish
printed braille information on
commercial packaging products
Slaven Miloš, Đorđe Vujčić, Igor Majnarić

Statistical evaluation of a Color
Managed Digital Printing Workflow
(CMDPW) consistency [4th C of CMW]
Haji Naik Dharavath

Influence of packaging design parameters
on customers' decision-making process
Minja Malešević, Mladen Stančić

Per-pixel displacement mapping using
cone tracing with correct silhouette
Adnane Ouazzani Chahdi, Anouar Ragragui,
Akram Halli, Khalid Satori



JGED

JOURNAL OF GRAPHIC
ENGINEERING AND DESIGN

4/2021

Volume 12, Number 4, December 2021.

Published by

UNIVERSITY OF NOVI SAD, SERBIA
Faculty of Technical Sciences
Department of Graphic Engineering and Design

PUBLISHED BY



University of Novi Sad
Faculty of Technical Sciences

DEPARTMENT OF GRAPHIC
ENGINEERING AND DESIGN

Address:

Faculty of Technical Sciences,
Department of Graphic
Engineering and Design,

Trg Dositeja Obradovića 6
21000 Novi Sad, Serbia

Telephone numbers:

+381 21 485 26 20
+381 21 485 26 26
+381 21 485 26 21

Fax number:

+381 21 485 25 45

Email:

jged@uns.ac.rs

Web address:

www.grid.uns.ac.rs/jged

Frequency: 4 issues per year

Printing: Faculty of Technical Sciences,
Department of Graphic Engineering and Design

Circulation: 200

Electronic version of journal available on
www.grid.uns.ac.rs/jged

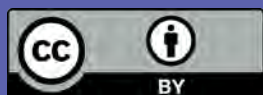
E-ISSN 2217-9860

The journal is abstracted/indexed
in the Scopus and Directory of Open Access Journals



CIP - Katalogizacija u publikaciji
Biblioteka Matice srpske, Novi Sad
655

JGED : Journal of Graphic Engineering and Design /
editor Dragoljub Novaković. - Vol. 1, No. 1 (nov. 2010) -
Sciences, Department of Graphic Engineering and
Design,
2010-. 30 cm
Dva puta godišnje
ISSN 2217-379X
COBISS.SR-ID 257662727



© 2021 Authors. Published by the University of Novi Sad, Faculty of
Technical Sciences, Department of Graphic Engineering and Design. All
articles are an open access articles distributed under the terms and con-
ditions of the Creative Commons Attribution license 3.0 Serbia (<http://creativecommons.org/licenses/by/3.0/rs/>).

EDITORS

Dragoljub Novaković, University of Novi Sad, Novi Sad, Serbia

Nemanja Kašiković, University of Novi Sad, Novi Sad, Serbia

EDITORIAL BOARD

Thomas Hoffmann-Walbeck

HDM Stuttgart, Stuttgart, Germany

Rafael Huertas

University of Granada, Granada, Spain

Joanna Ewa Izdebska

Warsaw University of Technology, Warsaw, Poland

Igor Majnarić

University of Zagreb, Zagreb, Croatia

Branko Milosavljević

University of Novi Sad, Novi Sad, Serbia

Raša Urbas

University of Ljubljana, Ljubljana, Slovenia

László Koltai

Óbuda University, Budapest, Hungary

Anastasios E. Politis

Hellenic Union of Graphic Arts and Media Technology Engineers-
HELGRAMED, Athens, Greece

Miljana Prica

University of Novi Sad, Novi Sad, Serbia

Iskren Spiridonov

University of Chemical Technology and Metallurgy,
Sofia, Bulgaria

Mladen Stančić

University of Banja Luka, Banja Luka, Bosnia and Herzegovina

Tomáš Syrový

University of Pardubice, Pardubice, Czech Republic

Gojko Vladić

University of Novi Sad, Novi Sad, Serbia

Thomas Sabu

Mahatma Gandhi University, Kottayam, India

Jonas Malinauskas

Vilnius College of Technologies and Design, Vilnius, Lithuania

Roberto Pašić

UKLO University St. Climent Ohridski, Bitola, North Macedonia

Behudin Mešić

SCION, Rotorua, New Zealand

Arif Özcan

Marmara University, Istanbul, Turkey

Vladan Končar

ENSAIT, Roubaix, France

Catarina Silva

Polytechnic Institute of Cávado and Ave (IPCA), Barcelos, Portugal

Michal Čeppan

Slovak University of Technology in Bratislava, Slovakia

Tim C Claypole

Swansea University, Swansea, United Kingdom

Alexandra Pekarovicova

Western Michigan University, Kalamazoo, USA

Panagiotis Kyratsis

University of Western Macedonia, Kozani, Greece

Jason Lisi

Ryerson University, Toronto, Canada

Peter Nussbaum

Norwegian University of Science and Technology, Gjøvik, Norway

Igor Karlovits

Pulp and paper institute, Ljubljana, Slovenia

Art Director

Uroš Nedeljković

Layout design

Bojan Banjanin

Journal cover design

Nada Miketić

JOURNAL OF GRAPHIC ENGINEERING AND DESIGN

Volume 12, Number 4, December 2021.

Contents

- | | | | |
|----|--|----|--|
| 5 | Use and analysis of UV varnish printed braille information on commercial packaging products
<i>Slaven Miloš, Đorđe Vujčić, Igor Majnarić</i> | 33 | Influence of packaging design parameters on customers' decision-making process
<i>Minja Malešević, Mladen Stančić</i> |
| 17 | Statistical evaluation of a Color Managed Digital Printing Workflow (CMDPW) consistency [4th C of CMW]
<i>Haji Naik Dharavath</i> | 39 | Per-pixel displacement mapping using cone tracing with correct silhouette
<i>Adhane Ouazzani Chahdi, Anouar Ragraoui, Akram Halli, Khalid Satori</i> |




Use and analysis of UV varnish printed braille information on commercial packaging products

ABSTRACT

This paper investigates the possibility of reproducing Braille by UV ink-jet printing on self-adhesive labels, previously printed by flexo printing technology. The aim was to determine whether it is possible to reproduce Braille, the degree of quality of created Braille dots (cells), the legibility of Braille text, and how many layers of varnish are necessary for quality reproduction. The Braille letter was applied to the previously printed label (design) using 8, 10, 12, 14 and 16 layers of varnish. It has been found that it is possible to reproduce a quality and legible Braille. With the increase in the number of layers, the assessment of legibility and quality of reproduction by the respondents also increased. Samples reproduced with 12 layers of varnish received a very good grade of legibility and good grade for quality of Braille. Samples reproduced with 8 and 10 layers received bad grades for legibility, and even worse for quality, while samples with a higher number of layers of varnish, 14 and 16, received even better grades. The threshold for quality reproduction would therefore be the use of 12 layers of varnish, where a good ratio of workmanship and economy is obtained.

KEY WORDS

Braille printing, UV ink-jet, UV varnish, blind, vision impairment

Slaven Miloš¹ 
Đorđe Vujčić² 
Igor Majnarić¹ 

¹ University of Zagreb,
Faculty of Graphic Arts, Graphic
engineering, Zagreb, Croatia

² University of Banja Luka,
Faculty of Technology, Graphic
engineering, Banja Luka,
Bosnia and Herzegovina

Corresponding author:

Đorđe Vujčić

e-mail: djordje.vujcic@tf.unibl.org

First received: 29.6.2021.

Revised: 19.8.2021.

Accepted: 25.8.2021.

Introduction

Based on statistical data, it can be concluded that visual impairment is a significant health problem (Pascolini & Mariotti, 2011; Hashemi et al., 2017; WHO, 2019). It is estimated that at least 2.2 billion people worldwide have some level of visual impairment, including blindness. According to statistics from 2015, 36 million people worldwide are blind (visual acuity worse than 3/60),

217 million have moderate or severe vision impairment (worse than 6/18, but equal to or better than 3/60) and 189 million have mild vision impairment (worse than 6/12, but equal to or better than 6/18)¹. It is estimated that 1.8 billion people have near vision impairment (Bourne et al., 2017; Fricke et al., 2018; WHO, 2019). In percentage 3.44% of people have distance vision impairment (0.49% are blind and 2.95% have moderate or severe vision impairment) (Ackland, Resnikoff & Bourne, 2017).

¹Visual acuity

Visual acuity is a simple, non-invasive measure of the ability of the visual system to distinguish two points of high contrast in space (WHO, 2019).

Distance visual acuity is usually assessed using a vision chart at a certain distance (usually 6 meters (or 20 feet)). The smallest line read on the chart is written as a fraction, where the counter refers to the distance from which the chart is observed, and the denominator is the distance at which the "healthy" eye is able to read that line on the chart. For example, visual acuity 6/18 means that at 6 meters from the vision chart a person can read a letter that someone with normal vision could see at 18 meters. "Normal" vision is considered to be 6/6 (WHO, 2019).

Near visual acuity is measured according to the smallest print size that a person can notice at a given test distance. In a population survey, near-visual impairment is usually classified as a near visual acuity less than N6 or m 0.8 at 40 centimeters, with N referring to the print size based on the point system used in the printing industry, and 6 is the font size equivalent to the newspaper print (WHO, 2019).

Estimates show that there are more than 30 million blind and partially sighted people in geographical Europe. On average, 1 in 30 Europeans faces vision loss. Trends in Europe also show that women are more susceptible to visual impairment than men and that vision loss is closely linked to aging (one in three citizens over the age of 65 faces vision loss; 90% of people with visual impairment are over the age of 65) (EBU, 2019).

It is very important to provide blind and partially sighted people with an environment in which they will feel safe and have access to the necessary information. This can, among other things, be achieved by labelling products in Braille (Havenko et al., 2013). According to the European Directive 2004/27/EC (European Commission, 2005), labelling of pharmaceutical products has been mandatory since 2005, but it is expected that in the near future it will be mandatory to label a larger number of consumer products: food products, products for personal hygiene and care, products for space hygiene, etc. In some countries, Braille product labelling has already been extended to some other product categories, in addition to pharmaceutical products.

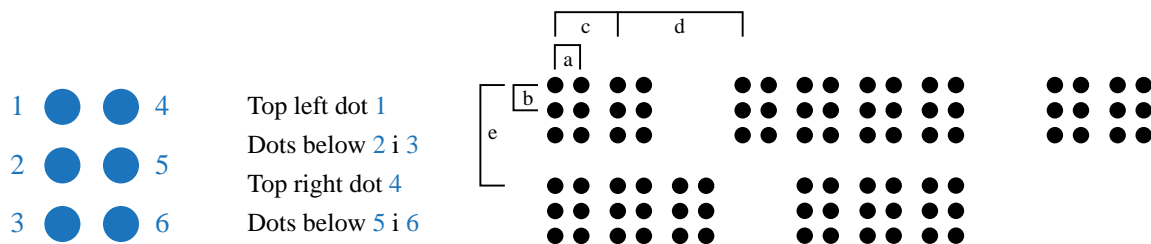
Braille is a universally accepted tactile reading and writing system for the blind and visually impaired (European Commission, 2005; Royal Blind, 2019). Frenchman Louise Braille, who went blind in the third year of his life, invented Braille in 1825, and it was named after him (European Commission, 2005; VisionAware, 2019). It can be said that Braille is a code that can be used to read and write in many languages (American Foundation for the Blind, 2019; European Commission, 2005; Royal Blind, 2019). It enables literacy and gives an individual the opportunity to become acquainted with spelling, punctuation, paragraph and other formatting rules (Royal Blind, 2019). It is a system that consists of raised dots, which are read tactilely, by crossing a finger over them (American Foundation for the Blind, 2019). One complete cell of Braille consists of six raised dots placed in two parallel vertical columns, three dots in each (it looks like the number 6 on the dice). Each dot is assigned a number from 1 to 6. Thus, the upper left dot is assigned the number 1, dots below 2 and 3, the upper right dot number 4, and dots below 5 and 6 (Figure 1a) (American Foundation for the Blind, 2019; European Commission, 2005; Royal Blind, 2019; PharmaBraille, 2019a).

64 different combinations can be obtained by placing one or more dots in different positions. One cell of a Braille can denote an alphabet letter, a number, a punctuation mark, a mathematical sign, a musical or computer notation, etc. (American Foundation for the Blind, 2019; European Commission, 2005; Royal Blind, 2019; PharmaBraille, 2019a).

A large number of countries that produce Braille, especially great ones, have developed their own standards. These standards define the spaces between the character of the Braille and the minimum height of the dots in each cell of the Braille (Tiresias, 2008). The Marburg Medium Braille standard has been specially created for use on pharmaceutical packaging and labels (Tiresias, 2008; PharmaBraille, 2019b). It is recommended by European and North American standards for pharmaceutical packaging and labels. Below are the specifications (Figure 1b) according to the Marburg Medium Braille standard (PharmaBraille, 2019b):

- The dot diameter is 1.3 – 1.6 mm.
- The dot spacing is 2.5 mm from dot centre to dot centre (a; b).
- The character spacing is 6.0 mm from dot centre to dot centre (c).
- The cell spacing from dot centre to dot centre with single space between is 12.0 mm (d).
- The line spacing is 10.0 mm (e).

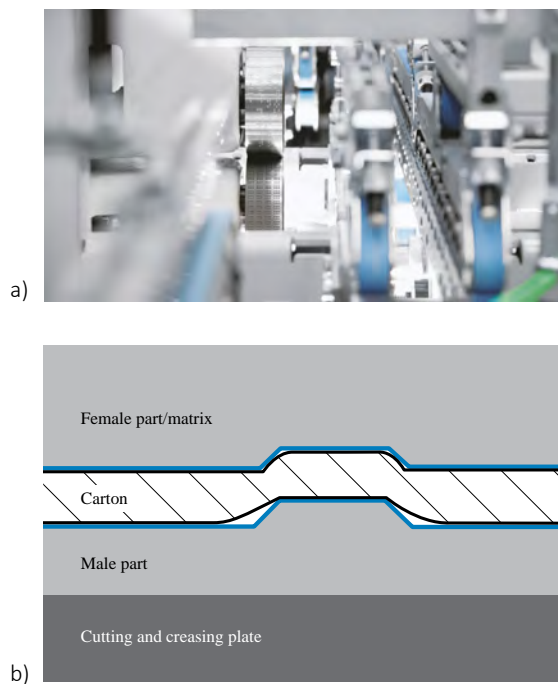
The Marburg Medium standard does not define the height of dots in Braille. The CEN standard for pharmaceutical packaging suggests a target dot height of 0.20 mm, for embossing of the material (PharmaBraille, 2019b). A 2008 study (Douglas, Weston & Whittaker, 2008) concluded that in the range of heights from 0.06 to 0.23 mm, the adequate height of raised Braille dots is 0.18 mm (67% of participants definitely recognize the text, and 27% probably), but there is a problem that at this height the surface of the cardboard bursts (Douglas, Weston & Whittaker, 2008; Golob, Rotar & Šulc, 2011; Golob et al., 2013). Furthermore, the ECMA Euro Braille standard, in addition to the defined values for spacing between dots, characters and lines, which are identical to the Marburg Medium standard, defines a dot diameter of 1.3 mm and a target dot height of 0.5 mm (PharmaBraille, 2019b).



» **Figure 1:** Position of dots within Braille cell (a) and spacing dimensions (b) (ECMA, 2008)

Until recently, in order to print Braille, it was necessary to prepare a special embossing matrix for each industrial print. With the progress in the field of screen printing, the possibility of applying varnish and creating dots appeared. For each printing it is necessary to prepare a new screen mesh. With the development of digital printing, great changes and improvements are taking place. The printing form of this technique is in digital format. Since digital printing has replaced screen printing in many fields, and since it also enables application of varnish on the substrate, it is quite logical to ask whether it is possible to print Braille with this technique (Jowat, 2019).

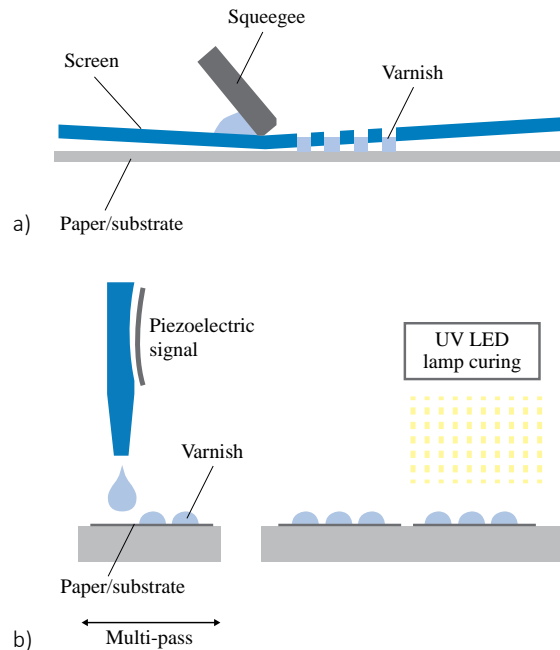
Braille is usually formed on the packaging by embossing. It can be done on a printing machine, a cutting machine, and sometimes on a gluing machine (Figure 2). This procedure is standard for the production of packaging for pharmaceutical products, and in addition it is possible to use labels printed by ink-jet or screen printing technique. The Braille formed on the labels is stronger and more stable compared to the embossed Braille, where the dots may collapse during transport, and also the problem may be to achieve the required dot height (Golob et al., 2013).



» **Figure 2:** Braille embossing segment on cardboard packaging gluing machine (a) and diagram of Braille dot embossing process and cardboard deformation (BOBST, 2021; ECMA, 2008)

By analyzing scientific publications and patents Havenko et al. (2013) provided a classification of available methods for Braille dot formation (Yim, 1996; Burman & Lofstedt, 2001; Labetska, 2012; Kibirskitis, Venyte & Lydekaityte, 2012; Labetska & Havenko, 2012). They can be divided into two groups, namely contact and non-contact methods (Havenko et al., 2013). Contact methods

include embossing on cardboard, special types of paper and films and screen printing (Figure 3a) on special papers with thick layers of non-flowing color or mixture, creating relief in the plane due to thermal imprint. And, non-contact methods include ink-jet printing using special composition varnish (Figure 3b) and methods for obtaining a relief imprint using polymers or other thermochemical materials on electrophotographic printers.



» **Figure 3:** Screen printing Braille process (a) and UV ink-jet Braille printing (b)

If the existing printing market is analyzed, there are two main methods for creating Braille dots. With the first method, dots are obtained by embossing and it is widely used due to lower costs and faster production. However, this method has significant disadvantages in terms of achieving the appropriate height of Braille dots, as well as their mechanical strength. Since mechanical strength of dots is often not appropriate, it leads to a decrease in the height of the dots during transport or during reading by blind or partially sighted people. Another method of creating Braille dots is the screen printing technique. Its main advantage is the possibility of printing on various materials, such as paper, cardboard, foils, etc. Also, the relief obtained by this printing technique is mechanically more stable and less susceptible to deformation during transport or use by blind and partially sighted persons (Havenko et al., 2013).

When it comes to the reproduction of tactile imprints on self-adhesive labels, there is a problem of creating Braille using the embossing technique. As an alternative, there is the possibility of forming Braille dots using varnish. This can be done by the screen printing technique, but there is a question whether the reproduction by the digital printing technique is possible, as well as

how many layers of varnish would be needed. Some research has proven the possibility of creating Braille dots using the UV ink-jet printing technique (Golob, Rotar & Šulc, 2011; Golob et al., 2013; Klisarić, Novaković & Milić, 2013; Golob et al., 2014; Urbas et al., 2016). In one study, certain technical aspects of the Braille dots reproduction on self-adhesive labels with this printing technique were examined (Havenko et al., 2013). There is still little and insufficient research on the reproduction of Braille dots using the UV ink-jet printing technique on self-adhesive labels. The aim of this paper is to determine whether it is possible to reproduce a Braille dot of appropriate shape and dimensions, with how many layers of varnish and whether blind people can use it.

Digital printing is becoming more and more common, and with this technology it is also possible to form relief, and thus Braille dots on various substrates, including self-adhesive labels. A wide range of materials can be printed using digital ink-jet printing with the use of highly viscous, transparent UV varnish. Important elements in creating Braille dots with ink-jet printing, which affect the size and shape of the Braille dot, are the viscosity of the varnish and the surface stresses of the printing substrate. The quality of digitally printed Braille on various substrates, including self-adhesive labels, depends on numerous factors such as the physical and mechanical characteristics of the substrate and the varnish used, the temperature and pressure of the varnish, the feed rate of the printing substrate, etc. All these factors should be investigated in detail in order to obtain quality tactile imprints using the digital ink-jet printing technique (McCallum & Ungar, 2003; Creagh & McDonald, 2003; McCallum et al., 2005; Havenko et al., 2013).

A layer of UV varnish is applied to the substrate by spraying through small nozzles. Liquid varnish is transferred directly to the substrate by spraying, and hardens under the influence of UV light. The drops of varnish are small, usually 6 pL, and are fixed by the radiation of the LED light source. Considering the method of application on the substrate, and drying, non-absorbent printing substrates can also be printed (the drying process is instantaneous) (Majnarić, Bolanča Mirković & Golubović, 2012). Also, therefore, it is possible to apply several layers in the same position. This is important when forming a relief print. If after applying the ink or varnish in one layer, the height is not appropriate, the number of layers can be increased and desired height

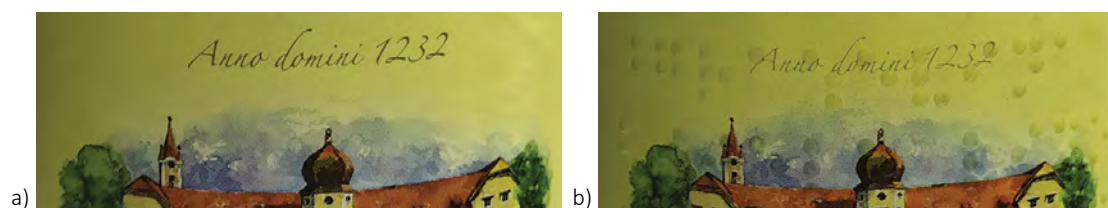
can be achieved (Schär et al., 2015). This allows you to print Braille. It represents a special type of use of structured varnish, and it has expanded to the creative field. For instance, raised elements are used to create illustrations in books for the blind and partially sighted, then for inscriptions in museums and galleries, as well as for descriptive labels (Eccles, 2014; Schär et al., 2015).

By reproducing Braille with ink-jet technology, the problem of deformation and bursting of the material is eliminated, and the information in Braille can be applied to a much wider range of materials. The Braille formed on the labels is stronger and more stable compared to the Braille obtained by embossing, where the dots may collapse during transport, and also the problem may be to achieve the required dot height (Golob et al., 2013). Considering the transparency of UV varnish, the text in Braille created with this technique does not affect people who have normal vision, when detecting printed information.

Materials and methods

This paper examines the legibility of tactile imprints formed by UV varnish on printing machine VersaUV LEC 300 (Roland DG Corporation, Japan, 2011) on ScandCoat MC self-adhesive label paper. Unlike other research, Braille was applied to previously printed material (label). The label was printed using the flexographic printing technique on the Nilpeter FA-4 machine (Nilpeter A/S, Denmark 2015). An actual design was printed. The ink printing order was CMYK. The part of the label on which the Braille was applied was previously printed with 40% yellow colour. UV curing Flint Flexocure UFR 10082 ink was used for printing. The aim was to determine whether it is possible to reproduce a quality and legible Braille using the UV printing technique on self-adhesive paper, in order to be able to label products for blind and partially sighted people. Also, the goal was to determine how many layers of varnish are optimal for obtaining a satisfactory quality in terms of height and size of Braille dots, and their legibility. Below is more information about the used paper, the method for reproduction of the prints, as well as the method for their evaluation.

The inscription in Braille was as follows: graševina bijelo vino berba 2013. Figure 4 shows an enlarged photograph of part of the label before and after the printing of the Braille text.



» **Figure 4:** Printed self-adhesive label (a) and label with printed Braille text using 12 layers of varnish (b)

Printing substrate

ScandCoat MC is a machine coated paper, with medium gloss and good whiteness. It is a versatile paper, suitable for a very wide range of primary label work. It is suitable for colour printing, with different printing techniques: flexography, rotary or flat-bed letterpress, offset lithography, screen printing process and can be foil blocked and varnished. It is important to note that it is suitable for use in food packaging, with limited contact with food, as well as in packaging for products intended for children.

Material characterization was performed according to the following parameters: calliper (ISO 534), basis weight (ISO 536), roughness (ISO 8791-4), brightness (ISO 2470) and opacity (ISO 2471). The characteristics of the used self-adhesive label paper are given in Table 1. The data are taken from the paper manufacturer datasheet.

UV varnish and Braille printing process on samples

In order to form Braille dots, liquid UV varnish was transferred directly to the printing substrate, in this case a printed label, and then cured with UV light. ECO-UV varnish, EUV-GL v.4, the following compositions were used (Roland, 2019): 1,6-Hexamethylene diacrylate 20-30%, 2-Methoxyethyl acrylate 20-24%, Benzyl acrylate 10-25%, N-Vinyl caprolactam 10- 20% and Diphenyl (2,4,6-trimethylbenzoyl) phosphine oxide 5- 10%. The printing was done in 8, 10, 12, 14 and 16 layers, in order to achieve the appropriate height of the relief. Gloss mode (drying with one UV lamp) was used for printing. The print resolution was 740 x 1440 dpi. The direction of printing was set to unidirection, and rasterization was done according to the dither method. Printing was done in high quality mode- higher amount of varnish and resolution, and lower speed. It is printed using a DX4 Epson piezo Inkjet head with dot size of 3.5 pL (Format Media Ltd., 2010). After 5 layers, the height of the head was changed to a higher level.

Instrumental measurements

An electro-mechanical surface roughness tester - perthometer S8P (MAHR PERTHEM, Germany 1988) was used (Figure 5). The test was performed in accordance with ISO standard 3274/75. The device was used to determine the profile of the Braille dot reproduced with different number of layers, as well as its diameter.

Table 1

Characteristics of used self-adhesive label paper

Paper type	Thickness μm (ISO 534)	Basis weight g/m^2 (ISO 536)	Roughness μm (ISO 8791-4)	Brightness % (ISO 2470)	Opacity % (ISO 2471)
ScandCoat MC	65 \pm 5	80 \pm 3	1	93	89

The height of the Braille dots was measured using an electronic micrometer, with a division of 0.01 mm. The micrometer used has a larger contact head, and it covered three dots at the same time. The height of the Braille dots was measured 10 times at different positions. Height was measured along with paper thickness. Then, by subtracting the thickness of the paper, the height of the formed Braille dots was obtained and an average of 10 measurements was taken.



» **Figure 5:** Perthometer S8P

Blind and partially sighted people survey

The survey was conducted among blind and partially sighted people in the Association of the Blind of the Zagreb City and at the High School for the Blind and Visually Impaired "Vinko Bek". The survey involved 24 respondents, of different ages and genders, different levels of education, as well as different experience in knowing and using Braille.

Twelve men and twelve women took part in the survey. 5 respondents are under 20 years of age, 3 respondents are aged 21-30 years, 1 respondent is 31-40 years old, 4 respondents are 41-50 years old, 8 respondents are 51-60 years old, and 3 respondents are over 60 years old. 17 of them have a secondary education, while 7 of them have a university degree. 9 respondents have used Braille for less than 20 years, 10 of them between 21-40 years, while 5 of them have known Braille for more than 40 years.

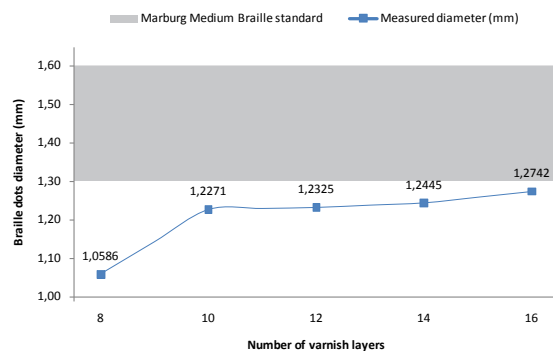
The samples were evaluated according to the quality of the Braille dots (cells), i.e. the height of the Braille dots

and their tangibility, and the legibility of the Braille text. Both criteria were evaluated with grades from 1 to 5, where the scale looked like this: 1- insufficient legibility, 2- sufficient legibility, 3- good legibility, 4- very good legibility, 5- excellent legibility, i.e. to assess the quality of the sample: 1- insufficient quality, 2- sufficient quality, 3- good quality, 4- very good quality and 5- excellent quality.

Results and discussion

Results of instrumental measurements

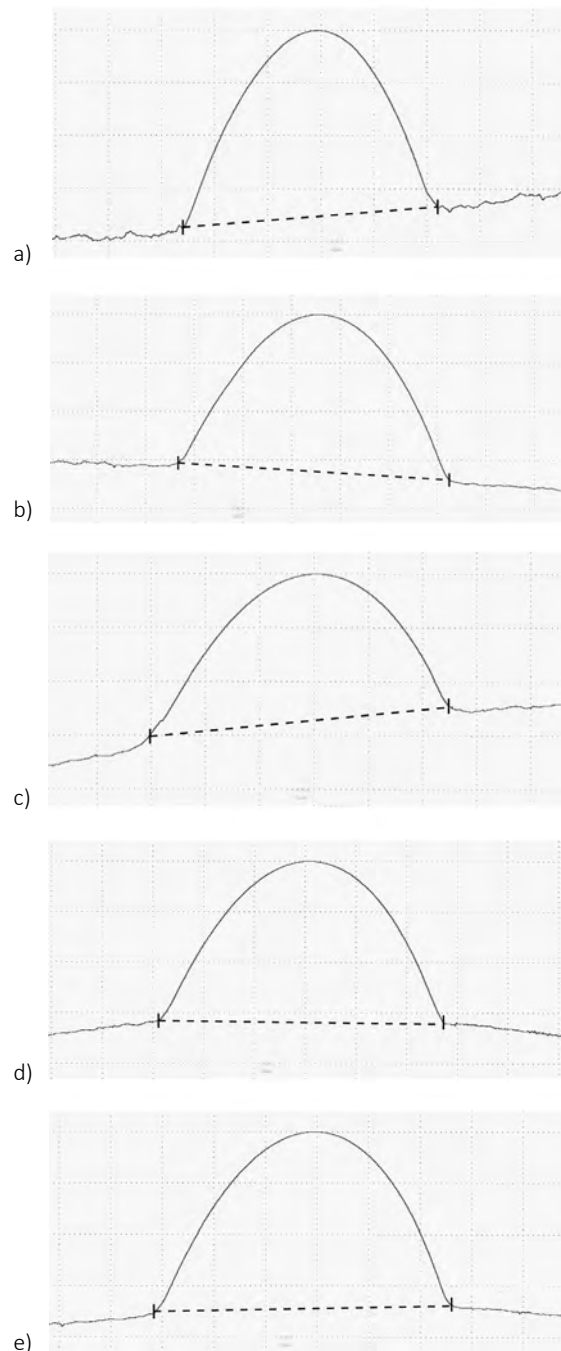
Figure 6 presents the obtained results of the diameter of reproduced dots for five samples, in which the number of varnish layers was successively increased. As can be seen from the figure, the diameter of Braille dots in all samples is below the standard value. When reproducing Braille dots using 8 layers of varnish, the diameter of the dot is the smallest. As the number of layers increases, the diameter of the dot also increases. It can be noticed that the change of the diameter is greatest between prints reproduced with 8 and 10 layers, while with further increasing the number of layers of varnish, the diameter of the dot slightly increases. Thus, it can be concluded that first application of UV varnish leads to the partial penetration of the varnish into the paper and the spreading of the Braille dot around its base. After, the surface of the paper is covered with polymerized UV varnish, and the next layers of varnish are applied to the given surface. Spreading of the varnish is reduced, and depends on amount of varnish that flows over the edges of previously polymerized layer. After applying 10 layers of UV varnish, spreading is reduced to minimum, since amount of applied varnish slightly flows over the edges of polymerized layers.



» **Figure 6:** Diameter of Braille dots reproduced with different number of layers of varnish

Figure 7 presents the profiles of Braille dots formed by a different number of layers of varnish, obtained using a S8P perthometer. From the presented profiles it can be noticed that the shape of the formed dots is domed and

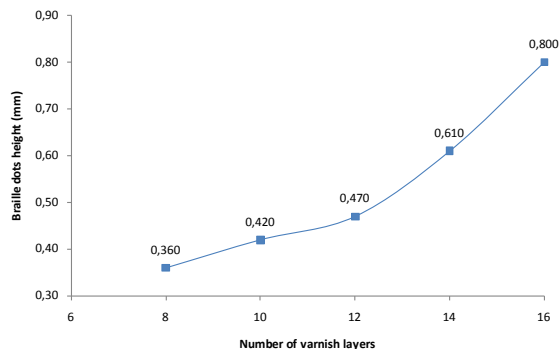
that the peak of the dot is approximately in its centre. The dot is slightly rounded at the top. There is impression of a dot that is comfortable under the fingers, but raised enough, that it can be tactilely felt and recognized.



» **Figure 7:** Braille dot profile printed with 8 (a), 10 (b), 12 (c), 14 (d) and 16 layers of varnish (e) measured with perthometer S8P

Figure 8 presents the obtained results of the dots height. Two parts of the curve trend can be seen from the figure. In the first part, from 8 to 12 layers of varnish, the increase is almost linear. The difference between 8 and 10 layers of varnish, as well as 10 and 12 is approximately the same. In the first case it is 0.06

mm, while in the second it is 0.05 mm. Further, an exponential increase in the height of the dot is observed. The difference in height increases successively, thus the difference between 12 and 14 layers of varnish is 0.14 mm, and between 14 and 16 coats 0.19 mm.



» **Figure 8:** Height of Braille dots reproduced with different number of layers of varnish

Based on the above, it can be concluded that at first there is a slightly larger increase in the diameter of the dot, i.e. spreading of the varnish during application, and a smaller increase in the height of the dot. With further application of layers of varnish, the diameter of the dot remains approximately the same, but the height of the dot shows a larger increase. Therefore, there is less spreading of varnish around the dot base, and thus the height of the dot increases. This can be explained by contact angle. According to Urbas et al. (2016), contact angle was smaller in case of unprinted surface than the surface covered with polymerized UV varnish. It can also be observed that the height of the dot in the sample with 12 layers of varnish is approximately equal to the target height of 0.5 mm, suggested by the ECMA Euro Braille standard.

Results of blind and partially sighted people survey

Table 2 presents the average values of assessments of the quality of Braille dots, and their legibility, by 24 respondents. When assessing the quality of the reproduction, the respondents were asked to arrange the reproduced samples with Braille from the worst to the best, depending on the quality of the Braille dots, i.e. the height of the Braille dots and their tangibility. In the legibility assessment, the subjects received the samples

in random order, without knowing that the samples were formed by a different number of layers of varnish, and had to give a legibility rating for each sample in the range of 1- 5, where grade 1 was insufficient legibility, and grade 5 excellent legibility. It can be seen from the table that the grades for both quality and legibility increase with increasing the number of varnish layers.

The average grade for quality of Braille dots reproduced with 8 layers of varnish is 1.04, and for the legibility is 2.71, while the highest average grade has a sample reproduced with 16 layers of varnish, 4.67 for quality and 4.88 for legibility. Based on the given assessments, it can be concluded that the quality of reproduction and legibility of Braille dots obtained with 8 and 10 layers of varnish are not very satisfactory, and that the samples reproduced in this way do not meet the requirements. The sample obtained with 12 layers has a very high legibility grade (4.00), while the mutual evaluation of print production quality is quite solid (3.17), and it can be concluded that with 12 layers of varnish satisfactory prints are produced, in terms of reproduction quality and legibility. By further increasing number of the layers the average grade increases and, by looking at these values it can be concluded that the highest quality samples are produced with 16 layers of varnish. Here it is important to establish a compromise, and choose samples that have satisfactory grades for both criteria, and require less time and less material consumption. Hence, find the right ratio of quality and economy. According to the given grades, it can be seen that the threshold for good prints would be the application of 12 layers of varnish, and the prints reproduced that way would be considered appropriate, and compared to prints with 14 and 16 layers of varnish, which received higher grades for two given parameters, they require less production time as well as less varnish consumption.

Below is a statistical overview of the results of the mutual evaluation of the reproduction quality of prints (Figure 9), and the legibility of the formed Braille dots (Figure 10), based on blind people survey. Figures show minimum and maximum grades given to each individual sample, the average value, and the value of standard deviation.

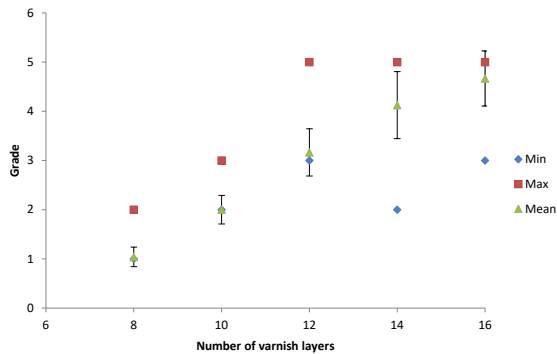
Also, there is a correlation graph (Figure 11) representing legibility and dot height reproduction quality, based on number of varnish layers, showing correlation between influencing factors. On the graph there are

Table 2

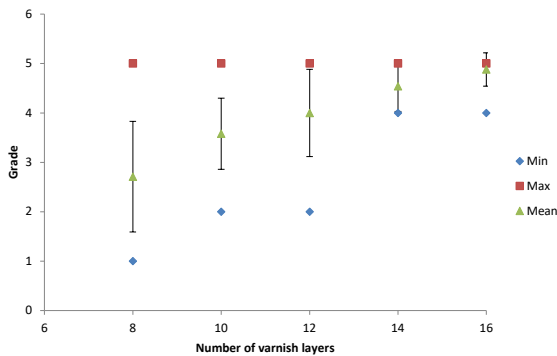
Average values of grades of legibility and quality of reproduced samples

Number of layers of varnish	8 layers	10 layers	12 layers	14 layers	16 layers
Average grade of Braille dot height reproduction quality	1.04	2.00	3.17	4.13	4.67
Average grade of Braille legibility	2.71	3.58	4.00	4.54	4.88

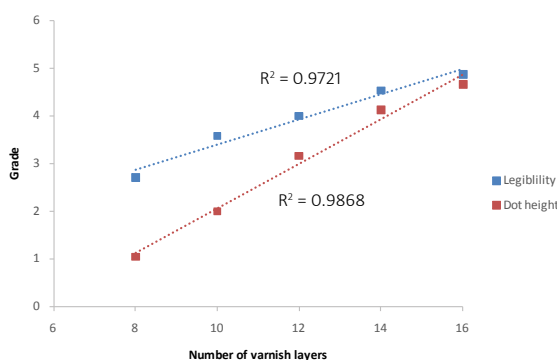
also R-squared values, which are for both variables near 1. Thus, it can be concluded that there is a high positive correlation between legibility and dot height reproduction quality and number of varnish layers.



» **Figure 9:** Evaluation of the reproduction quality of the Braille dots height with a different number of layers of varnish



» **Figure 10:** Evaluation of the legibility of Braille reproduced with a different number of layers of varnish



» **Figure 11:** Correlation graph representing legibility and dot height based on number of varnish layers

Conclusion

Labelling of products in Braille is currently mandatory for products of the pharmaceutical industry, but it can

be expected that in the near future it will be mandatory for products of other branches of industry, primarily food and chemical. Therefore, the possibility of reproducing Braille using UV varnish and UV ink-jet printing technique on self-adhesive label paper was investigated. The paper was previously printed using the flexo printing technique with Flint UV ink. An actual design was printed. The ink printing order was CMYK. Braille was then printed on the surface of the paper that was printed with 40% yellow. It was printed with 8, 10, 12, 14 and 16 layers, on a UV ink-jet machine Roland VersaUV LEC-300. Instrumental measurements of the height and the diameter of the dot, as key parameters, were performed. Also, a survey was conducted among blind and partially sighted people, in order to examine the legibility and quality of the production of printed samples, since the labelling in Braille is intended for this group of people.

In the case of a Braille reproduced with varnish, the height does not have to be a decisive factor in easier reading as in the case of a Braille made by embossing. Varnish hardness and accurate shape of the dot are also important. It has been determined by instrumental means that with the increase in the number of varnish layers, there is an increase in both the height and the diameter of the reproduced dot. First, there is a larger increase in diameter, and a smaller increase in the height of the dot. It can be assumed that it is caused by spreading of the varnish around the dot base. After that, with further application of varnish layers, there is a larger increase in the height of the dot, while the increase in diameter is insignificant. This can be explained by the fact that with 10 layers of UV varnish applied, spreading is reduced to minimum, since amount of varnish in one layer slightly flows over the edges of polymerized layers. The diameter of the reproduced dot for all samples is smaller than it is defined in Marburg Medium standard. But, with 10 layers of varnish (1.2271 mm) diameter slightly approaches the lower limit prescribed by this standard, i.e. the diameter prescribed by the ECMA Euro Braille standard (1.3 mm). With 16 layers of varnish this value is almost reached (1.2742 mm). The optimal dot height, which is defined by the ECMA Euro Braille (0.5 mm) and many other standards (British, American, German, Italian, Japanese, Swedish, etc.), was approximately obtained with 12 layers of varnish (0.47 mm). With a further increasing number of layers of varnish there is a significant increase in the height of the dot and it exceeds the standard value. For 14 layers of varnish it is 0.61 mm. Longer reading of the text in Braille, which has a higher dot, can lead to fatigue, as well as the possibility of damage to the fingertips.

Also, the analysis of the profile of Braille dots, obtained with a perthometer, founded that the created dot has a domed shape and that its peak is approximately in the centre of the dot. This is very important for detection of the dot and finger comfort.

Based on the conducted survey and the presented and analyzed results, it can be concluded that it is possible to reproduce tactile prints of appropriate quality and legibility using UV varnish and UV ink-jet printing on the presented self-adhesive label paper. Samples reproduced with 8 and 10 layers of varnish received bad grades for legibility, and especially for the quality of print reproduction, and were ranked as the worst reproduced. Samples in which the Braille dot was formed using 12 layers of varnish received very good grades for legibility and good grades for quality, and it can be concluded that they represent samples of appropriate quality and legibility. Samples reproduced with an even greater number of layers of varnish, 14 and 16, received even better grades in terms of legibility and quality of reproduction.

From all the above, it can be concluded that it is possible to reproduce quality Braille using UV ink-jet printing, and that for a quality reproduction a minimum of 12 layers of varnish is needed. Thinking about rationalizing costs and time, it is recommended to use 12 layers of varnish, because they represent the threshold for a quality Braille dot on the presented paper. Further increase of the varnish application leads to better reproduction and more readable print, according to the respondents, but there is also an increase in the consumption of the UV varnish, as well as the time required for the reproduction of samples. In addition, the height of the dot exceeds the height prescribed by the ECMA Euro Braille, as well as many others standards. This can be a problem with longer reading. It can be unusual for users accustomed to a lower Braille dot and, it can also reduce sensitivity in the fingertips.

Since the printing substrate itself directly affects the height of the applied varnish, future research should be focused on this. The quality of Braille dots and the legibility of Braille formed on different types of label papers, as well as some other types of substrates: plexiglass, glass, wood, etc., should be examined. Also, further research should be focused on examining the durability of the Braille dot formed by the technique of UV ink-jet printing on abrasion and tearing, the influence of light and temperature, etc.

References

- Ackland, P., Resnikoff, S. & Bourne, R. (2017) World blindness and visual impairment: despite many successes, the problem is growing. *Community eye health*. 30 (100), 71–73.
- American Foundation for the Blind (2019) *What Is Braille?*. Available from: <https://www.afb.org/blindness-and-low-vision/braille/what-braille> [Accessed: 13th December 2019].
- BOBST (2021) *ACCUBRAILLE - Braille embossing*. Available from: <https://www.bobst.com/ncen/products/folding-gluing/complementary-products/overview/machine/accubraille-gt/> [Accessed: 30th May 2021].
- Bourne, R.R.A., Flaxman, S.R., Braithwaite, T., Cicinelli, M.V., Das, A., Jonas, J.B., Keeffe, J., Kempen, J.H., Leasher, J., Limburg, H., Naidoo, K., Pesudovs, K., Resnikoff, S., Silvester, A., Stevens, G.A., Tahhan, N., Wong, T.Y., Taylor, H.R.; Vision Loss Expert Group (2017) Magnitude, temporal trends, and projections of the global prevalence of blindness and distance and near vision impairment: a systematic review and meta-analysis. *The Lancet Global Health*. 5 (9), e888–e897. Available from: doi: 10.1016/S2214-109X(17)30293-0.
- Burman, P. & Lofstedt, B. (2001) *Printer head for a Braille printer and a method of manufacturing the same*. United States Patent 6 241 405 B1 (Patent).
- Creagh, L.T. & McDonald, M. (2003) Design and performance of ink-jet printheads for non-graphics-arts applications. *MRS Bulletin*. 28 (11), 807–811. Available from: doi: 10.1557/mrs2003.229.
- Douglas, G., Weston, A. & Whittaker, J. (2008) *Braille dot height research: Investigation of Braille Dot Elevation on Pharmaceutical Products*. University of Birmingham. Final report 2008. Available from: <https://www.birmingham.ac.uk/Documents/college-social-sciences/education/victor/braille-dot-height.pdf> [Accessed: 28th June 2021].
- EBU (2019) *About blindness and partial sight – facts and figures*. Available from: <http://www.euroblind.org/about-blindness-and-partial-sight/facts-and-figures> [Accessed: 5th December 2019].
- Eccles, S. (2014) *How to print 3D with a UV digital inkjet*. Available from: <http://www.fespa.com/news/features/how-to-print-3d-with-a-uv-digital-inkjet.html> [Accessed: 13th February 2015].
- ECMA (2008) *Braille on Folding Cartons*. The Hague, ECMA.
- European Commission (2005) *Guidance concerning the Braille requirements for labelling and the package leaflet*. Brussels, European Commission. Available from: https://www.gmp-compliance.org/files/guidemgr/Braille_text20050411.pdf [Accessed: 28th June 2021].
- Format Media Ltd. (2010) *DX4 Printhead - 1000002201 - for Epson, Roland, Mimaki and Mutoh*. Available from: <https://www.largeformatreview.com/hardware/wide-format-print/dx4-print-head-1000002201-for-roland-mimaki-and-mutoh-1000002201> [Accessed: 23rd June 2021]
- Fricke, T., Tahhan, N., Resnikoff, S., Papas, E., Burnett, A., Ho, S., Naduvilath, T. & Naidoo, K. (2018) Global Prevalence of Presbyopia and Vision Impairment from Uncorrected Presbyopia. *Ophthalmology*. 125 (10), 1492 – 1499. Available from: doi: 10.1016/j.ophtha.2018.04.013.
- Golob, G., Gregor-Sveteč, D., Leskovšek, A., Turnšek, A., Majnarić, I., Dudok, T., Mayik, V. & Urbas, R. (2014) Braille text and raised images used in books for children who are blind or visually impaired.

- In: Urbas, R. (ed.) *Proceedings 7th International Symposium of Information and Graphic Arts Technology, 5–6 June 2014, Ljubljana, Slovenia*. Ljubljana, Faculty of Natural Sciences and Engineering, Department of Textiles, Chair of Information and Graphic Art Technology. pp. 109-111.
- Golob, G., Gregor Svetec, D., Urbas, R., Rotar, B., Jereb, N., Mayik, V. & Dudok, T. (2013) Dot shape and legibility analysis of multilayer UV ink-jet printed Braille text. In: *XIth Symposium on Graphic Arts, 17-18 June 2013, Pardubice, Czech Republic*. Pardubice, Department of Graphic Arts and Photophysics. pp. 61-65.
- Golob, G., Rotar, B. & Šulc, D. (2011) Braille dot height impact on the functionality and legibility of the pharmaceutical packaging. In: Enlund, N. and Lovreček, M. (eds.) *Advances in Printing and Media Technology, Proceedings of the 38th International Research Conference of iariqai, 11-14 September 2011, Budapest-Debrecen, Hungary*. Darmstadt, The International Association of Research Organizations for the Information, Media and Graphic Arts Industries. pp. 293-299.
- Hashemi, H., Yekta, A., Jafarzadehpur, E., Doostdar, A., Ostadimoghaddam, H., & Khabazkhoob, M. (2017) The prevalence of visual impairment and blindness in underserved rural areas: a crucial issue for future. *Eye (London, England)*. 31 (8), 1221–1228. Available from: doi: 10.1038/eye.2017.68.
- Havenko, S., Labetska, M., Stępień, K., Kibirkštis, E. & Venytė, I. (2013) Research of influencing factors on the change of geometric parameters of Braille elements on self-adhesive labels. *Mechanika*. 19 (6), 716-721. Available from: doi: 10.5755/j01.mech.19.6.6016.
- Jowat (2019) *Structural Braille Varnish*. Available from: https://www.jowat.com/fileadmin/dokumente/anwendungen/PDFs_AI_PV/AI_Braille_EN.pdf [Accessed: 5th December 2019].
- Kibirkštis, E., Venytė, I. & Lydekaitytė, J. (2012) Resistance to mechanical effect of Braille dot surface, formed on different materials. In: *VII International Scientific-Practical Conference Book quality, 6-8 June 2012, Lviv, Ukraine*. Lviv, Ukrainian Academy of Printing. pp. 144-150.
- Klisarić, V., Novaković, D. & Milić, N. (2013) Ispitivanje taktilnih otisaka sa brajevim pismom reprodukovanih UV ink-jet tehnologijom štampe. *Zbornik radova Fakulteta tehničkih nauka*. 28 (7), 1302-1305.
- Labetska, M.T. (2012) Analytical research of technological features of thermographic printing. *Book quality*. 1 (21), 123-128.
- Labetska, M.T. & Havenko, S.F. (2012) Research of performance indicators of Braille relief-dot elements on packaging. In: *I International Scientific-Practical Conference Packaging industry: modern tendencies of development and specialists training, 2012, Lviv, Ukraine*. Lviv, Ukrainian Academy of Printing. pp. 111-114.
- Majnarić, I., Bolanča Mirković, I. & Golubović, K. (2012) Influence of UV curing varnish coating on surface properties of paper. *Tehnički Vjesnik*. 19 (1), 51-56.
- McCallum, D. & Ungar, S. (2003) An introduction to the use of inkjet for tactile diagram production. *The British Journal of Visual Impairment*. 21 (2), 73-77. Available from: doi: 10.1177/026461960302100206
- McCallum, D., Ahmed, K., Jehoel, S., Dinar, S. & Sheldon, D. (2005) The design and manufacture of tactile maps using an inkjet process. *Journal of Engineering Design*. 16 (6), 525-544. Available from: doi: 10.1080/09544820500273946.
- Pascolini, D. & Mariotti, S.P. (2011) Global Estimates of Visual Impairment: 2010. *The British journal of ophthalmology*. 96 (5), 614-618. Available from: doi: 10.1136/bjophthalmol-2011-300539.
- PharmaBraille (2019a) *The Braille Alphabet*. Available from: <https://www.pharmabraille.com/pharmaceutical-braille/the-braille-alphabet/> [Accessed: 13th December 2019].
- PharmaBraille (2019b) *Marburg Medium Braille Font Standard*. Available from: <https://www.pharmabraille.com/pharmaceutical-braille/marburg-medium-font-standard/> [Accessed: 25th December 2019].
- Roland (2019) *ECO-UV, EUV-GL Ver. 2 - Safety Data Sheet*. Roland DG Corporation. Available from: https://www.rolanddg.kr/-/media/roland-apac/dgk/files/support/sds/euv2/euv2_gl_20190524.pdf?la=ko&hash=B32C66BE4710D421B5A77C-848C488A74CF22A566 [Accessed: 28th June 2021].
- Royal Blind (2019) *Braille Facts*. Available from: <https://www.royalblind.org/national-braille-week/about-braille/braille-facts> [Accessed: 13th December 2019].
- Schär, M., Krivec, T., Golob, G. & Selbmann, K.-H. (2015) Yellowing of thick-film coatings printed with UV-curable inkjet varnishes. *Advances in printing and media technology*. 42, 265-274.
- Tiresias (2008) *Braille Cell Dimensions*. Available from: <http://www.arch.mcgill.ca/prof/klopp/arch678/fall2008/3%20Student%20exchange/Team%20Surface/Connexion%20Surface%20Folder/MA%20files/Braille%20cell%20dimensions.pdf> [Accessed: 25th December 2019].
- Urbas, R., Rotar, B., Hajdú, P. & Elesini, U.S. (2016) Evaluation of the modified braille dots printed with the UV ink-jet technique. *Journal of Graphic Engineering and Design*. 7 (2), 15-24. Available from: doi: 10.24867/JGED-2016-2-015.
- VisionAware (2019) *All About Braille*. Available from: <https://www.visionaware.org/info/everyday-living/essential-skills/reading-writing-and-vision-loss/all-about-braille/1235> [Accessed: 7th December 2019].
- WHO (2019) *World report on vision*. World Health Organization. Available from: <https://www.who.int/publications/i/item/9789241516570> [Accessed: 28th June 2021].

Yim, J. M. (1996) *Touch-readable product and associated process*. World Intellectual Property Organization WO1996041320A1 (Patent).




© 2021 Authors. Published by the University of Novi Sad, Faculty of Technical Sciences, Department of Graphic Engineering and Design. This article is an open access article distributed under the terms and conditions of the Creative Commons Attribution license 3.0 Serbia (<http://creativecommons.org/licenses/by/3.0/rs/>).

Statistical evaluation of a Color Managed Digital Printing Workflow (CMDPW) consistency [4th C of CMW]

ABSTRACT

The purpose of this applied research was to determine the Color Managed Digital Printing Workflow (CMDPW) consistency (4th C of the color management) over a period of time [100 days, (N = 100)]. The quality of digital color printing is determined by these influential factors: screening method applied, type of printing process, calibration method, device profile, ink (dry-toner or liquid-toner), printer resolution and the substrate (paper). For this research, only the color printing attributes such as the overall average color deviation [ACD, $\Delta E_{(2000)}$] and the solid ink density (SID) were analyzed to examine the CMDPW process consistency in a day-to-day digital printing operation. These are the color attributes which are monitored and managed for quality accuracy during the printing. Printed colors of the random sample size (n = 80) were measured against the GRACoL2013 standards to derive the colorimetric/densitometric values. Reference colorimetric values used in the analysis were the threshold deviations (acceptable color deviations) as outlined in the ISO12647-7 standards (GRACoL2013). A control charts analysis was applied for further determining the process (CMDPW) SID and ACD variation. The data collected were run through multiple software applications (MS-Excel/SPSS/Minitab) to apply various statistical methods. Analyzed data from the experiment revealed that the printed colorimetric values were in match (aligned) with the GRACoL 2013 (reference/target). Since the SID values of CMYK colors were in control throughout the process, this enabled the CMDPW to produce consistent acceptable color deviation (Average Printed $\Delta E_{(2000)} = 2.978$; SD = 0.437; Acceptable Threshold color deviation is $\Delta E_{(2000)} \leq 3.00$).

Haji Naik Dharavath 

Central Connecticut State University, Department of Computer Electronics & Graphics Technology, New Britain, USA

Corresponding author:
Haji Naik Dharavath
e-mail: dharavathh@ccsu.edu

First received: 9.4.2021.

Revised: 7.8.2021.

Accepted: 22.9.2021.

KEY WORDS

calibration, color deviation, solid ink density, control chart, output profile, colorimetry, gamut, screening

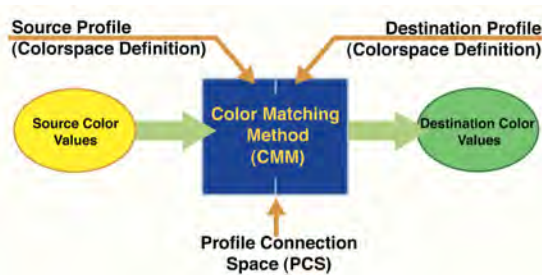
Introduction

Over the past three decades, the printing (graphic arts or graphic communications) industry has been revolutionized. Technology, workflow, management strategy, markets, and customer expectations have changed. Today, print is just one of many media channels which consumers can access. Advancements in science and engineering fields are enabling the printing and graphic professionals to apply scientific research methods across

prepress, print production (press area), and quality control areas for quality color reproduction. Applying these methods heightens the importance of proper print production workflow. The value and role of printing is changing, and the use of print is being merged across multiple communications channels: web, mobile, devices and social media. Recent developments in the computing, networking and digital printing technologies enable the digital print media to become a powerful multi-channel marketing and communications tool. Due to these

changes, there is an increased demand for an educated, skilled and technically competent workforce. These changes have resulted in both opportunities and challenges and have created a need for this workforce who understand the entire graphics and print media process and possess the skills necessary to manage print and non-print operations. In a quest to empower students to better understand the quality improvement techniques, this applied research examined the industry standard printing process and quality management practices similar to those a student would encounter upon entering into the industry. Hence, for a student to consistently deliver a quality print, managing and controlling color from the input device to a multicolor output device is a major concern for the graphics and imaging educator.

Modern printing has evolved from a craft-oriented field toward a color management science. This is demanding a greater color control among the display, input/color capturing, and output devices (printing and non-printing) and the substrates used in the printing and imaging industry. The quality of color image reproduction of any type of printing (digital or traditional) is largely influenced by the properties of substrate/paper (Wales, 2008). A modern and up-to-date commercial printing workflow requires a Color Management System (CMS) to produce a quality color printing. A CMS enables the color producer (printer operator or the designer) to deliver accurate output colors regardless of device color capacities with the use of proper color management techniques (see Figure 1). Analyzing the color image by examining its quantitative attributes eliminates the subjective judgment of color quality evaluation of printed colors or colors in nature.



» **Figure 1:** Schematic of PCS of CMS (Courtesy of Adobe Systems, Inc.)

Rationale for literature review

A continuous-tone color image is composed of a full spectrum of shades and color, from near white to dense black. In a traditional printing (offset, digital offset, gravure or flexography) workflow, the method by which continuous-tone photographic images are transformed to a printable image is called halftoning. In this method, varying percentages of the printed sheet are covered with halftone dots to represent the varying tones in the

image. The ink (paste or liquid ink or dry toner) printed by each dot, of course, has the same density. At normal viewing distance, the dots of a printed image create an optical illusion of a continuous tone image. In contrast, a simple digital image could be a binary picture, $[h(x, y)]$, with each point being either completely black or completely white (Pnueli & Bruckstein, 1996). A digital halftone is a pixel map, with bit depth, that gives the impression of an image containing a range of gray shades or continuous tones. An 8-bit grayscale image contains 256 different levels of gray from white to black.

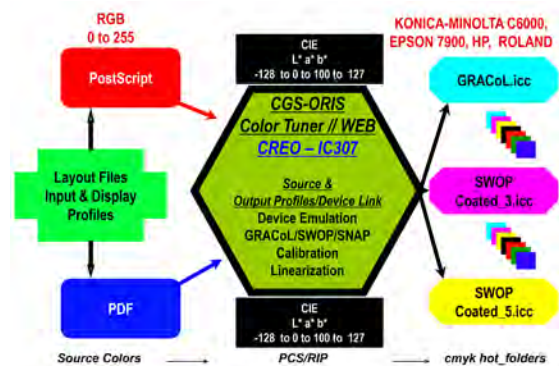
Digital printing methods differ in that they usually do not have a direct physical impact on the substrate. Inkjet printing utilizes different methods of transferring liquid ink droplets to a substrate to create an image. Another digital printing technology known as color-electrophotography, or laser printing, is commonly used and employs charged toner particles that transfer electrostatically to the substrate and create an image that is fused to the surface. Laser and ink-jet printing generate the majority of digitally printed materials in the industry. Digital printing technologies today have reached a level of quality that is comparable to traditional printing methods. In studies of print quality using process color ink systems, there are a number of variables, such as dot gain, that may cause tonal variations, and can have negative influences on the accuracy of color reproduction. Measuring and recording certain color print attributes may enable the technologist to make controlled adjustments and then check these variables to see if positive changes can be affected and maintained.

Overview of Color Management Digital Printing Workflow (CMDPW)

Color Managed Digital Printing Workflow (CMDPW) is represented through schematic illustrations of activities that reflect the systematic organization of analog and digital devices used during the print and image production process (see Figure 2). A print ready e-file (.PDF or .JPEG or .PSD or PostScript, etc.) is likely to be manipulated and later printed by an array of output digital devices [computer-to-plate (CTP), digital printers and printing presses].

Given each family of devices tends to create and produce color differently, the challenge is to manage color consistency across the entire workflow. Digital color print reproduction involves physical/mechanical interaction among the imaging cylinder, dry/liquid toner, and the substrate (Novaković & Avramović, 2012). The outcome of this interaction is the color print. Review of numerous reports revealed that the study of color is a science and the optical aspects of color only are quantitatively analyzable and measurable. The human eye, however, perceives color more subjectively, which poses a challenge at times for the printing and image reproduction industry.

Input (scanners or digital cameras) and output (monitors or printers) devices produce colors differently because they depend on their own color capabilities. The color management system simplifies and improves the reproduction of color images accurately from device to device.



» **Figure 2:** Schematic of CMW at Laboratory for this Research

The International Color Consortium (ICC) was formed in 1993 and it defines the standards for color device characterization (Adams & Weisberg, 2000). Today, ICC represents more than seventy industry and honorary members (International Color Consortium, 2009). This device characterization is presented in terms of specially formatted files, which have come to be called profiles. Unfortunately, the use of color management systems has not yet solved all the problems of color reproduction (Fleming & Sharma, 2002). However, it has made possible the quantification of problems. As always, in quality control, with quantification comes the ability to control and, with control, quality management becomes possible (Fleming & Sharma, 2002).

Color Management Workflow (CMW) or Color Management System (CMS) uses a set of hardware tools and software applications working together to create accurate color among various input (image capturing), display, and output devices (printing). A CMS consists of device profiles (characterization of devices), which control and document the working performance of the scanner, monitor, and the printer. A device color transformation engine (Color Management (matching) Module (method) or CMM) is one that interprets the color data among the scanner, display, and the printer. The gamut compensation mechanism of the CMS addresses differences among the color capabilities of input, display and output device. A device independent color space (Profile Connection Space or PCS) is a space through which all color transformation occurs from one device-dependent color space to another (see Figure 1). The PCS is based on the spaces (color models) derived from CIE color space (color model). This device color characterization file (profile) passes in and out of PCS to complete the color transformation (Fleming & Sharma, 2002). The

PCS of the CMS is the central hub of the CMS in which a particular color value is considered absolute and not subject to interpretation (Fleming & Sharma, 2002).

The 4 C's (Calibration, Characterization, Conversion, and Control) of CMS or CMW

To implement the CMS successfully, all the devices (monitor, scanner or digital camera, and printer or printing press) which are used for printing and imaging purposes must be calibrated, characterized (profiled) and their color capabilities (RGB and CMYK) converted into an independent color space (CIE $L^* a^* b^*$ space). A calibration process means standardizing the performance of the devices according to the device manufacturer specifications so that the results of the devices are repeatable. A profiling process (or characterization) refers to colorimetric assessment of the device color performance and creation of an ICC (International Color Consortium) profile specific to that device. The characterization process requires CMS hardware tools and software. Characterization of the devices is converted into an ICC profile file format. It communicates measured color output of devices in response to known output. Conversion refers to translating color image data from one device color space to another device space. It is also known as color transformation. Control or Consistency (the fourth C) means the user of a CMW must monitor and analyze the use of the CMW process through the use of statistical process control (SPC) tools in order to avail the benefits of the CMW.

Statistical Process Control (SPC) tools

Statistical process control, the creation of internal standards, and equipment performance tracking are becoming increasingly important in the color managed digital printing workflow (Kipman, 2001). In a given Color Managed Digital Printing Workflow (CMDPW) scenario where visual methods are currently being used to evaluate image quality in production printing, measurement methods can either replace or augment results adding objective judgement, traceability and validity. Therefore, this increased efficiency becomes an added benefit to the CMDPW. Quality improvement (QI) practices represent a leading approach to the essential, and often challenging, task of managing organizational change (Burnes, 2000). Statistical process control (SPC) is, in turn, a key approach to QI (Wheeler & Chambers, 1992). SPC was developed in the 1920s by the physicist Walter Shewhart to improve industrial manufacturing (Thor et al., 2007).

In a CMDPW, use of SPC is a scientific technique to control, manage, analyze and improve the performance of a process by eliminating special causes of variation in the digital printing process (Thor et al., 2007). It is a powerful collection of problem-solving tools useful in achieving process stability and improving capability through edu-

cation on variability (Abteu et al., 2018). There are seven original SPC tools: Flow-Charts, Check-Sheets, Histograms, Pareto Diagrams, Cause-and-Effect Diagrams, Scatter Diagrams and Control Charts (Mears, 1995). SPC enables us to control quality characteristics of the methods, machines, workforce, and products. There are two kinds of variations that can occur in all manufacturing processes, including the digital printing, which causes subsequent variations in the final product (Abteu et al., 2018). The first is known as the common cause of variation and consists of the variation inherent in the process as it is designed (Abteu et al., 2018). It may include variations in temperature, properties of raw materials, ink/toner, etc. The second kind of variation is known as a special cause of variation and happens less frequently than the first (Abteu et al., 2018). For an example, failed calibration and characterization methods could be carried into the production processes.

A control chart is the best tool for determining whether a process (CMDPW) is in-control or not in-control. An in-control process is one that lacks “assignable causes” or “special causes” of variation. This means that the processes output will be consistent over time. This is not to say that the process will be capable of meeting your needs or your customer’s expectations, just that the results will be relatively consistent (Blevins, 2001). Good color reproduction requires consistency in the CMW. Accurate color reproduction is dependent upon several factors. One of the factors is the cyan, magenta, yellow, and black (CMYK) ink densities and quality of device profiles. To achieve acceptable printing results, it is important to establish aim points (target values or control limits of the process) and monitor the aim points consistency during the production process. With the use of specific process control techniques (SPC tool), one can determine if the consistency is in-control or not in-control. If the average density or color deviation values (Delta E) and range of the process fall between the established aim points the process is said to be within the specific process control. Contrarywise, if the color deviation and density values are not within the aim points, they would be not in-control (out of control).

Purpose of the research

The experiment was conducted in a color managed digital printing workflow (CMDPW). The purpose of this applied study is to determine the consistency (4th C of CMW) of colorimetric variation among the printed colors overall average color (CMYK-RGB) deviation (ΔE) and CMYK solid ink density (SID) variation in the electro-photographic color printing process over a period of time (100 days). To determine the statistically significant process variation among these color deviations over a period of time (OAPOT), a control chart analysis technique was employed. Reference colorimetric values are the threshold deviations (acceptable color deviations) as

outlined in the ISO12647-7 standards. To accomplish this, the following guiding objectives have been established:

1. Determine the deviation in color printing average/overall (CMYK+RGB) ΔE over a period of time (100 days) by comparing the printed colorimetry against the reference colorimetry.
2. Determine the deviation in the Solid Ink Density (SID) of CMYK colors over a period of time (100 days) by comparing the printed colorimetry against the reference colorimetry.

Limitations of the research

No engineering or mathematics or physics or statistical equations or computational methods were manually developed/used/applied during the experiment or data analysis stage. Industry standard software applications were used. For this research, limitations in the technology of the graphics laboratory were acknowledged. Prior to printing and measuring the samples, the digital color output printing device and color measuring instruments (spectrophotometer and densitometer) were calibrated against the recommended reference. The print condition associated with this experiment was characterized by, but not restricted to, the inherent limitations: colored images (TC1617x, ISO300, and ISO12647-7) chosen for printing. Additionally, the desired rendering intent applied, type of digital printer, type of paper, type of toner, resolution, screening technique, color output profiles, and calibration data applied are acknowledged. Several variables affected the facsimile reproduction of color images in the CMDPW, and most were mutually dependent. The scope of the research was limited to the color laser (electrophotographic) digital printing system (printing proof/printing), substrates, types of color measuring devices, color management and control applications (data collection, data analysis, profile creation, and profile inspection) used within the university graphics laboratory. Findings were not expected to be generalizable to other CMDPW environments. It is quite likely, however, that others will find the method used and data collected both useful and meaningful. The research methodology, experimental design, and statistical analysis were selected to align with the purpose of the research, taking into account the aforementioned limitations.

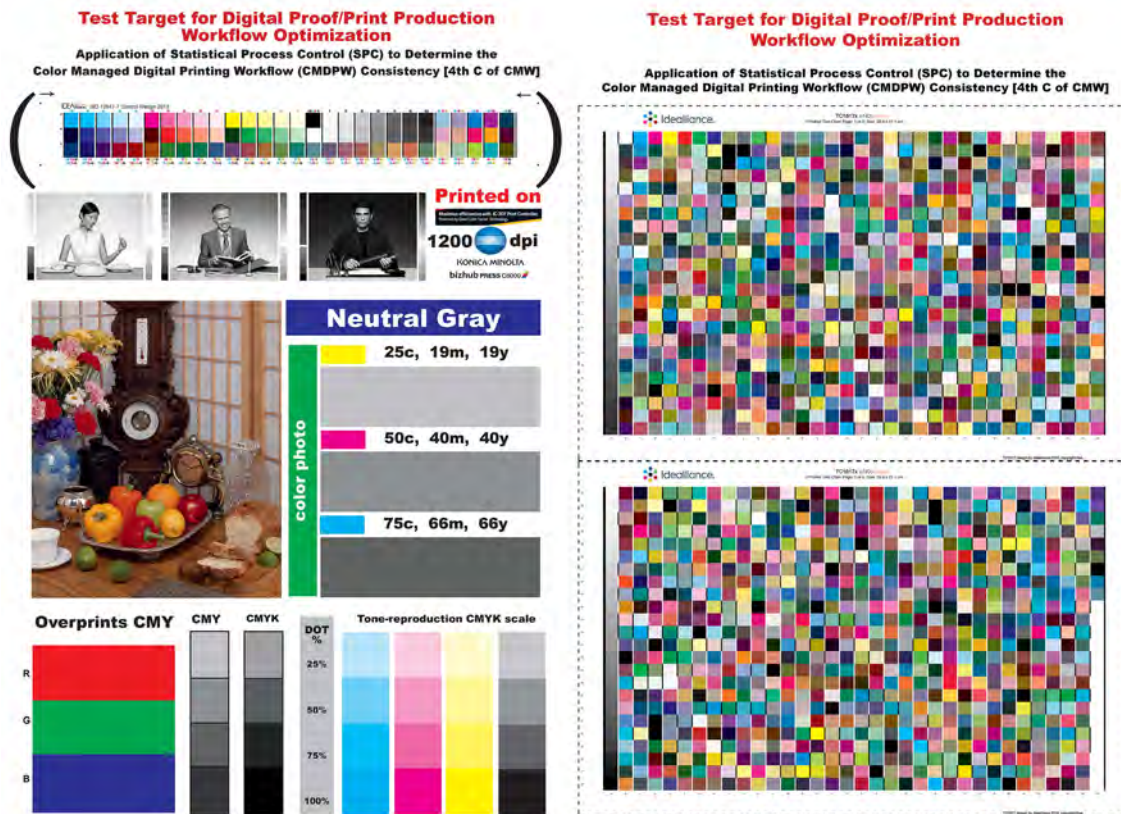
Research methodology

The digital color printing device used in this experiment is a Konica-Minolta bizHub C6000 Digital Color Press. It uses a Creo IC-307 raster image process (RIP) application (front-end system). A two-page custom test image (12”x18” size) was created for proofing and printing use for the experiment (See Figure 3). Table 1 presents the variables, materials, conditions, and equipment associated with this experiment.

Table 1

Experimental and Controlled Variables

Variable	Material/Condition/Equipment
Test image	Custom Test Target (See Figure 3)
Control strips/targets	ISO 12647-7 (2013), TC1617x
Other Images	B/W and Color for Subjective Evaluation
Profiling Software	X-Rite i1PROFILER 1.8
Profile Inspection Software	Chromix ColorThink-Pro 3.0
Image Editing Software	Adobe PhotoShop-CC
Page Layout Software	Adobe InDesign-CC
Source Profile (CMYK)	GRACoL2013.icc
Destination Profile (CMYK)	Custom, Konica-Minolta.icc
Reference/Source Profile (CMYK)	GRACoL2013.icc
Color Management Module (CMM)	Adobe (ACE) CMM
Rendering Intents	Absolute
Computer & Monitor	Dell OPTIPLEX/LCD
Raster Image Processor (RIP)	Creo IC-307 Print Controller with Profiling Tools
Digital Press/Printer	Konica-Minolta bizHub C6000 Color Laser
Calibrated CMYK Solid Ink Density	C = 1.75; M = 1.60; Y = 1.00; and K = 2.04
Type of Screen and Screen Ruling	Amplitude Modulated (AM), 190 LPI
Print Resolution	1200 x 1200 DPI
Toner	Konica-Minolta Color Laser
Type of Paper Weight/thickness	Mohawk 100LB Gloss Coated, Sheetfed
Type of Illumination/Viewing Condition	D50
Color Measurement Device(s)	X-Rite Eye-One PRO Spectrophotometer with Status T, 2° angle, and i1iO Scanning Spectrophotometer
Data Collection/Analysis Software	Minitab, MS-Excel, SPSS, and CGS-ORIS Certified Web



» **Figure 3:** Test Target Image

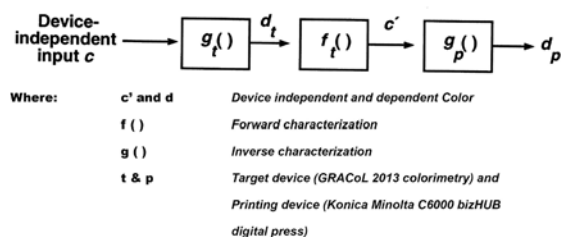
The test target contained the following elements: generic images for subjective evaluation of color, an ISO 12647-7 Control Strips (2013, three-tier), and a TC1617x target for gamut/profile creation. Colorimetric, Densitometric, and Spectrophotometric data were extracted by using an X-Rite Eye-One Spectrophotometer and an X-Rite i1iO Scanning Spectrophotometer from the color printed samples for the analysis. The process (CMDPW) was monitored for a total of 100 days. A total of 100 samples of target color images were printed/collected for daily measurement/analysis purpose. 100 prints were noted by letter "N" (N = 100). Of 100 samples, 80 samples (n = 80) were randomly selected and measured, noted by the letter "n" (n = 80). This sample size was selected in order of the specific confidence interval ($\alpha = 0.05$). Glass & Hopkins (1996) provides an objective method to determine the sample size when the size of the total population is known. This sample size is needed to make sure the reliability of data is accurate. It is well documented that a large sample size is more representative of the sampling (subjects) population (Glass & Hopkins, 1996). The following formula was used to determine the required sample size, which was 80 (n) printed sheets for this study (Glass & Hopkins, 1996):

$$n = \left[\frac{\chi^2 NP (1-P)}{d^2 (N-1) + \chi^2 P (1-P)} \right] \quad (1)$$

n = the required sample size
 χ^2 = the table value of chi-square for 1 degree of freedom at the desired confidence level (3.84)
 N = the total population size
 P = the population proportion that it is desired to estimate (.50)
 d = the degree of accuracy expresses as a proportion (.05)

CMW setup for the digital press

The digital output device used in this experiment is a Konica-Minolta (KM) C6000bizHub color printer (or digital press). KM C6000 uses a Creo IC-307 raster image process (RIP) server (front-end system) based workflow application. This workflow application (the RIP) enables the printer (or designer or operator) to emulate/simulate (See Figure 4) the color device to print as per the ISO 12647 series digital color printing production standards.



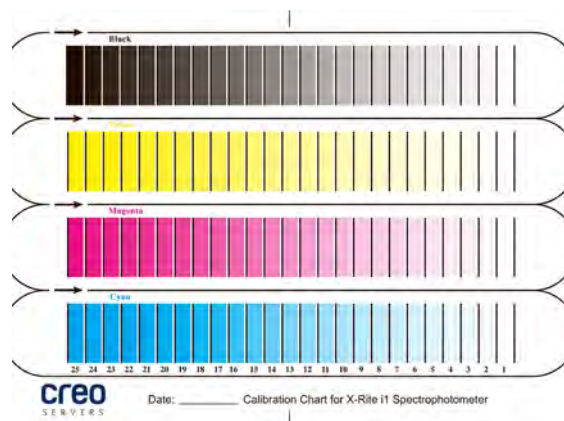
» **Figure 4:** Color Transformation of Device Emulation/ Simulation (Proof/Printing)

The RIP provides software tools for calibrating the printer and creating an ICC device profile. This simulation process requires the characterization data (an ICC profile) from the printing device (destination printer) as well as the data from the target device (an ISO 12647-7 reference colorimetry or other target device profile). Figure 4 illustrates how a device emulation is accomplished from characterizations of the proofing and target (printing) devices (Raja, 2002). Emulation/simulation is not possible without two profiles.

In this scenario, target colors are the source colors outlined in the General Requirement for the Applications in the Commercial Offset Lithography (GRACoL2013) standards and the printed colors are the destination colors of a device (Konica Minolta bizHUB C6000 digital press). Many up-to-date CMYK workflows emulate the printed colors to GRACoL standards by default, because the GRACoL reference colorimetry provides an optimal color balance based on the traditional CMYK (offset printing) workflows (Xerox, 2009).

Digital press calibration

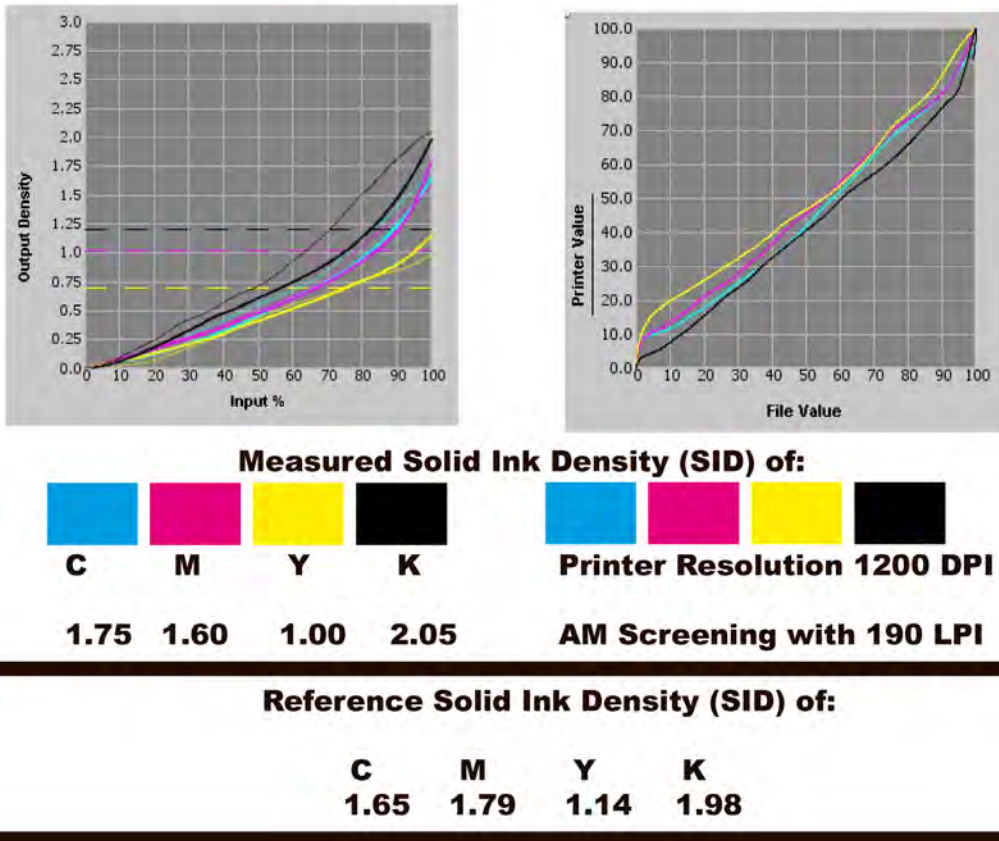
A calibration process means standardizing the performance of the devices according to the device manufacturer specifications so that the results of the devices are repeatable. Prior to printing the patches/target image, the printer was calibrated for amplitude modulated (AM) screening technique with 1200 x 1200 dots per inch (DPI) resolution as per the manufacturer's specifications for a 100 lb gloss coated paper. The calibration chart (See Figure 5) was printed and measured by using an X-Rite Eye-One Spectrophotometer.



» **Figure 5:** Calibration CMYK Chart

A calibration step in a CMDPW is designed to assure repeatable results by standardizing the performance of the devices according to the device manufacturer specifications. The calibration curve consists of the maximum and minimum printable (or acceptable) solid ink densities (SID) of each color (CMYK) used for the printing (See Figure 5A). The calibration data (range of

PRINTER CALIBRATION FOR 100 LB GLOSS COATED PAPER



» **Figure 5A:** Calibration of a Digital Printing Press

CMYK densities) were saved in the calibration lookup tables (LUT) of the RIP and a calibration curve was created. Printed Test target TC1617x (Page 02 of the target image) was used for the output device profile creation process. Measured and Reference (or target) SID values are extracted from the digital press LUT of the RIP.

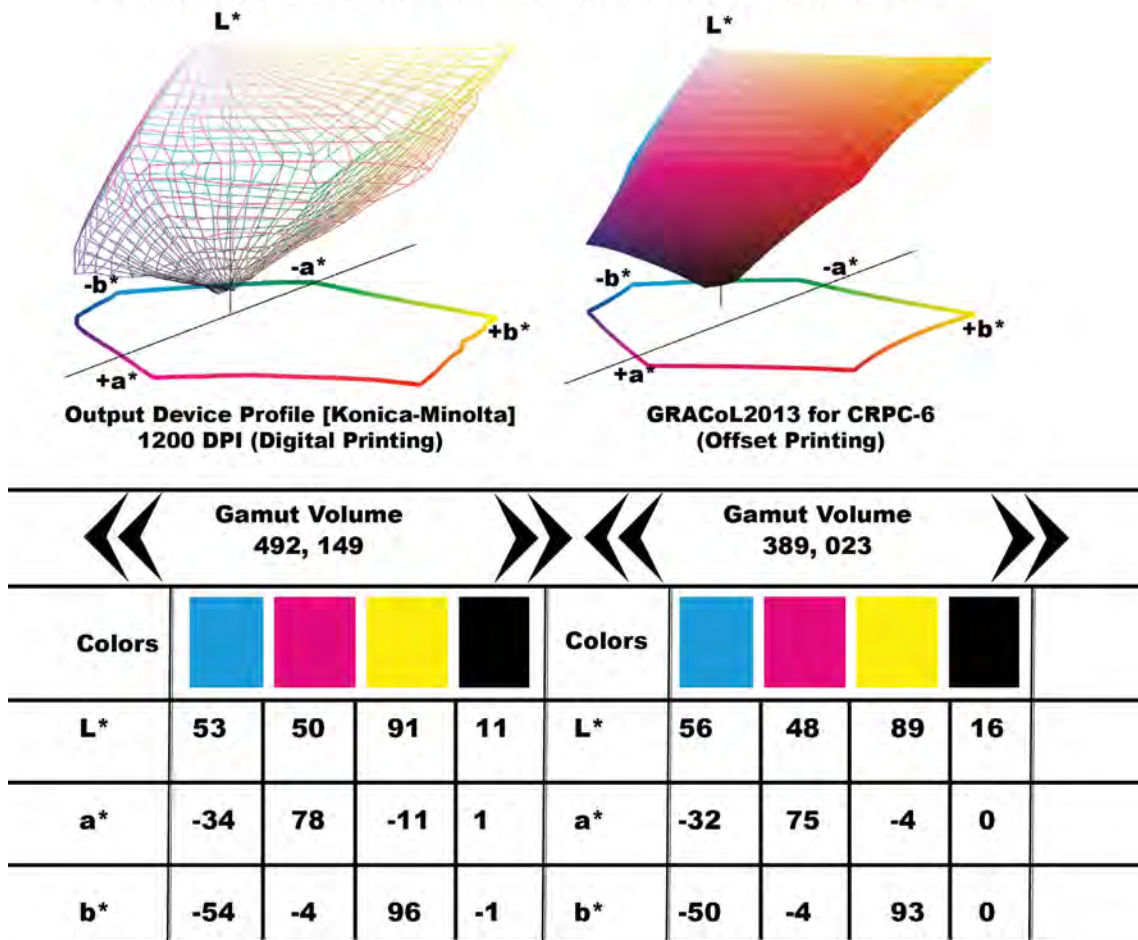
Digital printing press/Printer profile

The test target image (TC1617x) was placed into an Adobe InDesign-CC layout of 12" W x 18" H size and a PDF file was created devoid of any image/color compression (see Figure 3). Mohawk 100 LB gloss coated digital color printing paper 12" x 18" was used for printing the target image. A total of 100 sheets/copies of TC1617x were printed with the calibration curve attached. Also, an amplitude modulated (AM) halftone screening technique with 190 lines per inch (LPI) and 1200 DPI as the printer resolution was applied during the printing. No color management or color correction techniques were applied during the printing. Printed patches of TC1617x were measured in CIE L* a* b* space using the i1PROFILER application with an X-Rite i1iO spectrophotometer. The printer profile was then created and stored. The profile format version is 4.00 and it is considered as the Output Device (printing device) Profile (ODP). This profile was used as a destination profile (DP) in the workflow. The source profile

(SP) used in the experiment is a GRACoL2013 for characterized reference printing conditions-6 (CRPC-6). See Figure 6 for an output device profile comparison of GRACoL 2013 profile vs. ODP, gamut volume of the profiles, and L* a* b* values of each profile used.

Visual examinations of both the profiles indicate that the ODP (printer profile/digital press) color gamut volume (CGV) is higher than the target device profile/GRACoL2013 (see Figure 6). The CGV, a volume in CIE L* a* b* space can be interpreted as the number of colors which are discernable within a tolerance of $\Delta E = \sqrt{3}$ (Chovancova-Lowell & Fleming, 2009). Each profile is an indication that it has different color capabilities because it represents different imaging devices. Color gamut mapping can be completed by one of the four ICC recognized colorimetric rendering intents: perceptual, absolute, relative, and saturation. The rendering intent determines how the colors are processed that are present in the source gamut but out of gamut in the destination (output). For this experiment, absolute colorimetric intent was chosen. It intends to produce in-gamut color exactly and clips out-of-gamut colors to the nearest reproducible hue by scarifying saturation (chroma or vividness) and lightness (Fraser, 2001). The experiment had successfully calibrated the press and created the ODP for use in the remainder of the experiment.

Profile Comparison: ODP vs. GRACoL2013 CRPC-6 Ref.



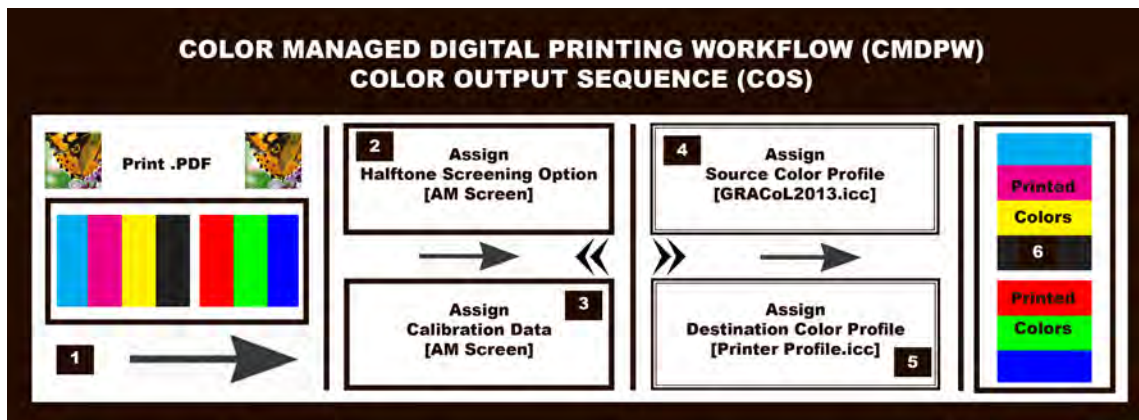
» Figure 6: Comparison of ODP vs. GRACoL2013 CRPC-6 Ref.

Printing with target (source) and destination profiles

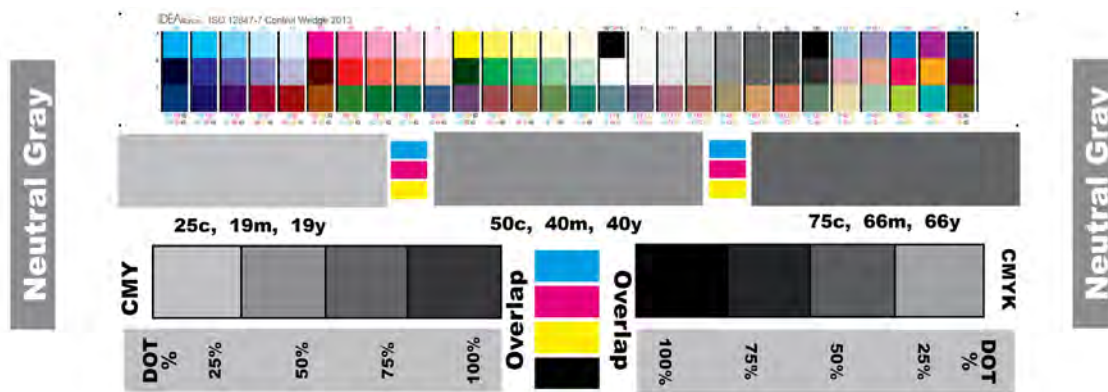
As stated earlier, AM screening technique was applied during the calibration and profile creation process in the experiment. The CMDPW was considered a group (process) within the experiment. A group involves a set of print parameters, such as a digital halftone screening technique [amplitude modulate (AM)], a calibration curve (of AM screened), a color source profile [General Requirements for Applications in Commercial offset Lithography for characterized reference printing conditions-6 (GRACoL2013 for CRPC-6)], and a color destination profile of a digital press (AM screened). As parameters illustrate in Figure 7 (Schematic Illustration of Sequence of Print Parameters for CMDPW), the test target of 12" x 18" (two pages) was printed for use in the experiment. The test target contained the following elements: TC1617x target, ISO 12647-7 (2013) control strip, an ISO 300 and custom images of color and b/w for subjective evaluation of color. A total of 100 sheets/samples were printed for the screening technique used by enabling the color management technique at the RIP. The digital press calibration

curve, destination profile, and the source profiles all were applied during the printing (see Figure 7).

The group printing performances were monitored for a period of 100 days to determine the fluctuations in the color consistency (4th C of CMW) by printing multiple printing jobs on the same type of paper with the same print sequences. Prior to start of the printing for the day, the test target (Figure 3) was printed, measured for the colorimetric and densitometric data and the sample was kept aside for a later stage analysis. A total of 100 target images were printed/collected for the analysis. Of the 100 printed samples (from 100 days, N = 100), data were generated from the randomly pulled 80 printed samples (80 days samples, n = 80). The test image consists of a printed ISO 12647-7 (2013) control strip (see Figure 8). By using Eye-One-Pro spectrophotometer with interface application, such as the CGS-ORIS Certified WEB, the printed image was measured against the GRACoL2013_CRPC6 reference data. Measured colorimetric data (CIE L* a* b*) from ISO 12647-7 (2013) control strip were used to determine the color deviations. Data derived from ISO 12647-7 (2013) control strip (sample) is the difference between the characterization data set (full



» Figure 7: Schematic Illustration of Sequence of Print Parameters for CMDPW



» Figure 8: ISO 12647-7 (2013) control strip with additional Color Patches

IT8.7/4 target) and the sample. The control strip (wedge) image is intended primarily as a control device for pre-press proofs but may also be used to control production printers or presses. The wedge has 3 rows and 84 patches, and it contains only a small sub-sample of the total printable color gamut. The wedge contains too few patches to prove an accurate match to a specification like GRACoL or SWOP (Specifications for Web Offset Publications). It does contain enough patches to monitor the stability of a system that has previously been tested with a target such as the IT8.7/4 (CMYK target image). The reference file content for this image (IT8.7/4) are the CMYK dot percentage values and the nominal CIE L* a* b* characterization data values for the GRACoL2013-CRPC6 reference. Colorimetric, densitometric, and spectrophotometric computations were used to determine the color deviations and CMYK solid ink densities. Colorimetric and densitometric formulae and formats were presented in the following section (DATA ANALYSIS) for each of the color deviations/attributes investigated.

Data analysis & research findings

Colorimetric computations and statistical process control methods were used for the color deviations and process variations. Analyzed collected data were presented in

the following pages/tables. Subjective judgment on color difference or any deviations was not used in this particular study because the subjective judgment of color difference could differ from person to person. For example, people see colors in an image not by isolating one or two colors at a time (Goodhard & Wilhelm, 2003), but by mentally processing contextual relationships between colors where the changes in lightness (value), hue, and chroma (saturation) contribute independently to the visual detection of spatial patterns in the image (Goodhard & Wilhelm, 2003). Instruments, such as colorimeters and spectrophotometers-, eliminate subjective errors of color evaluation perceived by human beings.

Solid Ink Densities (SID) of CMYK average variation

Solid Ink Density (SID) is defined as the ability of a material (ink/substrate/surface area) to absorb light, and it is a function of the percentage of light reflected from that material (Committee for Graphic Arts Technologies Standards, 1993). The reproduction of printed images during the press run (digital or analog processes) is susceptible to tonal and color variations mainly because of the dot size and SID. Reports reveal that it is important for the CMYK ink densities to be kept in balance during the printing. If ink densities are not in balance, color (hue)

will shift. Therefore, monitoring solid ink density during a press run is essential when comparing any printed material in terms of quality. Digital printing device RIP keeps (holds/stores) acceptable SID values in the calibration/linearization look-up-tables (LUT's) and enables an operator to apply the curve during the printing.

In the CMDPW (process or the group) of this experiment, the printed SID values of CMYK toners/inks were monitored for over a period of 100 (population size, N = 100) days by printing and measuring the SID values from the randomly selected samples [sample size, N = 100, n = 80, n₁ = 4 (CMYK)]. Data (SID) collected were compiled in MS-Excel/SPSS/Minitab and analyzed to derive the \bar{X} (average), SD (standard deviation) and \bar{R} (range average) and used for further analysis. Also, a normality test was performed by using the compiled SID data (see Table 2, Figure 9). A normality test is used to determine whether sample data (SID values) has been drawn from a normally distributed population (within some tolerance). Any research involving use of statistical tests requires data from a normally distributed sample. The normal distribution (ND) is the most important probability distribution in statistics because it fits many natural phenomena. It is practically feasible to measure the distances under the normal curve in terms of z-scores (fractions or multiples of +/- of 3 standard deviations from the mean).

Table 2

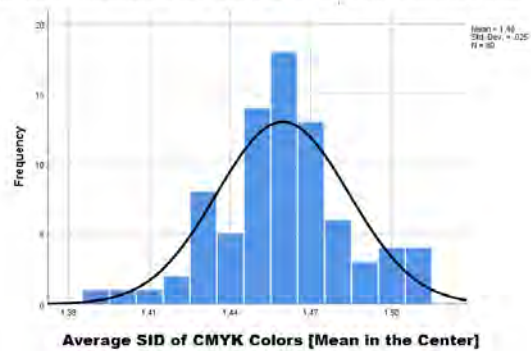
Descriptives of Normality Test for Average SID of CMYK in a CMDPW

Attributes/Variables	Statistics	Standard Error
Average (Mean) SID of CMYK [C = 1.420; M = 1.710; Y = 1.030; K = 1.670]	1.459	0.003
Median (Med)	1.460	
Standard Deviation (SD)	0.0245	
Skewness	-0.099	0.269
Kurtosis	0.430	0.532

The ND curve is symmetrical around the mean, showing that data of SID values near the average (\bar{X} = 1.46, SD = 0.025) are more frequent in occurrence than the SID values far from the \bar{X} . The Standard Error (Std Error or SE) is 0.003 of SID. It is an indication of the reliability/accuracy of the average SID of the CMYK in the process. A small SE is an indication that the produced average is a more accurate reflection of the actual population mean. A larger sample size will normally result in a smaller SE (while SD is not directly affected by sample size). Further normality validation was performed by visually evaluating the SID of CMYK values by plotting in the Quantile-Quantile (Q-Q) chart (see Figure 10). It plots the quantiles of SID values (values that split a dataset into equal portions) of the dataset instead of every individual data point of the collected

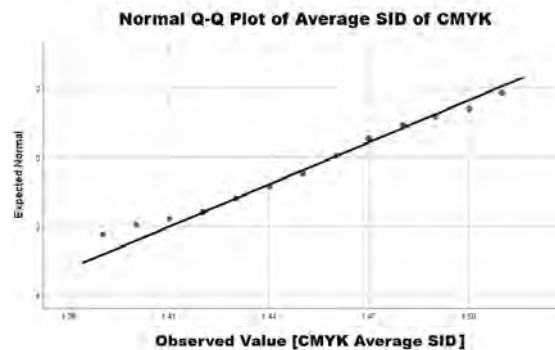
data. Also, Q-Q plot is easier to interpret when there is a large sample size (in this case, N = 100, n = 80).

Normal Distribution Curve of Average SID of CMYK Printing in a CMDPW



» **Figure 9:** Normal Distribution Curve of Average SID of CMYK in a CMDPW

The Skewness of the ND is -0.099 (with SE 0.269) and it is interpreted as the data is symmetrical (-0.5 and 0.5). The Kurtosis of the ND of the SID of CMYK colors of the process is 0.430 (with SE 0.532). If the Kurtosis is +1.00 of the ND of the SID of CMYK, then the distribution would be too peaked; if there is an indication of -1.00 of the ND of the SID of CMYK, the distribution is too flat. Distributions exhibiting skewness and/or kurtosis that exceed these guidelines are considered non-normal (Hair, Hult, Ringle, and Sarstedt, 2017). In graphs (see Figures 9 & 10), normal distribution appears as a bell shape curve and Q-Q plot represents a straight line. Therefore, the data collected (SID values of CMYK) were valid and will be used for further statistical analysis to determine the SID consistency of the CMDPW process.



» **Figure 10:** Q-Q Plot of Average SID of CMYK Colors in a CMDPW

The average and range control charts analysis was applied for further determining the process (CMDPW) SID consistency. The SPSS application was used to calculate/construct the graphs of the control limits of average (X-Bar) and range variation. The control limit (CL x-double bar), upper control limit (UCL x-bar) and lower control limit (LCL x-bar) values associated with the SID (CMYK) average variations of the CMDPW are compiled in Table 3. Differences were found in the SID values of printed colors when comparing with

the GRACoL standards. However, overall the process was consistent from day to day over a period of 100 days (see Figure 11) and concluded to be in-control.

Table 3

Solid Ink Density Average Variation of Printed Samples in a CMDPW

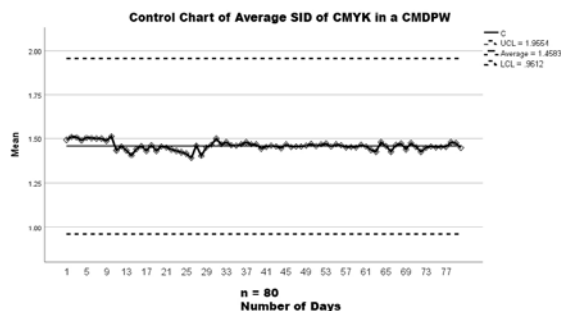
Color	GRACoL SID Standards	Printed Sample n = 80 Mean (average) $n_i = 4$	Printed Samples n = 80 Std. Deviation $n_i = 4$
Black	1.75	1.67	0.03
Cyan	1.40	1.42	0.07
Magenta	1.50	1.70	0.05
Yellow	1.00	1.03	0.02

Printed Samples Average Control Limits

UCL \bar{X}	1.95	
CL (X-Double Bar)	1.46	
LCL \bar{X}	0.96	

Source for GRACoL SID Standards: Guidelines & Specifications (International Digital Enterprise Alliance, 2007)

The Solid Ink Density (SID) X-Bar (average) and R (range) variation were monitored by comparing them to calculated tolerances (control limits of the process). If the variations are within the tolerances, then the SID of CMYK colors are accepted. If the variations are not within the established tolerances, then they are not accepted. The X-Bar chart illustrates how the SID average varied over a period of time (100 days), while the R-Chart illustrated the dispersion (variation) within the samples studied (monitored). These charts have three lines parallel to the x axis, while the average values are parallel to the y axis. The average and range of SID values (see Figures 11 and 12) fall closely along the control limit line (within the control limits), indicating the SID of the process was very consistent.



» **Figure 11:** Control Chart of Average SID of CMYK

SID Range Variation

The control limit (CL r-bar), upper control limit (UCL r) and lower control limit (LCL r) values associated with the SID (CMYK) range variation of the CMDPW are compiled

in Table 4. The SID range variations of CMYK printed colors over a period of time are in control. (see Figure 12).

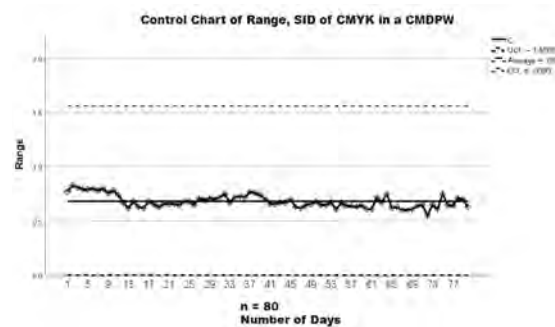
Table 4

Solid Ink Density Range Variation of Printed Samples in a CMDPW

Color	Average Maximum SID	Average Minimum SID	Printed Sample n = 80 Range Mean (average)
CMYK	1.71	1.03	0.68

Printed Samples Range Control Limits

UCL (Range)	1.55	
CL (R Bar)	0.68	
LCL (Range)	0.00	

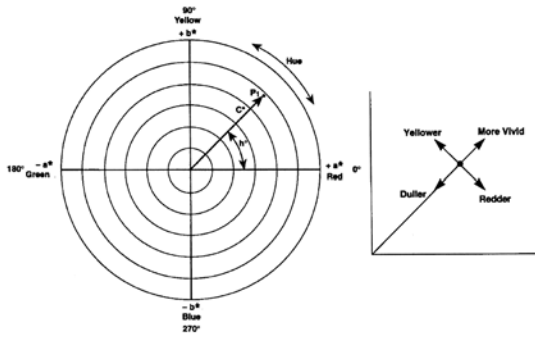


» **Figure 12:** SID Range Variation of CMDPW

Colorimetric variation [CIE L* a* b* and Delta E (ΔE_{2000})] in a CMDPW

Colorimetric values of printed colors against original colors and the deviations (Delta E) can be used to determine the visual variation in overall colors, hue, chroma, and lightness. The a*, b* coordinates correspond approximately to the dimensions of redness – greenness and yellowness – blueness respectively in the CIE L* a* b* color space and are orthogonal to the L* dimension. Hence, a color value whose coordinates a* = b* = 0 is considered achromatic regardless of its L* value. Assessment of color is more than a numeric expression. It is an assessment of the difference in the color sensation (delta) from a known standard. In the CIELAB color model, two colors can be compared and differentiated.

The expression for these color differences is expressed as ΔE [Delta E or Difference in Color Sensation]. In comparing the color differences between two colors, a higher deviation (ΔE) is an indication that there is more color difference and a lesser deviation (ΔE) is an indication of less color difference. In this scenario of the color measuring/evaluation stage, a consistent and standardized light source (D50 or D65) and angle of viewing (2° or 10°) are important (Committee for Graphic Arts Technologies Standards, 2003).



» **Figure 13:** Schematic of L^* a^* b^* & c^* , h^* Coordinates

Overall color variation (ΔE) of printed jobs vs. GRACoL 2013 Ref. in a CMDPW

The CIE L^* a^* b^* values associated with the CMYK+RGB colors of printed jobs vs. G7 GRACoL 2013 [CGATS21-2-CRPC6 (reference)] are compiled in Table 5 (International Digital Enterprise Alliance, 2014). Numerical color differences (ΔE) were found when comparing the average printed colors vs. GRACoL within all seven colors (CMYK+RGB). Also, noticeable visual color differences were found in the solid color area. Overall, both groups of images are similar in colors (See Figures 14), with the exception of the printed image consisting of lower L^* a^* b^* values. This results in producing the slightly higher ΔE for these colors.

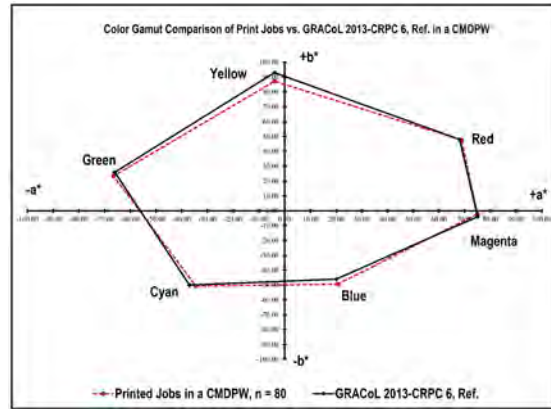
This higher color deviation (yellow, black, red, and green) might be the result of the substrate (paper) or toners used (age, condition, quality, etc.) or measurement error. These are the darker colors which produced lower L^* value and in turn affected the slightly higher color deviation. The 2D color gamut comparison (see Figure 14) reveals that the colors of the printed image closely match the reference colors.

Table 5

Overall Color Variation of CMYK+RGB: Printed Jobs vs. GRACoL 2013, CRPC-6 Ref.

CIE Color(s)	Printed Jobs Average			GRACoL 2013			Color Difference $\Delta E_{(2000)}$
	L^*	a^*	b^*	L^*	a^*	b^*	
	Color 1 N = 80*			Color 2 N = N/A			
White (W)	95.99	1.22	-6.22	95.02	0.98	-4.02	1.890
Cyan	56.21	-34.54	-50.65	56	-37	-50	1.691
Magenta	47.15	74.92	-2.15	48	75	-4	2.307
Yellow	88.06	-3.94	87.23	89	-4	93	2.749
Black (K)	9.87	-0.18	0.08	16	0	0	3.272
Red	48.75	68.74	47.61	47	68	48	4.657
Green	52.43	-66.48	23.39	50	-66	26	4.038
Blue	24.55	20.66	-49.38	25	20	-46	2.125

Average Printed $\Delta E_{(2000)} = 2.978$; SD = 0.437; Acceptable Threshold $\Delta E_{(2000)} \leq 3.00$



» **Figure 14:** Printed Images vs. GRACoL 2013-CRPC-6 Ref.

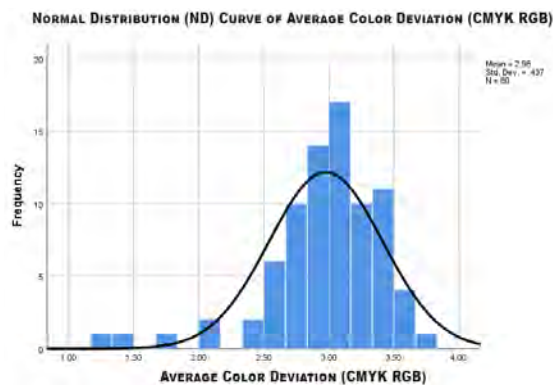
The goal was to determine the consistency /deviations among various attributes of colors over a period of 100 days in a CMDPW. The comparison is an indication that, in a color managed workflow (CMW), color matching of a target image can be achieved from device to device regardless of device color characterization and original colors. Subjective judgment was not used for the color comparison.

Table 6

Descriptives of Normality Test for Average Color Deviation [$\Delta E_{(2000)}$] in a CMDPW

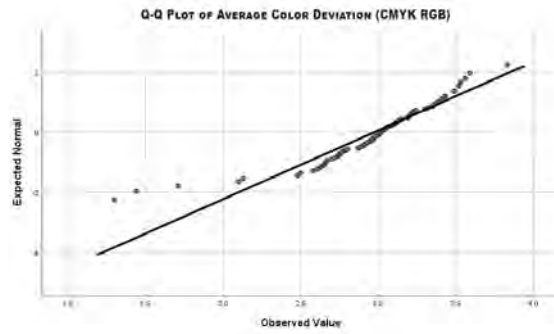
Attributes/Variables	Statistics	Standard Error
Average Color Deviation [ACD (CMYK RGB)]	2.978	0.048
Acceptable ACD Threshold $\Delta E_{(2000)}$	≤ 3.00	
Median (Med) of ACD	3.015	
Standard Deviation (SD)	0.437	
Skewness	-1.509	0.269
Kurtosis	3.931	0.532

The ND curve is not symmetrical around the mean (average) but it is skewed to the left (see Figure 15) showing that the average of color deviation (ACD) is lower than the median of ACD ($\bar{X} = 2.978$, Med = 3.015, SD = 0.437). GRACoL 2013 guidelines indicate the acceptable ACD is 3.00 ($\Delta E_{(2000)} \leq 3.00$). Most of the printed jobs produced $\Delta E_{(2000)} \leq 3.00$. The ACD values are more frequent in occurrence to the left (see Figure 15) than the right of \bar{X} . The Standard Error (Std Err or SE) is 0.048 of ACD. It determines the reliability/accuracy of the average ACD of the CMYK RGB colors in the process. A small SE is an indication that the produced average is a more accurate reflection of the actual population mean. A larger sample size will normally result in a smaller SE while the SD is not directly affected by sample size. Further normality validation was performed by visually evaluating the ACD of CMYK RGB values by plotting in the Quantile-Quantile (Q-Q) chart (see Figure 16). It plots the quantiles of ACD values (values that split a dataset into equal portions) of the dataset instead of every individual data point of the collected data. Also, Q-Q plot is easier to interpret when there is a large sample size (in this case, N = 100, n = 80).



» **Figure 15:** Normal Distribution Curve of ACD of CMYK RGB Colors

The skewness of the ND is -1.509 (with SE 0.048) and it is interpreted as the data is not symmetrical. It is negatively skewed (-1 and -0.5). The kurtosis of the ND of the ACD of CMYK RGB colors of the process is 3.931 (with SE 0.532). The distribution of ACD of CMYK RGB colors is leptokurtic (Kurtosis of > 3) because this type of distribution is longer and tails are fatter. The peak of the curve is higher and sharper, which means that data are heavy tailed or there is a profusion of outliers. If the kurtosis is +1.00 of the ND of the ACD of CMYK RGB colors, then the distribution would be too peaked; if there is an indication of -1.00 of the ND of the ACD of CMYK, the distribution would be too flat. Distributions exhibiting skewness and/or kurtosis that exceed these guidelines are considered non-normal (Hair et al., 2017), which the CMDPW was expected to produce. In the graphs (see Figures 15 & 16), normal distribution does not appear as a bell shape curve and Q-Q plot represents almost a straight line (see Figure 16).



» **Figure 16:** Q-Q Plot of ACD of CMYK RGB Colors in a CMDPW

The average and range control charts analysis was applied for further determining the process (CMDPW) ACD consistency ($\Delta E_{(2000)}$). The SPSS application was used to calculate/construct the graphs of the control limits of average (X-Bar) and range variation. The control limit (CL x-double bar), upper control limit (UCL x-bar) and lower control limit (LCL x-bar) values associated with the ACD (CMYK RGB) variations of the CMDPW are compiled in Table 7.

Differences were found in the ACD of CMYK RGB values of printed colors when comparing with the GRACoL standards. However, overall the process was consistent from day to day over a period of 100 days (see Figure 17) and concluded to be in-control.

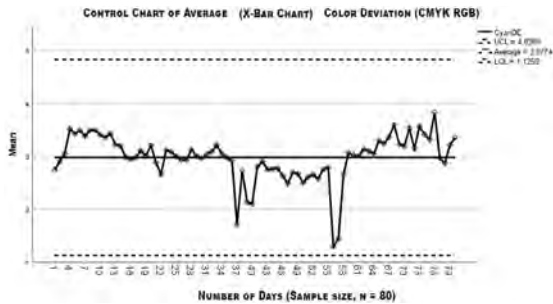
Table 7

Average Color Deviation (ACD) or Color Variation [$\Delta E_{(2000)}$] of Printed Samples in a CMDPW

Color Attributes/Variable	Printed Sample n = 80 Mean (average) n _i = 7	Printed Samples n = 80 Std. Deviation n _i = 7
Mean Color Deviation [$\Delta E_{(2000)}$] of CMYK RGB	2.978	0.437
Printed Samples Average Color Deviation Control Limits		
UCL \bar{X}	4.828	
CL (X-Double Bar)	2.978	
LCL \bar{X}	1.125	

The average color deviation [$\Delta E_{(2000)}$] X-Bar (average) and R (range) variation were monitored by comparing them to calculated tolerances (control limits of the process). If the variations are within the tolerances, then the ACD of CMYK RGB colors are accepted. If the variations are not within the established tolerances, then they are not accepted. The X-Bar chart illustrates how the average color deviation of CMYK RGB varied over a period of time (100 days), while the R-Chart illustrated the dispersion (variation) within the samples studied (monitored).

These charts have three lines parallel to the x axis, while the average values are parallel to the y axis. The average and range color deviation [$\Delta E_{(2000)}$] values (see Figures 17 and 18) fall closely along the control limit (CL) line (within the control limits) or below the CL indicating the ACD of the process was very consistent. ACD less than CL (Average Printed $\Delta E_{(2000)} = 2.978$) is an indication of lower color deviation between the printed and reference.



» **Figure 17:** Control Chart of Average Color Deviation of CMYK RGB in a CMDPW

ACD range variation

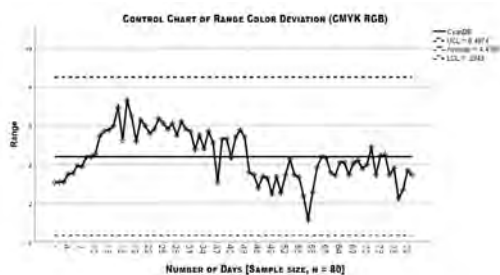
The control limit (CL r-bar), upper control limit (UCL r) and lower control limit (LCL r) values associated with the color deviation (CMYK RGB) range variation of the CMDPW are compiled in Table 8. The ACD range variations of CMYK printed colors over a period of time are in control (see Figure 18).

Table 8

Average Color Deviation Range Variation [$\Delta E_{(2000)}$] of Printed Samples in a CMDPW

Color Attributes/Variables	Average Maximum $\Delta E_{(2000)}$	Average Minimum $\Delta E_{(2000)}$	Printed Sample n = 80 Range Mean (average)
CMYK RGB	5.49	1.42	4.415

Printed Samples Range Color Deviation Control Limits	
UCL (Range)	8.497
CL (R Bar)	4.415
LCL (Range)	0.334



» **Figure 18:** Control Chart of Color Deviation Range Variation of CMYK RGB in a CMDPW

Summary/Conclusions

This applied research experiment was conducted in a Color Managed Digital Printing Workflow (CMDPW). The workflow was observed and monitored for 100 days in Fall 2020. It was aimed at determining the average color deviation consistency over a period of 100 days. The conclusions of this study are based upon an analysis of colorimetric and densitometric data, visual assessment, and associated findings. The guiding objectives of this study allowed testing of an accepted color management practice to gain a better understanding of the presumptions associated with the application of statistical process control (SPC) in a digital printing environment. The experiment examined the importance of calibration, characterization and the color evaluation processes of the digital press which was capable of printing colors to match or be in proximity of GRACoL 2013 standards. Printed samples from the experiment were measured against the GRACoL 2013 (CGATS21-2-CRPC6) standards in CIE L* a* b* space using CGS-ORIS CertifiedWEB application interface with an X-Rite eye one spectrophotometer. The data collected were run through multiple software applications (MS-Excel/SPSS/Minitab) to apply various statistical methods. Analyzed data from the experiment revealed that the printed colorimetric values were in match (aligned) with the GRACoL 2013 (reference/target). Since the SID values of CMYK colors were in control throughout the process, this enabled the CMDPW to produce consistent acceptable color deviation ($\Delta E_{(2000)}$).

It is evident that integration of device profiles is important in a CMW and it also enables/allows the workflow process to meet specific industry standards of ICC based CMW. This study represented specific printing or testing conditions. The images, printer, instrument, software, and paper that were utilized are important factors to consider when evaluating the results. The findings of the study cannot be generalized to other digital printing workflows. However, the result of this research may be of interest to others when exploring similar methodologies to other printing workflows. The findings determined that only the optical aspects of color are quantitatively analyzable and measurable because humans perceive color subjectively. It will be hard to document and measure the color values we see or detect. Additionally, the implementation of a CMDPW is costly, time consuming and a tedious process. It does, however, benefit those who implement this workflow to get consistent color from device to device. Applied statistical methods and the outcome of the analyzed data enabled the determination of the process consistency (4th C of CMW). It is important to reiterate the fact that having a CMW will not replace the SPC. Employing quality improvement techniques or strategies must be part of any manufacturing process or digital printing. The colorimetric data of this experiment also led to the conclusion that the application of a correct print param-

eters set-up is an important step in a CMDPW in order to output accurate colors of choice for a desired use/purpose. Mismatch of print parameters could result in a color management discrepancy or inconsistency.

References

- Abteu M., Kropi, S., Hong, Y. & Pu, L. (2018) Implementation of Statistical Process Control (SPC) in the Sewing Section of the Garment Industry for Quality Improvement. *AUTEX Research Journal*. 18 (2), 160-172. Available from: doi: 10.1515/aut-2017-0034
- Adams, R. M. & Weisberg, J. B. (2000) *The GATF Practical Guide to Color Management*. Sewickley, GATF Press.
- Blevins, C. (2001) *Let's stop chasing our tail (Densities)*. Denver. Available from: <http://www.newsandtech.com/> [Accessed: 10th January 2006].
- Burnes, B. (2000) *Managing change: A strategic approach to organizational dynamics*. 3rd Edition. London, Financial Times/Prentice Hall.
- Chovancova-Lovell, V. & Fleming, P. D. (2009) Color Gamut – New Tool in the Press-room?. *TAPPI Journal*. 8 (2), 4-11.
- Committee for Graphic Arts Technologies Standards (1993) ANSI/CGATS.4-1993. *Graphic Technology – graphic arts reflection densitometry measurements – terminology, equations, image elements and procedures*. Reston, The Association for Suppliers of Printing and Publishing Technologies.
- Committee for Graphic Arts Technologies Standards (2003) ANSI/CGATS.5-2003. *Graphic Technology – spectral measurement and colorimetric computation for graphic arts image*. Reston, The Association for Suppliers of Printing and Publishing Technologies.
- Fleming, P. D. & Sharma, A. (2002) Color Management with ICC Profiles: Can't live without it So Learn to Live with it. *Gravure Magazine*.
- Fraser, B. (2001) *Out of Gamut: Realizing Good Intentions with Rendering Intents*. creative PRO. Available from: <https://creativepro.com/out-of-gamut-realizing-good-intentions-with-rendering-intents/> [Accessed: 2nd January 2021].
- Glass, G. V. & Hopkins, K. D. (1996) *Statistical methods in education & psychology*. 3rd Edition. Boston, Allyn & Bacon.
- Goodhard, M. M. & Wilhelm, H. (2003) *A New Test Method Based on CIELAB Colorimetry for Evaluating the Permanence of Pictorial Images*. Wilhelm Imaging Research, Inc. Available from: http://wilhelm-research.com/pdf/WIR_CIELAB_TEST_2003_07_25.pdf [Accessed: 20th August 2015].
- Hair, J. F., Hult, G. T. M., Ringle, C. M. & Sarstedt, M. (2017) *A Primer on Partial Least Squares Structural Equation Modeling (PLS-SEM)*. 2nd Edition. Thousand Oaks, Sage Publications.
- International Color Consortium (2009) *About ICC*. Reston, ICC. Available from: <http://www.color.org/> [Accessed: 29th July 2009].
- International Digital Enterprise Alliance (2014) *IDEAlliance Guide to Print Production*. Alexandria, IDEAlliance.
- International Digital Enterprise Alliance (2007) *IDEAlliance Guidelines and Specifications*. Alexandria, IDEAlliance.
- Kipman, Y. (2001) The Role of Quantitative Data in Graphic Arts Production Facilities. In: *IS&T: International Conference on Digital Printing and Industrial Applications 2001, 13-16 May 2001, Antwerp, Belgium*. Red Hook, Curran Associates, Inc. pp. 373-377.
- Mears, P. (1995) *Quality Improvements Tools & Techniques*. New York, McGraw-Hill, Inc.
- Novaković, D. & Avramović, D. (2012) Influence of Printing Surface Attributes on Print Quality in Electrophotography. *Technical Gazette*. 19 (2), 295-301.
- Pnueli, Y. & Bruckstein, A. (1996) Gridless Halftoning: A Reincarnation of the Old Method. *CVGIP: Graphical Model and Image Processing*. 58 (1), 38–64. Available from: doi: 10.1006/gmip.1996.0003
- Raja B. (2002) *Digital Color Imaging Handbook*. New York, CRC Press. pp 372-373.
- Thor, J., Lundberg, J., Ask, J., Olsson, J., Carli, C., Haerenstam, K. & Brommels, M. (2007) Application of statistical process control in healthcare improvement: systematic review. *Quality and Safety in Health Care*. 16 (5), 387-399. Available from: doi: 10.1136/qshc.2006.022194
- Wales, T. (2008) *Paper: The Fifth Color*. Alexandria, IPA Bulletin. Available from: https://idealliance.org/files/2008_03tech.pdf [Accessed: 25th January 2021].
- Wheeler, D. J. & Chambers, D. S. (1992) *Understanding statistical process control*. 2nd Edition. Knoxville, SPC Press.
- Xerox Corporation, Inc. (2009) *FreeFlow Print Server Color Handbook*. Xerox Corporation, Inc. Available from: <http://www.support.xerox.com/> [Accessed: 3rd January 2021].



© 2021 Authors. Published by the University of Novi Sad, Faculty of Technical Sciences, Department of Graphic Engineering and Design. This article is an open access article distributed under the terms and conditions of the Creative Commons Attribution license 3.0 Serbia (<http://creativecommons.org/licenses/by/3.0/rs/>).

Influence of packaging design parameters on customers' decision-making process

ABSTRACT

Many recent research has focused on graphic design and shape of the packaging, and their effects on the customer's decision-making process as two separate categories. Since the shape of the packaging along with the graphic design plays an important role in the visual appearance of the packaging and attracts the customer's attention, the main objective of this research was to find out which packaging shapes and graphic elements customers find most attractive, as well as to understand the general opinion of customers about the influence of packaging aesthetics on their decision-making process when purchasing a product. Methodology of this research was conducted in two stages, from which the first one included creating three different graphic design solutions combined with three shape categories, and three variations of added value, for the same food packaging. The second part of the research covered an online questionnaire, in which a group of 50 people participated. This questionnaire focused on three variables: graphic design of the packaging, packaging shape and its added value. These variables were evaluated using the Likert scale. Through the questionnaire, participants were asked to answer general questions about the impact of the packaging visual appearance and added value, on their decision-making process when buying a product, as well as to choose the most appealing packaging between the given options. The research results showed that customers preferred non-standard packaging shapes and simple graphic design, as well as packaging with added value. The results of this research prove that the aesthetics of packaging has an impact on the customer's perception of a product, which means that packaging plays an important role in product marketing.

KEY WORDS

packaging, graphic design, consumer research, marketing

Minja Malešević 
Mladen Stančić 

University of Banja Luka,
Faculty of Technology,
Department of Graphic
Engineering, Banja Luka,
Bosnia and Herzegovina

Corresponding author:
Minja Malešević
e-mail: malesevicminja@gmail.com

First received: 14.6.2021.

Revised: 26.9.2021.

Accepted: 5.10.2021.

Introduction

The basic function of packaging is to “preserve product integrity” by protecting the actual food product from potential damage due to “climatic, bacteriological and transportation hazards” (Stewart, 1995), as well as to ensure proper storage and to communicate with customers by providing information about the contents (Robertson, 2012). However, the importance of packaging has increased rapidly in recent years, and in addition to

its main functions, packaging plays an important role in attracting customers' interest by increasing their visibility through form and design (Wells, Farley & Armstrong, 2007). According to Giovanneti (1995) cited by Franken (2020), the biggest challenge for designers and companies is to find the optimal design that is preferred by customers and increases recognition in the market. Since packaging can be considered as the medium between the customer and the product and is the first contact with the consumer, it is clear that packaging plays an

important role in persuading the customer. Customers tend to make decisions about the product based on the quality of the packaging, i.e. if the packaging gives the impression of inferior quality, consumers will perceive this as if the product is of inferior quality, even if this is not the case (Underwood, Klein & Burke, 2001). The importance of packaging is constantly increasing due to the ever increasing competition, which means that the product needs to stand out from all other similar products (Morgan, 2016). With this in mind, companies are opting to use various visual techniques to increase customer attention, such as using original materials, shapes and colors for their packaging (Ooijen et al., 2016).

According to Poslon, Kovačević & Brozović (2021), the form of packaging varies depending on the purpose and type of product. Packaging shape not only makes a product more attractive, but can also help consumers predict the volume of the product, and it can also influence the perception of the taste of a product, as the sense of taste can be activated even without consuming the product. The importance of packaging shape also makes itself felt in differentiating products from competitors, as it can trigger emotions and purchase behavior. The more complex and atypical the shape is, the more attention it attracts (Vladić et al., 2015).

Packaging design is often used as a marketing tool to achieve marketing objectives and meet consumer demands. This can be achieved by using the aesthetic and functional components of a packaging. Aesthetic considerations refer to the shape and size, material, colour, text, and graphics of a packaging. Packaging design is not only critical to branding, but also to the function of the packaging. From a marketing perspective, packaging must meet a number of objectives within a marketing strategy: innovative design to attract customer attention, brand identification, facilitation of product transportation and protection of contents, ease of opening and closing, clever dispensing and recallability (Rundh, 2013).

Problem statement

It is known that the role of product packaging is multifaceted. Not only it protects the product, but also transmits the information about the product through its visual elements. Therefore, graphic design of visual packaging elements is one of the most effective means of shaping the aesthetics of a product packaging and attracting the consumer attention. Aesthetic food packaging has a greater chance of eliciting positive responses from consumers, in comparison with standardized packaging (Kovačević, Brozović & Banić, 2020).

Another important aspect of the packaging that is responsible for the visual identity of the packaging is its shape. Even though the shape of the packaging is usually

determined by various factors such as material costs, production and transportation, brand characteristics and product requirements, the shape of the packaging plays an important role in communication. The shape and size of the packaging have a great impact on the customer's decision-making process and can attract or deter them (Bata et al., 2018). People tend to perceive the visual aspects of packaging differently, and all of them trigger different emotions and associations that consumers directly associate with the product. Based on this premise, we hypothesized that packaging design and shape, together with its added value have an important influence on how customers perceive a specific product. With this in mind, this study focused on investigating the relationship between packaging aesthetics and its impact on consumers' emotions and decision-making process.

Methodology

Samples

For this research, three different graphic design solutions and shape categories were created for a fictitious biscuit brand, *Cakers*. The different packaging shapes were created using the software Engview Packaging Design, while the graphic design solutions were created using Adobe Illustrator. The packaging shapes used in this study are triangular (Figure 1), pentagonal (Figure 2) and square (Figure 3).

The graphic solutions used the standard brand colors (yellow, brown, white) in all three solutions. All the designed solutions also included an image of the biscuit and the main elements of the food product's packaging, such as the brand name, the product description, the weight, the bar code, the nutritional tables, the expiry date, etc.

For the first graphic solution, yellow was used as the primary color, occupying half the height of the packaging. The yellow background is covered with brown round shapes, symbolizing the chocolate chips contained in the cookies. The second graphic solution consists of a neutral beige background covered with yellow and white round shapes. The basic color (yellow) was also used as the background color in the third graphic solution. In this case, the yellow color is used as a background for the white cross-line pattern, which is located in the lower part of the packaging. The first and second design solutions differ from the third in additional features that might be of interest to customers. Namely, the first solution is a multisensory packaging, as customers have the opportunity to smell the product contained in the packaging, by rubbing the image of the biscuit on the front of the packaging. The second graphic solution, in addition to the basic elements, also includes elements



» **Figure 1:** Triangular packaging in three different graphic designs



» **Figure 2:** Pentagonal packaging in three different graphic designs



» **Figure 3:** Square packaging in three different graphic designs

for personalization, on which it is possible to write for whom the packaging or product is intended. All graphic solutions were applied to all three packaging forms.

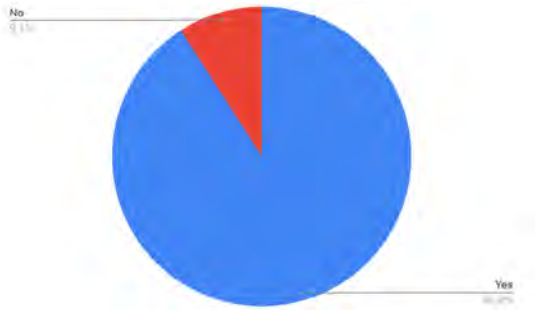
Participants and procedures

The research was conducted using an online questionnaire Google Forms in which 50 participants were asked to rate the attractiveness of each packaging on a scale of 1 to 5 and to answer several questions about the overall influence of the packaging on their decision-making

process. 60% of the participants were women, the rest were men in the age group of 25 to 35 years.

Results

In order to investigate whether the appearance of the packaging influences the decision-making process of customers when buying a product, participants were asked to answer the question “Do you pay attention to the packaging when buying a product?”.

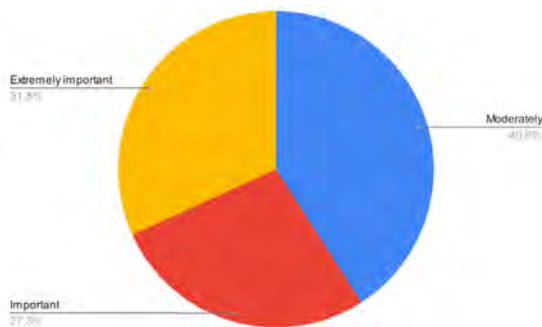


» **Figure 4:** Ratio of participants who pay attention to the packaging when buying a product

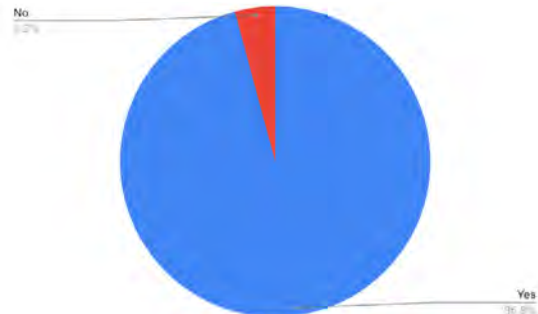


» **Figure 6:** Ratio of participants' interest in the possibility of personalizing packaging

To understand the value that the visual design of the packaging has for the customers, the participants were asked to answer the question "How important is the visual design of the packaging for you?". 40.9% of participants answered that visual design is moderately important, 27.3% answered that visual design is important to them, while 31.8% of participants answered that visual design of packaging is very important to them when they purchase a product (Figure 5). As with the previous question, most of the participants who think that the visual design of the packaging is important were women.



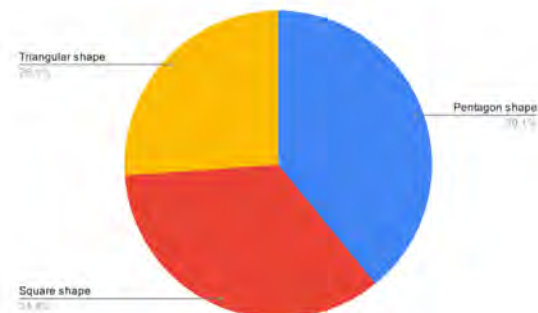
» **Figure 5:** Ratio of participants with regard to the importance of the visual design of the packaging



» **Figure 7:** Ratio of participants' interest in multisensory packaging

In addition to choosing between the given packaging forms, participants were asked to select the one they found most visually appealing among the given graphic solutions (Figure 9). 52.5% of the participants chose the second graphic solution as their favorite, 39.1% preferred the first graphic solution, while 8.7% of the participants chose the third graphic solution as their favorite.

Since the first and second biscuit packaging are packaging with additional functions (possibility of personalizing the packaging and multisensory packaging), participants were asked to answer the questions "Do you find packaging with the possibility of personalization interesting?" and "Do you find multisensory packaging interesting?". All participants answered "Yes" to the first question (Figure 6), while 95.8% of them answered "Yes" and 4.2% answered "No", to the second question (Figure 7).



» **Figure 8:** The participants' choice of the most visually attractive form of packaging

After answering these general questions about the visual appearance of the packaging, participants were asked to choose the one they found most visually appealing among the given packaging shapes (triangular, pentagonal, square). 39.1% of the participants chose the pentagonal shape as the most visually appealing, while 34.8% chose the standard square shape and 26.1% of them chose the triangular shape (Figure 8).

Discussion

According to the participants, the most attractive combination of graphic design and packaging shape is the pentagonal packaging with the second graphic design solution, which also offers the possibility of



» **Figure 9:** Graphic design solutions for biscuit packaging

personalization (Figure 10). This research showed that aesthetics have an impact on customers' perception of the packaging and their decision-making process. Another interesting result was that customers find packaging with additional functions more attractive and interesting than packaging without additional functions. The results on the packaging shape chosen showed that customers found non-standard cookies packaging shapes such as pentagonal more visually appealing. According to the participants, the simple graphic design with a soft color palette and an appealing cookie image was more attractive than the line cross pattern and the symbolic chocolate chip illustration.



» **Figure 10:** Most visually appealing graphic design and shape of the biscuit packaging, in the opinion of the participants

Conclusion

In conclusion, this research shows that the visual appearance of packaging plays an important role in successful marketing. It was noticed that soft color palette, simple geometric shapes and appealing product photographs are more appealing than abstract patterns and symbolic images. Non-standard geometric shapes attract customers' interest more than standard shapes. The results of this research also show that packaging with added value,

especially packaging with the possibility of personalization, is very attractive. All these findings can be used as guidelines for food packaging design. Although the research conducted provides important information on visual guidelines for packaging, it should be noted that some results might be different in different age groups and for different products, as the research was conducted on a limited age group between 25 and 35 years and on a single food product (cookie). Considering this, there is a possibility that the participants were subjective due to their general (dis)preference for the product. It should also be noted that participants were surveyed via an online questionnaire, which may be limited due to differences in color representation on screens. Further studies on different foods and in different age groups are planned to further investigate the current results.

References

- Bata, J., Hanzer Jamnicki, S., Banić, D. & Brozović, M. (2018) Compression resistance of small paper-board packaging shapes. In: Kašiković, N. (Ed.) *Proceedings - The Ninth International Symposium on Graphic Engineering and Design, GRID 2018, 08-10 November 2018, Novi Sad, Serbia*. Novi Sad, Faculty of Technical Sciences. pp. 237-242.
- Franken, G. (2020) Packaging design and testing by eye tracking. In: Dedijer, S. (Ed.), *Proceedings - The Tenth International Symposium on Graphic Engineering and Design, GRID 2020, 12-14 November 2020, Novi Sad, Serbia*. Novi Sad, Faculty of Technical Sciences. pp. 347-354.
- Kovačević, D., Brozović, M. & Banić, D. (2020) Applying graphic design principles on tea packaging. In: Dedijer, S. (Ed.), *Proceedings - The Tenth International Symposium on Graphic Engineering and Design, GRID 2020, 12-14 November 2020, Novi Sad, Serbia*. Novi Sad, Faculty of Technical Sciences. pp. 571-575.
- Morgan, T. (2016) *Visual Merchandising*. London, Laurence King Publishing.
- Ooijen, I., Franssen, M. L., Verlegh, P. W. J. & Smit, E. G. (2016) Atypical food packaging affects the persuasive impact of product claims. *Food Quality and Preference*. 48 (A), 33-40. Available from: doi: 10.1016/j.foodqual.2015.08.002.

-
- Poslon, S., Kovačević, D. & Brozović, M. (2021) Impact of packaging shape and material on consumer expectations. *Journal of Graphic Engineering and Design*. 12 (2), 39-44. Available from: doi: 10.24867/JGED-2021-2-039.
- Robertson, G. L. (2012) *Food Packaging: Principles and Practice*. Boca Raton, CRC Press.
- Rundh, B. (2013) Linking packaging to marketing: how packaging is influencing the marketing strategy. *British Food Journal*. 115 (11), 1547-1563. Available from: doi: 10.1108/BFJ-12-2011-0297.
- Stewart, B. (1995) *Packaging as an Effective Marketing Tool*. Surrey, Pira International.
- Underwood, R. L., Klein, N. M. & Burke, R. R. (2001) Packaging communication: attentional effects of product imagery. *Journal of Product & Brand Management*. 10 (7), 403-422. Available from: doi: 10.1108/10610420110410531.
- Vladić, G., Kecman, M., Kašiković, N., Pal, M. & Stančić, M. (2015) Influence of the shape on consumers' perception of the packaging attributes. *Journal of Graphic Engineering and Design*. 6 (2), 27-32.
- Wells, L. E., Farley, H. & Armstrong, G. A. (2007) The importance of packaging design for own-label food brands. *International Journal of Retail & Distribution Management*. 35 (9), 677-690. Available from: doi: 10.1108/09590550710773237.



Per-pixel displacement mapping using cone tracing with correct silhouette

ABSTRACT

Per-pixel displacement mapping is a texture mapping technique that adds the microrelief effect to 3D surfaces without increasing the density of their corresponding meshes. This technique relies on ray tracing algorithms to find the intersection point between the viewing ray and the microrelief stored in a 2D texture called a depth map. This intersection makes it possible to determine the corresponding pixel to produce an illusion of surface displacement instead of a real one. Cone tracing is one of the per-pixel displacement mapping techniques for real-time rendering that relies on the encoding of the empty space around each pixel of the depth map. During the preprocessing stage, this space is encoded in the form of top-opened cones and then stored in a 2D texture, and during the rendering stage, it is used to converge more quickly to the intersection point. Cone tracing technique produces satisfactory results in the case of flat surfaces, but when it comes to curved surfaces, it does not support the silhouette at the edges of the 3D mesh, that is to say, the relief merges with the surface of the object, and in this case, it will not be rendered correctly. To overcome this limitation, we have presented two new cone tracing algorithms that allow taking into consideration the curvature of the 3D surface to determine the fragments belonging to the silhouette. These two algorithms are based on a quadratic approximation of the object geometry at each vertex of the 3D mesh. The main objective of this paper is to achieve a texture mapping with a realistic appearance and at a low cost so that the rendered objects will have real and complex details that are visible on their entire surface and without modifying their geometry. Based on the ray-tracing algorithm, our contribution can be useful for current graphics card generation, since the programmable units and the frameworks associated with the new graphics cards integrate today the technology of ray tracing.


KEY WORDS

Real-time rendering, texture mapping, per-pixel displacement mapping, ray-tracing, cone tracing, silhouette correction, quadratic approximation

Adnane Ouazzani

Chahdi¹ 

Anouar Ragragui¹ 

Akram Halli² 

Khalid Satori¹

¹Sidi Mohamed Ben Abdellah University, Faculty of Science Dhar EL Mahraz LISAC Laboratory, Fez, Morocco

²Moulay-Ismaïl University FSJES-UMI OMEGA-LERES Laboratory Meknes, Morocco

Corresponding author:

Adnane Ouazzani Chahdi

e-mail:

adnaneouazzanichahdi@gmail.com

First received: 20.6.2021.

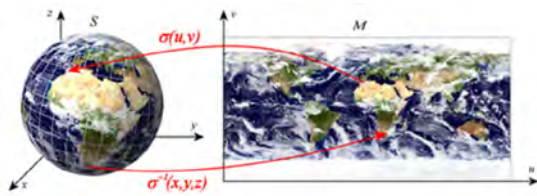
Revised: 22.9.2021.

Accepted: 24.9.2021.

Introduction

Per-pixel displacement mapping (Patterson, Hoggart & Logie, 1991) is a technique based on texture mapping (Catmull, 1974; Blinn & Newell, 1976). It is inspired at the same time by bump mapping (Blinn, 1978; Peercy, Airey & Cabral, 1997) that proceeds on pixels of the microreliefs

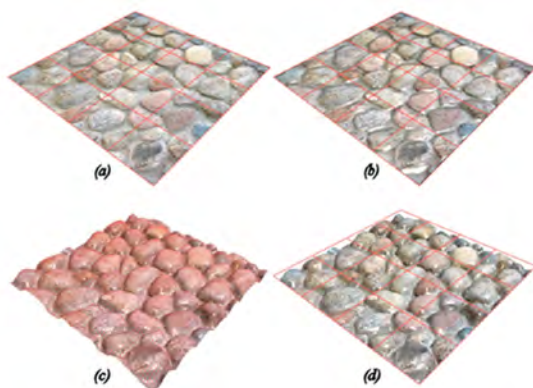
texture, and the displacement mapping (Cook, 1984) that proceeds on the vertex of the 3D mesh. Texture mapping associates a two-dimensional image with a three-dimensional surface using a function called parameterization. This function maps each vertex (x, y, z) of the mesh surface, with a pair of coordinates (s, t) representing a pixel of the texture (Figure 1).



» **Figure 1:** Parameterization $\sigma(u, v)$ and inverse parameterization $\sigma^{-1}(x, y, z)$ matching a surface S of R^3 with the domain M of R^2

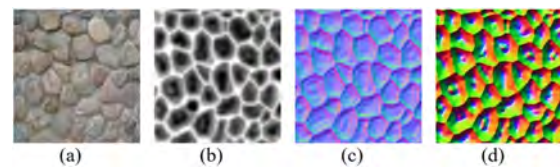
Texture mapping does not produce any microrelief effects and the colors of the pixels representing the object in the scene always remain the same regardless of the lighting conditions (Figure 2a). To solve this problem, Blinn introduced bump mapping (Blinn, 1978) based on the disturbance of the surface normals in the function of a depth map (Figure 3b). The disruption of normals produces an illusion of small displacements and produces a microrelief effect (Figure 2b). The displacement mapping uses the depth map in another way. It consists of displacing the vertices of the surface according to the values stored in the depth map. For this, the mesh must be subdivided so that it adapts to the texture resolution (depth map), which generates a lot of graphic primitives (vertices and polygons) to be processed (Figure 2c). The main goal of per-pixel displacement mapping is to have the same rendering as displacement mapping but without increasing the density of the base mesh (Figure 2d). It consists of reducing the number of graphics primitives while retaining the overall visual quality of the scene.

Figure 2 shows the difference between texture mapping techniques. As shown in the figure, the mesh density is the same in images (a), (b), and (d) but per-pixel displacement mapping allows rendering very detailed geometry. And compared to displacement mapping (c), per-pixel displacement mapping produces the same result but at a very low cost.



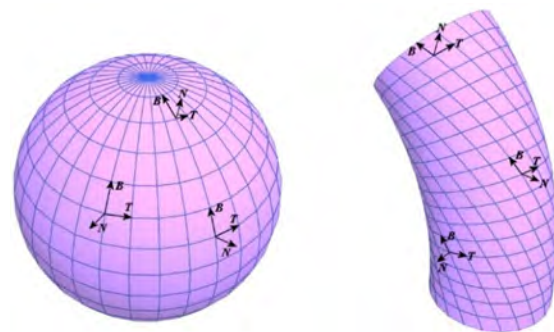
» **Figure 2:** Comparison of the different texture mapping techniques (Halli et al., 2008). (a) Texture mapping. (b) Bump mapping. (c) Displacement mapping. (d) Per-pixel displacement mapping

Per-pixel displacement mapping is based on three main elements: the displacement map, the tangent space, and the ray-tracing algorithm. The displacement map (Figure 3) is a two-dimensional image whose pixels are not used to store colors, but geometrical data (i.e. depths and normals). In the α channel, we store the depths associated with the microrelief mapped on the 3D surface. The other three channels: red, green, and blue, are used to store the three x , y , and z components of the normal, which are calculated from the depths. Since the z component of the normal can be retrieved as a function of the two others, the blue channel can be released to store other data used by certain techniques such as cone tracing. In this case, the displacement map can be named according to this technique (i.e. the Cones Map as shown in Figure 3d).



» **Figure 3:** (a) The corresponding texture. (b) The depth map. (c) The components x , y , and z of the normal. (d) A cones map that stores the depths in the α channel, the x and y components of the normal are stored in the red and green channels, and the blue channel stores the cones' radius

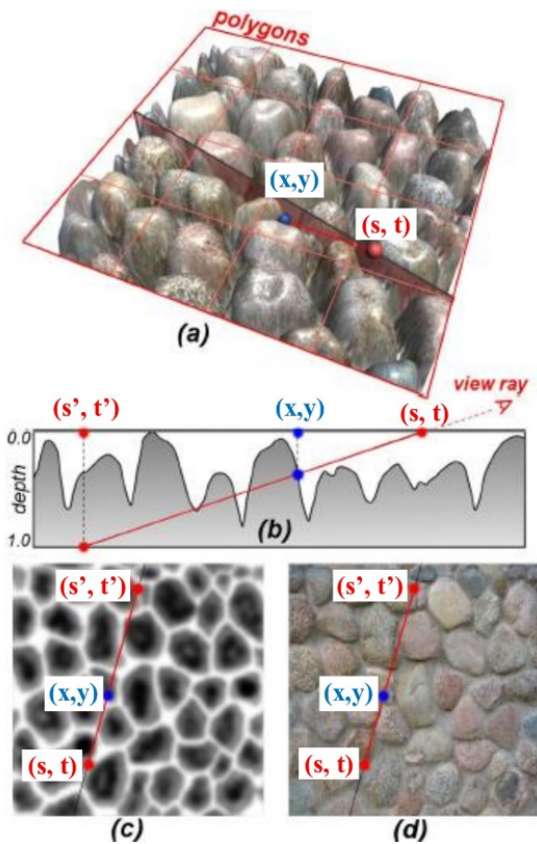
As shown in figure 4, the tangent space is a local space associated with each vertex constituting the 3D mesh (Peercy, Airey & Cabral, 1997). It is calculated using the normal to the vertex and the associated texture coordinates. The viewing ray vector and the light vector must be expressed in this space.



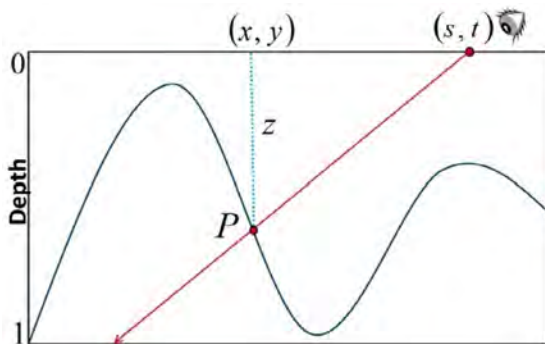
» **Figure 4:** Tangent space. It is a local space constituted by three vectors: the normal, binormal, and tangent associated with each vertex of the 3D mesh

Ray tracing is an algorithm that searches the intersection of the viewing ray and the microrelief stored in the displacement map (Figure 5 and Figure 6). This search is performed in texture space for each pixel resulting from the 3D mesh. The main problem of per-pixel displacement mapping is to find the first intersection point.

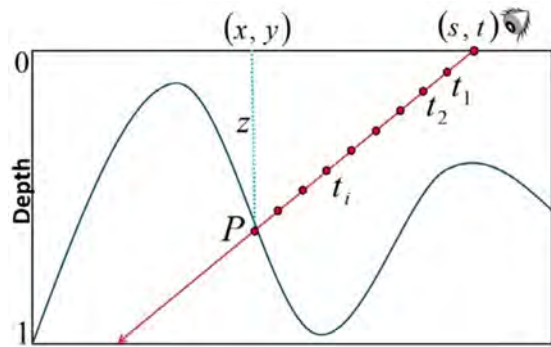
As shown in figures 5 and 6, the first intersection is represented by the point P along the viewing ray V. So, to have an illusion of relief displacement, the fragment (s, t) will be textured using the texel (x, y) instead of (s, t).



» **Figure 5:** Ray tracing in the depth map (Halli et al., 2008). (a) 3D view of the ray tracing. (b) The relief's slice including the viewing ray. (c) The depth map. (d) The corresponding texture. (s,t) is the starting point. The main problem of per-pixel displacement mapping is to find the first intersection (x,y) of the viewing ray and the microrelief. So, the fragment (s,t) will be textured using the texel (x,y) instead of (s,t)



» **Figure 6:** Ray tracing in the depth map. The first intersection point between the viewing ray and the microrelief is the P(x, y, z)



» **Figure 7:** Search for the intersection with iterations (Linear search). The number of iterations and the size of the displacement step must be defined in advance. The t_i parameter represents the sum of the step size at iteration i

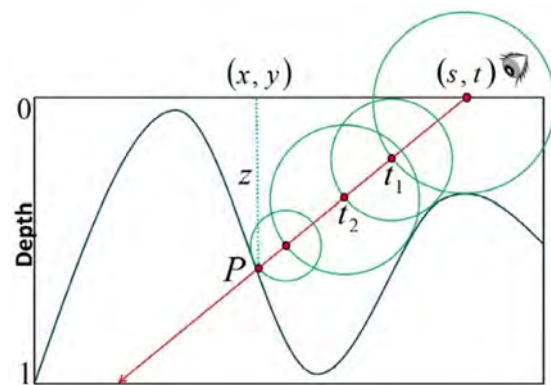
As shown in figures 5 and 6, the point P can be expressed as follows:

$$P = Vt \quad (1)$$

The speed constraint does not allow an exact search, which makes it necessary to find a point as close as possible to the intersection point. The different approaches to performing this search are presented in (Szirmay-Kalos & Umenhoffer, 2008). To better locate the first intersection, the number of iterations is predefined in advance. The size of the displacement step is defined according to the technique used, which can be constant (Figure 7) or variable (Figure 8). During the search for the intersection, we use the following general formulas:

$$t_{i+1} = t_i + \text{step} \quad (2)$$

$$P_{i+1} = vt_{i+1} \quad (3)$$



» **Figure 8:** Search for the intersection with iterations and with an encoding of the empty space (Sphere tracing). The number of iterations must be defined in advance and the size of the displacement step is calculated as a function of the sphere parameters encoded in a pre-processing stage. The t_i parameter represents the sum of the step size at iteration i .

Where v is the normalized viewing ray vector expressed in the texture space having a normalized depth (i.e. v/v_z) involving $v_z=1$.

These two formulas are used together to determine the point P_{i+1} . At iteration $i+1$, the parameter t_{i+1} makes it possible to determine the position of the point P along with vector v , and the step parameter makes it possible to determine its displacement, the value of which is calculated according to the used technique.

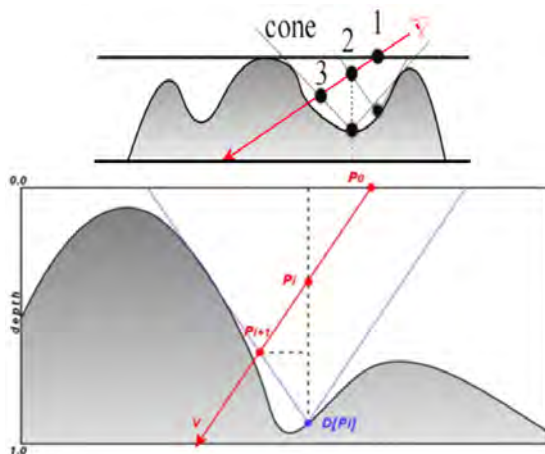
We note that the viewing ray is reversed during the search for the intersection. It means that we start from the eye (camera) towards the microrelief.

Contribution

Per-pixel displacement mapping suffers from three main problems, namely, the time to compute the displacement map, the search of the intersection between the viewing ray and the microrelief stored in the displacement map, and the treatment of the silhouette.

The preprocessing is the phase in which we calculate a displacement map for each texture. The computing speed depends on the used algorithm. An improvement has been proposed in (Halli et al., 2008) which consists of using linear algorithms instead of quadratic ones and which has considerably increased the computing speed.

To find the intersection point, we use ray-tracing algorithms. The best technique in this sense is cone tracing (Figure 9).

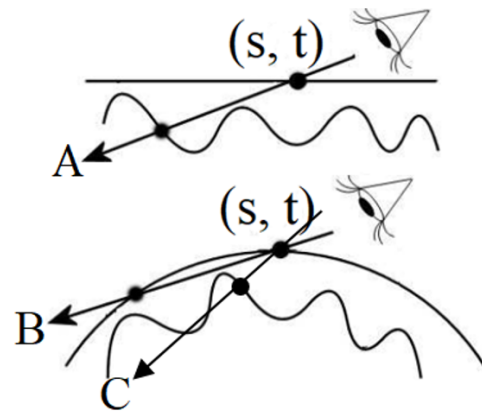


» **Figure 9:** Cone tracing on the displacement map. At each iteration, the next position P_{i+1} of the viewing ray v is calculated as a function of the current position P_i and the cone parameters which are the height $D[P_i]$ and its radius.

This technique relies on the encoding of the empty space to converge more quickly. This space is stored in a texture

called a cones map (Figure 3d). Improvements concerning the search of the intersection (ray-tracing algorithm) have been proposed in (Halli et al., 2008; Ouazzani Chahdi et al., 2017; Ouazzani Chahdi et al., 2018).

Despite the improvements proposed in (Halli et al., 2008; Ouazzani Chahdi et al., 2017; Ouazzani Chahdi et al., 2018), the silhouette problem persists. The silhouette is visible at the edges of the 3D object (Figure 10, Figure 11). To explain this problem, we have Figure 10 which shows a flat and curved surface. For flat surfaces, the viewing ray always pierces the reliefs (Ray A), that is to say, there we will always have an intersection. But for curved surfaces, sometimes the viewing ray does not pierce the relief (Ray B), that is to say, there is no intersection. Then, the ray tracing algorithm will not find an intersection point or it will find an erroneous one, and in this case, the pixel must be discarded to be able to have a correct treatment of the silhouette.

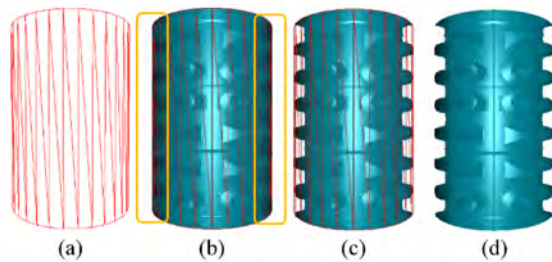


» **Figure 10:** Highlighting the silhouette problem. (top) a flat surface always allows us to have an intersection with the relief. (bottom) with a curved surface, the viewing ray can leave the surface without piercing the relief. The pixel (s,t) in this case belongs to the silhouette

The main contribution proposed in this paper compared to the improvements proposed in (Halli et al., 2008; Ouazzani Chahdi et al., 2017; Ragragui et al., 2017; Ouazzani Chahdi et al., 2018; Ragragui et al., 2018a; Ragragui et al., 2018b; Ragragui et al., 2020) is the resolution of the silhouette problem.

Indeed, as shown in Figure 11b, the cone tracing technique does not support the treatment of the silhouette. Based on this observation, this paper presents two new cone-tracing algorithms based on a quadratic approximation at each vertex of the 3D mesh (Jean, 2002; Oliveira & Policarpo, 2005). The first algorithm consists of rectifying the viewing ray after each new displacement (after the cone tracing), and the second one consists of rectifying the cone before each new displacement (before the cone tracing).

Figure 11 shows a comparison of a cylinder rendered with the cone tracing technique without and with correction of the silhouette and by highlighting the polygonal mesh. We notice that the silhouette is not visible on the 3D object when rendered without the correct silhouette (Figure 11b); this problem is surmounted by exploiting the parameters of the quadratic surface to take into account the curvature of the 3D object. Figure 11c and Figure 11d show the same 3D model rendered by our approach that provides a correct rendering.



» **Figure 11:** Rendering of a cylinder with cone tracing techniques. (a) Basic mesh using 56 triangles. (b) Without the correct silhouette (original technique). (c), (d) With correct silhouette (proposed technique). We notice in (b) that the surface of the cylinder and the reliefs are confused. This problem has been solved by our approach in (c, d)

Contrary to the displacement mapping, the silhouette is generated without needing to change its geometry and by using a minimal number of triangles (Figure 11a). Figure 12 shows an example of a scene that can be realized by the contribution of this paper.



» **Figure 12:** Rendering of a scene by the relaxed cone mapping with the correct silhouette

The main advantage of our contribution is that it can be integrated into the new graphic card units. Indeed, the programmable pipeline model for ray tracing has been introduced in (Parker et al., 2013). Currently, the frameworks and the programmable units associated with the new graphics cards integrate a programmable GPU-accelerated ray-tracing that provides a simple, recursive, and flexible pipeline for accelerating ray-tracing algorithms.

Related Works

The displacement mapping was introduced in (Cook, 1984). It consists of displacing each vertex of the 3D mesh according to the normal with a value given by the height map. To have better rendering quality, the basic mesh must be subdivided into sub-polygons to be adapted to the height map resolution, which leads to a very high number of primitives processed by the graphic cards.

Contrary to the displacement mapping, which changes the geometry (Cook, 1984), the bump mapping occurs only at the level of the shading (Blinn, 1978; Peercy, Airey & Cabral, 1997). The latter being a function of the normals, the disruption of this one will cause a microrelief illusion. So instead of creating the displacement surface, just calculate its normal and use it in a shading formula to simulate the surface details. When it comes to miniature reliefs, this technique produces a satisfactory rendering, but it is limited for shading and self-occlusion. For a large elevation of reliefs, the per-pixel displacement mapping has been proposed in (Patterson, Hoggar & Logie, 1991). For shading, the use of a horizon map has been introduced in (Max, 1988; Sloan & Cohen, 2000).

To avoid the calculation of the normal during the rendering stage, a normal mapping has been introduced in (Peercy, Airey & Cabral, 1997) that consists of storing the normals of the microrelief in a texture called: normal map. For real-time rendering, several implementations have been proposed in (Ernst et al., 1998; Kilgard, 2000; Sung Kim, Hyun Lee & Ho Park, 2001; Lee et al., 2007).

Parallax mapping is an extension of the bump mapping (Kaneko et al., 2001; Welsh, 2004; McGuire & McGuire, 2005; Premecz, 2006). This technique performs an approximate search for the intersection between the viewing ray and the relief contained in the displacement map. This point is defined by the intersection of the viewing ray and the horizontal line, which passes through the height of the relief at the current point. The main advantage of this technique is the addition of the parallax effect. However, it is limited to irregular microrelief. Improvements were introduced in (Brawley & Tatarchuk, 2004; Tatarchuk, 2006) to manage the shading correctly.

Relief mapping introduced in (Policarpo, Oliveira & Comba, 2005; Policarpo & Oliveira, 2006) is based

on relief texture mapping (Oliveira, 2000; Oliveira, Bishop & McAllister, 2000). This technique calculates the intersection point by two stages, in the first one, it determines the interval where the first intersection is located, and in the second one, the intersection point is refined using a binary search.

The binary search does not take into account the depths of the microrelief. To overcome this problem, a linear search coupled with a secant one makes it possible to converge even more quickly by using the depths of the microrelief (Brawley & Tatarchuk, 2004; Yerex & Jagersand, 2004; Tatarchuk, 2006). An improvement of the relief mapping technique presented in (Ouazzani Chahdi et al., 2018) consists of choosing the number of iterations dynamically according to the relief's depth.

To converge rapidly towards the first intersection point, Donnelly introduced the notion of coding a conservative space in the sphere tracing technique (Donnelly, 2005). This is the first method that is based on the calculation of the empty space to converge quickly to the first intersection. This space is calculated during the preprocessing stage and during the rendering stage, a sphere tracing allows each iteration to approach significantly the first intersection with the relief.

The cylinder tracing was introduced in (Baboud & Decoret, 2006a). The preprocessing stage of this technique defines for each pixel of the depth map, a radius of a cylinder inside which, no viewing ray can pierce the relief more than once. During the search for the intersection, this radius allows moving forward without the risk of skipping the first intersection. The second step is to perform a binary search between the last two positions.

The cone tracing technique introduced in (Paglieroni & Petersen, 1994; Dummer, 2006; Policarpo & Oliveira, 2007) proposed to calculate the empty space as a form of top-opened cones using 2D texture. The technique has been proposed in two versions, the conservative technique (Paglieroni & Petersen, 1994; Dummer, 2006) and the relaxed one (Policarpo & Oliveira, 2007). Both versions were subsequently improved in (Halli et al., 2008). These improvements consist firstly of using linear algorithms $O(n)$ instead of quadratic ones $O(n^2)$ to compute the conservative and the relaxed cone. Secondly, calculating and storing the cones' radius instead of the cones' ratios thereby having cone angles to the order of $\pi/2$ rather than $\pi/4$, and finally extending the technique to support the non-square texture using elliptical rectification of cones during the rendering stage.

The third version of the cone has been proposed in (Ouazzani Chahdi et al., 2017), it consists of using a hybrid cone which is located between the conservative and the relaxed one so that the cone tracing pierces the relief only once and without the need for binary research.

Another way to calculate the empty space around a texel is to use a dilatation and an erosion map (Kolb & Rezk-Salama, 2005). These two maps are calculated from the depth map and allow having at each texel a secure region. The successive intersections of the viewing ray with these regions make it possible to converge to the intersection point.

Pyramidal displacement mapping introduced in (Oh, Ki & Lee, 2006; Tevs, Ihrke & Seidel, 2008) makes it possible to create a pyramidal structure of the depths by calculating in each time a map that is four times smaller than the previous one and taking the maximum of the depth of each group of four pixels. The intersection point between the viewing ray and the depths is obtained by the successive intersections with the horizontal lines representing the maximum depth of each level of the pyramid.

Per-pixel extrusion mapping consists of extruding the 3D models according to a binary form stored in a 2D texture without perturbing the basic mesh (Halli et al., 2009). The empty space is calculated by using the Euclidean Distance Transform EDT described in (Danielsson, 1980) and stored in a 2D texture called distance map, the normals of the extruded form are calculated from this later. The binary form, the distance map, and the normals are stored in a 2D texture called a shape map. Improvements were proposed to correct the intersection point between the viewing ray and the extruded form and to extend the extrusion algorithm for creating the outline extruded surfaces (Ragragui et al., 2017).

The algorithms of extrusion and revolution have been combined with a shape box to create extruded and revolved 3D objects without polygonal meshes (Halli et al., 2010). The two algorithms are based on the shape map. The extrusion consists of lifting the 2D binary form stored in the shape map, on the other hand, the revolution uses this one to create a revolved object around a revolution axis. For the texturing of revolved objects, we use one of the two projections, cylindrical or spherical. A rectification concerning these two types of projection has been proposed in (Ragragui, et al., 2018b).

3D objects created by extrusion or by revolution do not present any microrelief effect, that is to say, they are textured by the classic texture mapping technique. To solve this problem, two improvements have been proposed, one for extrusion (Ragragui et al., 2020) and the other for revolution (Ragragui et al., 2018a), which consists of making a combination with the bump mapping technique.

To manage the silhouette, four approaches have been proposed. The silhouette of an object is visible on the edges of the associated 3D mesh.

The first solution is to use a local representation of the 3D surface at each vertex. Two local representations

have been proposed. The first consists of using a quadratic approximation represented by two parameters (Jean, 2002; Oliveira & Policarpo, 2005). And the second consists of using a local space for each vertex (Chen & Chang, 2008; Na & Jung, 2008). The two representations are calculated and associated with each vertex during the preprocessing stage. During the rendering stage, the solution adopted makes it possible to determine the fragments belonging to the silhouette.

Shell mapping proceeds to the extrusion of each triangle of the mesh according to the normals of its three vertices (Hirche et al., 2004). The extrusion gives a prism constituted by eight triangles that will have to be included in the rendering stage. To avoid some discontinuity defects related to the bilinear interpolation, the prism is subdivided into three tetrahedrons using an algorithm described in (Shirley & Tuchman, 1990). The use of barycentric coordinates introduced in (Porumbescu et al., 2005) makes it possible to define a relation between each 3D point contained in the prism, and a single texel in the 3D displacement map. The use of semi-transparent 3D textures allows supporting some more advanced functionalities (Dufort, Leblanc & Poulin, 2005). A smoothing function coupled with the patches of coons makes it possible to eliminate strongly the distortions, and thus produces very satisfactory results (Jeschke, Mantler & Wimmer, 2007).

View-dependent displacement mapping (Wang et al., 2003; Wang et al., 2004) consists of calculating, for each viewing ray, the distance between each point of a polygon and the displacement surface. To be able to manage the silhouette, the curvature of the base surface must also be taken into consideration. A five-dimensional is thus defined to store the texture coordinates, the spherical coordinates of the viewing ray, and the curvature index of the surface along the viewing ray. This function represents a large amount of data, for this reason, it is compressed and stored as a 3D texture.

Image-based modeling and rendering techniques (IBMR) allow creating entire 3D objects without polygonal meshes based on per-pixel displacement mapping (Oliveira, Bishop & McAllister, 2000; Yerec & Jagersand, 2004; Baboud & Décoret, 2006a; Baboud & Décoret, 2006b; Policarpo & Oliveira, 2006; Ritsche, 2006; Toledo, Lévy & Levy, 2008; Toledo, Wang & Lévy, 2008; Halli et al., 2010; Ragragui et al., 2017; Ragragui et al., 2018a; Ragragui, et al., 2018b; Ragragui et al., 2020). Despite the diversity of the objects that can be created using these techniques, the silhouette problem persists. Once this problem is resolved and seen that modern graphics cards integrate and implement ray tracing algorithms, these techniques represent a better alternative to displacement mapping for creating 3D objects.

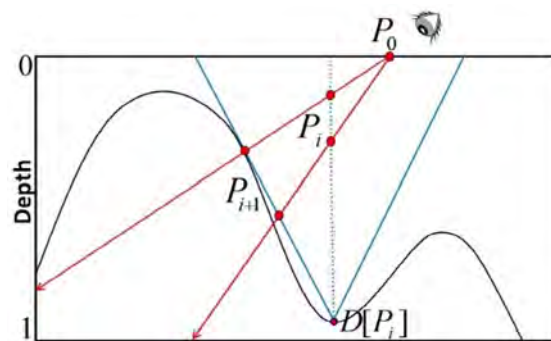
Cone tracing technique

In the pre-processing stage, the cone tracing technique calculates the empty space around each pixel of the depth map as a top-opened cone and stores its radius in a displacement map (Halli et al., 2008) (i.g. alpha channel). Then we use this space during the search for the intersection to converge quickly. This technique has been presented in two versions, the conservative technique and the relaxed one. In the first one, the cone is defined so that the cone tracing does not pierce the relief (Figure 13), and in the second one (Figure 14), the cone is defined so that the cone tracing cannot pierce the relief more than once, and then, the intersection point is refined using a binary search.

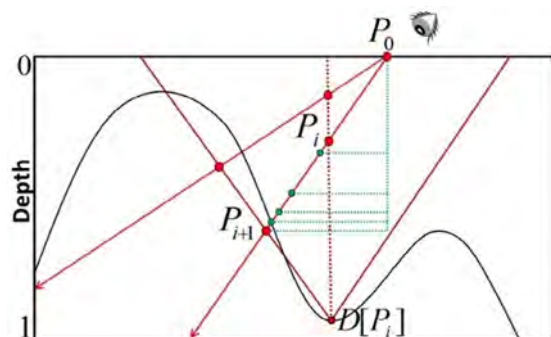
In both cases, the next t_{i+1} parameter is given by:

$$t_{i+1} = t_i + \frac{\text{cone_radius}(D[P_i] - P_{i_z})}{D[P_i]v_{xy} + \text{cone_radius}} \quad (4)$$

The next point P_{i+1} is computed with the formula (3), where $D[P_i]$ is the depth at point P_i in this case, it represents the height of the cone.

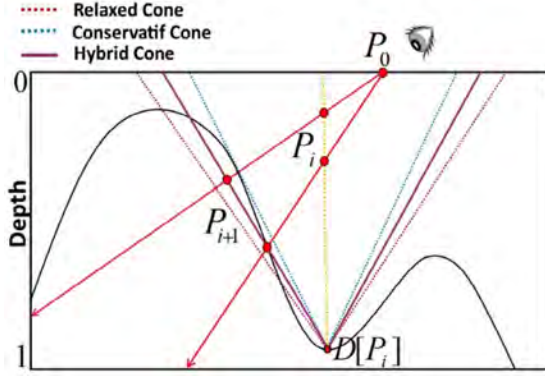


» **Figure 13:** Ray tracing in the cones map (cross-section). In each iteration, the following position P_{i+1} of the viewing ray is calculated according to the current position P_i and the value of the t_{i+1} parameter



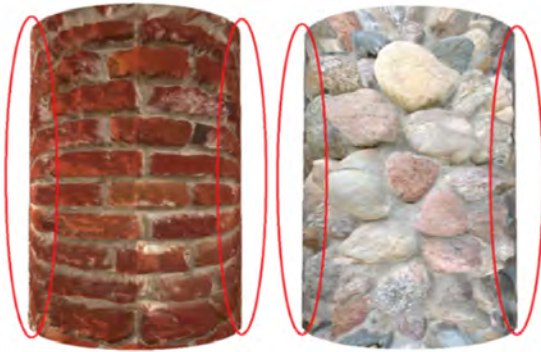
» **Figure 14:** The binary search phase with the relaxed cone tracing. It is made between the last position P_{i+1} and the starting position P_0 of the viewing ray

The third version of the cone has been proposed in (Ouazzani Chahdi et al., 2017), which is about the hybrid cone (Figure 15). The principle of this contribution is to use a cone that is located between the conservative cone and the relaxed one so that the cone tracing pierces the relief only once and without the need for binary research. This contribution further improves rendering quality and increases rendering speed.



» **Figure 15:** The hybrid cone is located between the conservative and the relaxed one (Ouazzani Chahdi et al., 2017)

Cone tracing (in its three versions) remains effective for real-time rendering on flat surfaces, but when it is about of the curved surfaces, the silhouette is not visible at the edges of the rendered objects (Figure 16).



» **Figure 16:** Rendering of a cylinder with the original cone-tracing techniques. The silhouette is not visible at the edges of the 3D objects. That is to say, the reliefs elevations coincide with the surface of the cylinder

To solve this problem, we propose to use the quadratic approximation approach to exploit its parameters in the cone-tracing phase to determine the silhouette fragment. The proposed contribution is based on the originals cone tracing techniques (Halli et al., 2008) and the quadratic approximation approach (Jean, 2002; Oliveira & Policarpo, 2005).

Quadratic approximation

The quadratic approximation was used with the relief mapping technique in (Oliveira & Policarpo, 2005), it consists of calculating an approximate quadratic surface for each vertex of the 3D mesh during a preprocessing stage, and in the rendering stage, this surface is used to adapt the ray-tracing process so that it takes into consideration the form of the mesh geometry.

The approximate quadratic surface is represented by two parameters a and b so that:

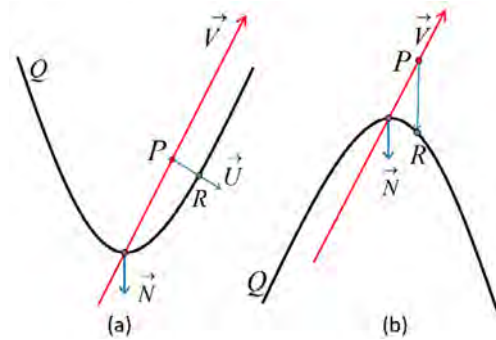
$$z = ax^2 + by^2 \quad (5)$$

where (x, y, z) are the coordinates of the processed vertex.

These parameters are calculated by using the quadrics (Jean, 2002): let E be the set of the triangles sharing a vertex $m_k(x_k, y_k, z_k)$, and let $M = \{m_1, m_2, \dots, m_n\}$ the set of the vertices in E . All the vertices in M are expressed in the tangent space associated with m_k . Given $M' = \{m'_1, m'_2, \dots, m'_n\}$, where $m'_i = (x'_i, y'_i, z'_i) = (x_i - x_k, y_i - y_k, z_i - z_k)$, the coefficients a and b are obtained by solving the following system $Ax = b$:

$$\begin{pmatrix} x_1'^2 & y_1'^2 \\ x_2'^2 & y_2'^2 \\ \vdots & \vdots \\ x_n'^2 & y_n'^2 \end{pmatrix} \times \begin{pmatrix} a \\ b \end{pmatrix} = \begin{pmatrix} z_1' \\ z_2' \\ \vdots \\ z_n' \end{pmatrix} \quad (6)$$

During the rendering stage, coefficients a and b will be interpolated for each pixel and then used to calculate the distance between the viewing ray and the quadratic surface. We have two cases as shown in Figure 17.



» **Figure 17:** Cross-section of two quadratic surfaces. On the left surface (a), the viewing ray is inside the quadric, and on the right surface (b), the viewing ray is outside. In both cases, the distance between the viewing ray and the quadric Q is given by the PR segment

V is the viewing ray and lets R be a point belonging to the quadric Q , U is the unit vector perpendicular to V at the point P .

In the first case (V inside the quadric, see Figure 17a); R is obtained by translating P by d units along the vector U:

$$R = P + Ud \quad (7)$$

The distance between the point P and the quadric is simply d , which can be obtained by substituting the coordinates of R in the equation of the quadric:

$$\begin{aligned} aR_x^2 + bR_y^2 - R_z &= 0 \\ a(P_x + dU_x)^2 + b(P_y + dU_y)^2 - (P_z + dU_z) &= 0 \end{aligned} \quad (8)$$

The solution of this equation gives:

$$d = \frac{-B + \sqrt{\Delta}}{2A} = \frac{-B + \sqrt{B^2 - 4AC}}{2A} \quad (9)$$

With $\Delta > 0$ and $\begin{cases} A = aU_x^2 + bU_y^2 \\ B = 2aP_xU_x + 2bP_yU_y - U_z \\ C = aP_x^2 + bP_y^2 - P_z \end{cases}$

In the second case (V outside the quadric, see Figure 17b), where $\Delta < 0$, the viewing ray is outside the quadric, in this case, the distance d is:

$$d = P_z - (aP_x^2 + bP_y^2) = P_z - q \quad (10)$$

We denote by q the quadric ($aP_x^2 + bP_y^2$) associated with the parameters a and b .

The texture space is planar, and in the rendering stage, the approximate surface calculated at each vertex of the 3D mesh during the preprocessing stage is used so that this space can be adapted to the 3D object geometry. In reality, the texture space remains always planar, and during the search for the intersection, the viewing ray is rectified to correct the position of the point P_{i+1} using the characteristics of the approximate surface. We denote by v and u respectively the vector V and U expressed in the texture space.

In the first case (Figure 17a), the next point P_{i+1} is corrected by:

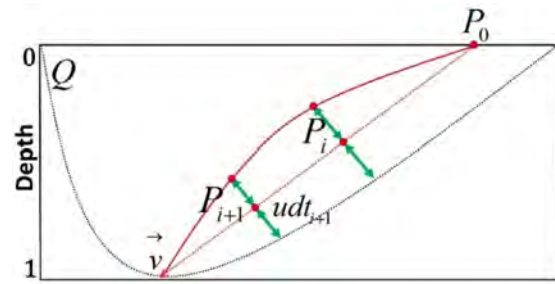
$$P_{i+1} = (v + ud)t_{i+1} = (v + w)t_{i+1} \quad (11)$$

Moreover, in the second case (Figure 17b), the next point P_{i+1} is corrected by:

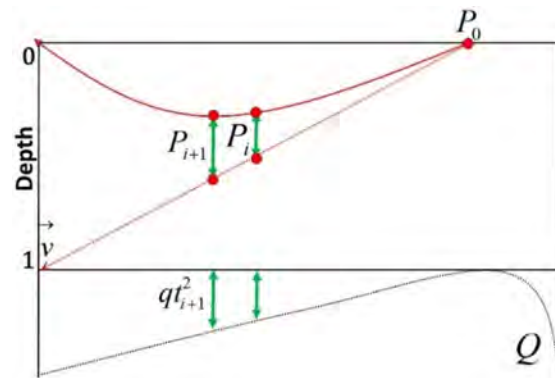
$$P_{i+1} = (v_x t_{i+1}, v_y t_{i+1}, v_z t_{i+1} - q t^2) \quad (12)$$

Since the depth of v is normalized (v/v_z), so, in the first case, the distance d must be divided by v_z , and in the second case, the quadric q must be divided by v_z^2 , and this before normalizing the depth of v .

Figure 18 and Figure 19 show the general appearance of the viewing ray during the search for the intersection.

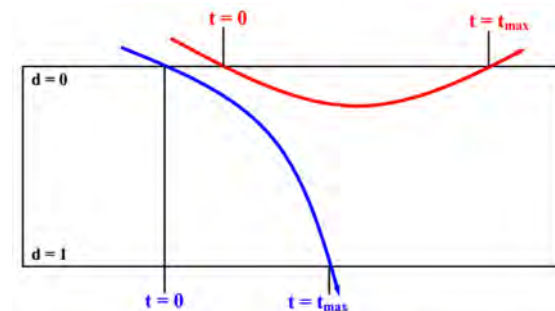


» **Figure 18:** The viewing ray is inside the quadric. At each iteration, we approach the quadratic surface



» **Figure 19:** The viewing ray is outside the quadric. At each iteration, we move away from the quadratic surface

During the linear search, the relief mapping technique (Policarpo, Oliveira & Comba, 2005) chooses the t parameter in the interval $[0, 1]$. This search is optimized in (Oliveira & Policarpo, 2005) by choosing this one in the interval $[0, t_{max}]$, with t_{max} is the smallest $t > 0$ such that the distance from the viewing ray to the quadric is equal to 0 or 1 (Figure 20).



» **Figure 20:** A ray that hits depth 1 ($d = 1$) in the texture space has reached the bottom of the depth field characterizing an intersection (the blue ray). On the other hand, a ray that returns to the depth 0 ($d = 0$) can be safely discarded as belonging to the silhouette (the red ray)

To find the most accurate value, t_{max} must be calculated by substituting (P_x, P_y, P_z) by $(V_x t, V_y t, V_z t)$ and setting $d=0$ and $d=1$ respectively in both equations (8) and (10), then solve for t . Algorithms 1 and 2 implement this optimization in both cases.

Algorithm 1: tMax1

Input: $V, U, (a, b)$ | Output: t_{max}

Begin

$A \leftarrow a \cdot V_x \cdot V_x + a \cdot V_y \cdot V_y$

$B \leftarrow 2 \cdot a \cdot V_x \cdot U_x + 2 \cdot b \cdot V_y \cdot U_y - V_z$

$C \leftarrow a \cdot U_x \cdot U_x + b \cdot U_y \cdot U_y - U_z$

$D \leftarrow B \cdot B - 4 \cdot A \cdot C$

If $D > 0$ Then

$t_{max} \leftarrow (B - \text{Sqrt}(D)) / (-2 \cdot A)$

EndIf

$D \leftarrow V_z / A$

If $D > 0$ Then

$t_{max} \leftarrow \text{Min}(t_{max}, D)$

EndIf

$t_{max} \leftarrow \text{Abs}(t_{max})$

End

Algorithm 2: tMax2

Input: V, q | Output: t_{max}

Begin

$D \leftarrow V_z \cdot V_z - 4 \cdot q$

If $D > 0$ Then

$t_{max} \leftarrow (-V_z + \text{Sqrt}(D)) / (-2 \cdot q)$

EndIf

$D \leftarrow V_z / q$

If $D > 0$ Then

$t_{max} \leftarrow \text{Min}(t_{max}, D)$

EndIf

$t_{max} \leftarrow \text{Abs}(t_{max})$

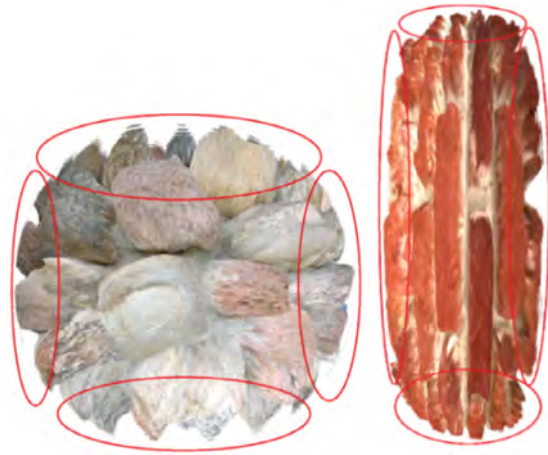
End

During the search for the intersection, the parameter t_{i+1} is calculated by:

$$t_{i+1} = t_i + t_{max}/steps \quad (13)$$

At the end of the linear search, we check whether the value of the t parameter is greater than t_{max} , if this is the case, the pixel must be discarded, else the intersection point is refined with a binary search.

The combination of relief mapping with quadratic approximation produces satisfactory results, but when the depth scale is large enough or when the viewing ray shaves the surface, defects become visible as shown in Figure 21.



» **Figure 21:** The defects are visible in the parts where the viewing ray shaves the surface

Cone tracing with correct silhouette

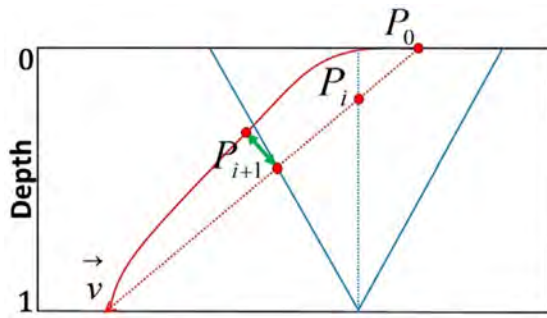
As mentioned above, the original cone tracing technique produces satisfactory results when it is about flat surfaces (Halli et al., 2008), but for the curved surfaces, the silhouette didn't render correctly at the edges of the 3D object. To correct the silhouette problem, we will use the parameters of the quadratic surface to adapt the cone tracing process so that it takes into account the characteristics of the 3D surface. For this, we opted two solutions. The first one uses a rectification of the viewing ray after each new displacement along the viewing ray and the second one uses a rectification of the cone before each new displacement along the viewing ray. Algorithm 7 of this section presents an implementation of the new cone-tracing techniques in both cases.

Rectification of the viewing ray

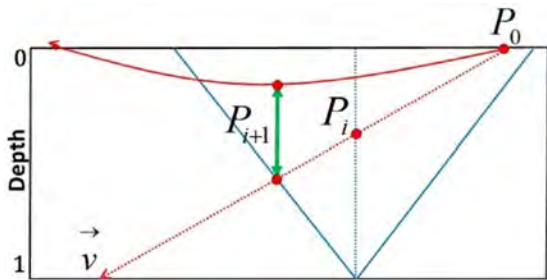
This rectification consists of adapting the displacements along the viewing ray so that they take into account the forms of the quadratic surfaces presented in Figure 17. In both cases, the t_{i+1} parameter is calculated with the formula (4).

In the first case (Figure 17a), the point P_{i+1} approaches the quadratic surface, and if there is an intersection, we converge quickly to the depth value 1 (Figure 22). This rectification is realized with the formula (11).

In the second case (Figure 17b), the point P_{i+1} moves away from the quadratic surface, that is to say, that we move away from the depth value 1. And if there is no intersection, we converge quickly to the depth value 0 (Figure 23). The rectification is realized with the formula (12).



» **Figure 22:** The viewing ray is inside the quadric, at each iteration, the point P_{i+1} is rectified according to the value du_{i+1}



» **Figure 23:** The viewing ray is outside the quadric. At each iteration, the depth of the point P_{i+1} is rectified according to the value $-qt_{i+1}^2$

Algorithms 3 and 4 implement this rectification. Figure 24 shows a comparison between a sphere rendered without and with silhouette correction and Figure 25 shows a torus rendered with this approach and by highlighting the polygonal meshes.

Algorithm 3: CurvedTransformeRay1

```

Input: p0, v, w, C, tmax | Output: t
Begin
  t ← 0
  For i=1 To STEPS And t <= tmax Do
    p ← p0 + (v + w)*t
    radius ← C[p.x,p.y].blue
    depth ← C[p.x,p.y].alpha
    t ← t + (radius * Max(depth - p.z,
      0) / (radius +
      depth*Length(v.xy)))
  EndFor
End

```

Algorithm 4: CurvedTransformeRay2

```

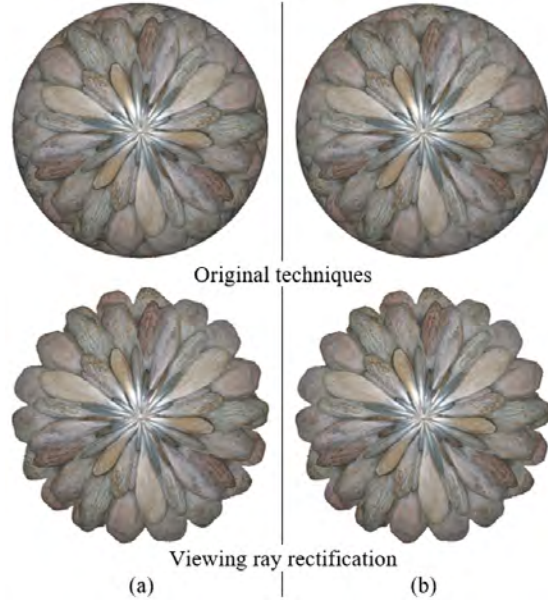
Input: p0, v, q, C, tmax | Output: t
Begin
  t ← 0
  For i=1 To STEPS And t <= tmax Do

```

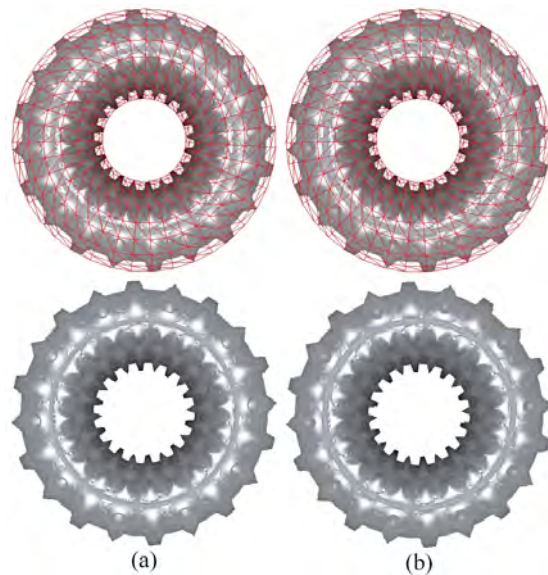
```

p ← p0 + v*t
p.z ← p.z - t*t*q
radius ← C[p.x,p.y].blue
depth ← C[p.x,p.y].alpha
t ← t + (radius * Max(depth - p.z,
  0) / (radius + depth*Length(v.xy)))
EndFor
End

```



» **Figure 24:** Comparison of a sphere rendered by the original cone tracing techniques and by using the viewing ray rectification. (a) Conservative technique. (b) Relaxed technique



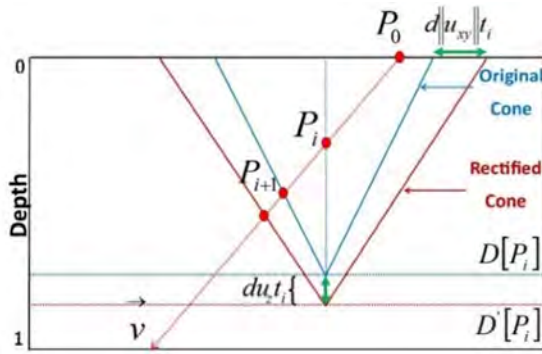
» **Figure 25:** Rendering of a torus by using the viewing ray rectification approach and by highlighting the polygonal meshes. (a) Conservative technique. (b) Relaxed technique

The change of the camera position does not influence the rectification process or the rendering quality since the rectification is realized in real-time and with each movement of the camera, we will have a new image rendered with a new rectification.

Rectification of the cone

The approximate surface has two forms, concave and convex (Figure 17). Instead of adapting the texture space to these forms, the cone is rectified so that it is influenced by the characteristics of the approximate surface. This rectification is realized before the cone tracing on its parameters, namely the radius and the height (cone depth).

In the first case (Figure 17a), the cone must be enlarged so that it approaches the quadratic surface. The rectification consists of increasing the values of the cones parameters stored in the displacement map by using the distance d and the vector u (Figure 26).



» **Figure 26:** The quadratic surface approaches the point P_{i+1} , so we move forward rapidly towards the intersection point

The depths increase, which implies the increase of the cones' depths (heights). The new cone depth is:

$$D'[P] = D[P] + dt_z t \quad (14)$$

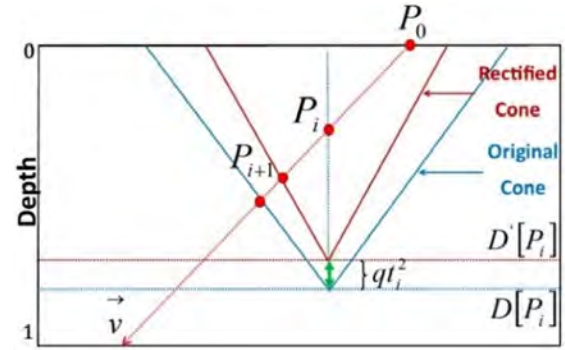
For the cone radius, we have:

$$cone_radius' = cone_radius + d||u_{xy}||t \quad (15)$$

Figure 26 shows that the displacement along the viewing ray with the rectified cone is faster than the base one because the displacement step increases. At each iteration, the cone rectification advances the P_{i+1} point along the viewing ray, and we converge more quickly in the case of an intersection.

In the second case (Figure 17b); the cone decreases so that it moves away from the quadratic surface. Indeed, the cone rectification consists of reducing

the values of its parameters stored in the displacement map by using the quadric q (Figure 27).



» **Figure 27:** The quadratic surface moves away from the point P_{i+1} , where the pixel belongs to the silhouette, we will don't have an intersection, so the pixel will be discarded

The depths decrease, which implies the decrease of cones depths (heights), so the new cone depth is:

$$D'[P] = D[P] - t^2 q \quad (16)$$

we have:

$$cone_ratio = \frac{cone_radius}{D[P]} = \frac{cone_radius'}{D'[P]}$$

therefore, the new cone radius is given by:

$$cone_radius' = \frac{cone_radius}{D[P]} \times D'[P] \quad (17)$$

Figure 27 shows that the displacement along the viewing ray with the rectified cone is slower than the base one because the displacement step decreases. At each iteration, the cone rectification moves back the point P_{i+1} along the viewing ray, and we diverge in the case where there is no intersection.

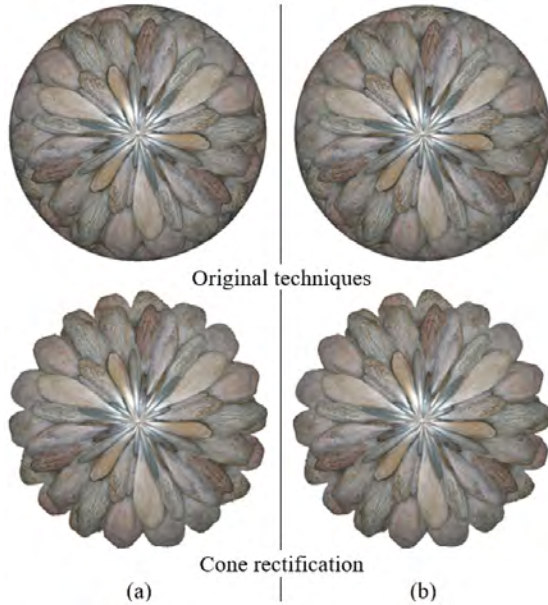
In both cases, the t_{i+1} parameter is calculated by:

$$t_{i+1} = t_i + \frac{cone_radius'(D'[P_i] - P_z)}{D'[P_i]||v_{xy}'|| + cone_radius'} \quad (18)$$

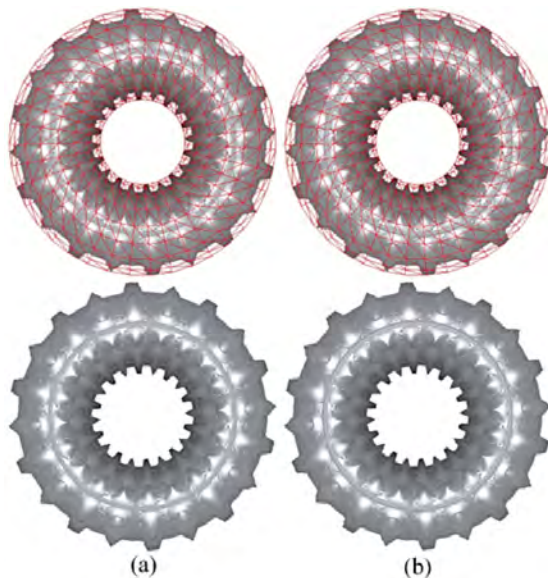
The next point P_{i+1} is computed with the formula (3). Algorithms 5 and 6 implement this rectification. Figure 28 shows a comparison between a sphere rendered without and with silhouette correction and Figure 29 shows a torus rendered with this approach and by highlighting the polygonal meshes.

Cone rectification does not depend on the depth map; it depends only on the quadratic parameters associated with the 3D surface. Also, the cones map is not attached to the base geometry onto which it is

mapped, because the rectification process is realized in real-time. This makes it possible to use the same rectification process and the same texture in real-time on different 3D objects, it means that the rectification process and the cones map are independent of the surface on which they will be used (Figure 30).



» **Figure 28:** Comparison of a sphere rendered by the original cone tracing techniques and by using the cone rectification. (a) Conservative technique. (b) Relaxed technique



» **Figure 29:** Rendering of a torus by using the cone rectification approach and by highlighting the polygonal meshes. (a) Conservative technique. (b) Relaxed technique

Algorithm 5: CurvedTransformeCone1

Input: p_0, v, w, C, t_{max} | Output: t

Begin

$p \leftarrow p_0$

$t \leftarrow 0$

For $i=1$ To STEPS And $t \leq t_{max}$ Do

$radius1 \leftarrow C[p.x, p.y].blue$

$depth1 \leftarrow C[p.x, p.y].alpha$

$radius2 \leftarrow radius1 + t * Length(w.xy)$

$depth2 \leftarrow depth1 + t * w.z$

$t \leftarrow t + (radius2 * Max(depth2 - p.z,$

$0) / (radius2 +$

$depth2 * Length(v.xy))$

$p \leftarrow p_0 + v * t$

EndFor

End

Algorithm 6: CurvedTransformeCone2

Input: p_0, v, q, C, t_{max} | Output: t

begin

$p \leftarrow p_0, t \leftarrow 0$

For $i=1$ To STEPS And $t \leq t_{max}$ Do

$radius1 \leftarrow C[p.x, p.y].blue$

$depth1 \leftarrow C[p.x, p.y].alpha$

$depth2 \leftarrow depth1 - t * t * q$

$radius2 \leftarrow (radius1 / depth1) * depth2$

$t \leftarrow t + (radius2 * Max(depth2 -$

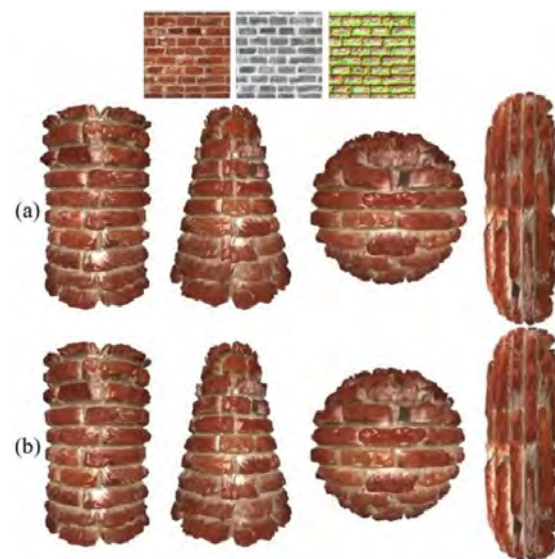
$p.z, 0) / (radius2 +$

$depth2 * Length(v.xy))$

$p \leftarrow p_0 + v * t$

EndFor

End



» **Figure 30:** Rendering of several 3D objects in real-time with the same cone rectification process and with the same texture. (a) Conservative technique. (b) Relaxed technique

The curved cone tracing algorithm

In this subsection, we present the implementation of the cone tracing algorithm with silhouette correction in the two approaches.

In the rendering stage, the search for the intersection is performed in the texture space, but the calculations related to the quadratic approximation are performed in the tangent space where t is equal to 1 so that the quadratic distance is computed as the viewing ray progresses.

Algorithm 7: CurvedConeTracing

Input: (s, t) , T , V , U , (S_x, S_y, S_z) , C , R , (a, b)

Output: p

Begin

```
p0 ← (T.x*s, T.y*t, 0)
v ← Normalize(V/(Sx, Sy, Sz))
v.z ← -v.z
vz ← v.z
v ← v/v.z
vR ← v*(Length(v.xy)/
(Sqrt(v.x*v.x+R*R*v.y*v.y)))
A ← a*U.x*U.x + b*U.y*U.y
B ← 2*a*V.x*U.x + 2*b*V.y*U.y - U.z
C ← a*V.x*V.x + b*V.y*V.y - V.z
D ← B*B - 4*A*C
If D > 0 Then
    tmax ← tMax1(V, U, a, b)
    u ← Normalize(U/(Sx, Sy, Sz))
    w ← ((B - Sqrt(D))/-2*A)*u/vz
    t←CurvedTransformer-
ay1(p0, vR, w, C, tmax)
    //t←CurvedTransforme-
Cone1(p0, vR, w, C, tmax)
Else
    q ← a*V.x*V.x + b*V.y*V.y
    q ← Sign(q) * Max(Abs(q), 0.001)
    tmax ← tMax2(V, q)
    q ← (q/Sz)/(vz*vz)
    t←CurvedTransformer-
ay2(p0, vR, q, C, tmax)
    //t←CurvedTransforme-
Cone2(p0, vR, q, C, tmax)
EndIf
If t > tmax Then
    Discard
Else
    p ← p0 + v*t
```

```
EndIf
// Binary search (only in the
case of relaxed cones)
v ← (v*p.z)/2 // initial step size
p ← p0 + v // starting point
For i=1 To STEPS Do
    depth ← C[p.x, p.y].alpha
    v ← v/2
    If p.z < depth then
        p ← p + v
    Else
        p ← p - v
    EndIf
EndFor
End
```

Results and discussion

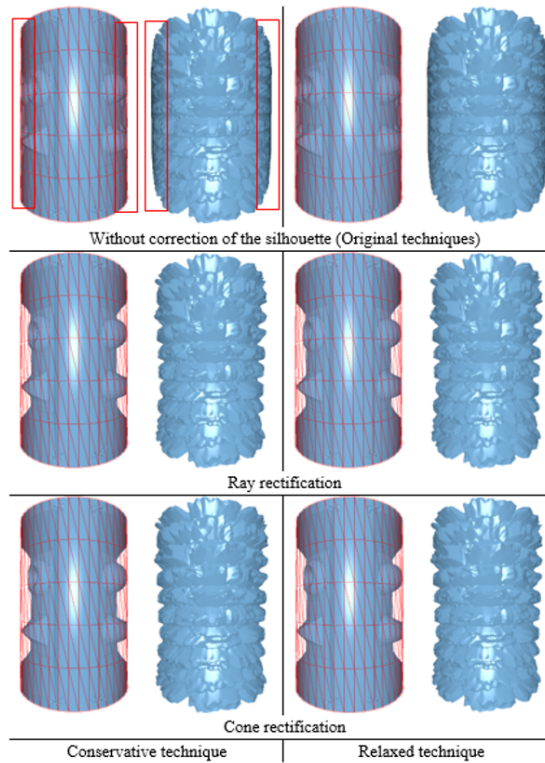
We have implemented the pre-processing part of the techniques discussed in this paper in C++. For rendering, we have exploited the programmable units of the GPU, namely Vertex Shader and Fragment Shader using OpenGL/GLSL. The figures are obtained using a Core-i7-4510U-2GH-4CPUs architecture with 8GB of RAM and GeForce-GT-840M with 4GB of memory.

In this paper, we have implemented different techniques of per-pixel displacement mapping, namely, conservative cone tracing, relaxed cone tracing, and relief mapping, to make a comparison with the proposed improvements. In our implementation, we have attached the magnification/minification method for the two camera positions (near and far) to the displacement map (cones map) and the color map using the same resolution (256×256, 512×512, 1024×1024, and 2048×2048).

The images of the figures are rendered with 25 linear steps and 5 binary steps. For the texture resolution, we have used 512×512. Figure 24 and Figure 28 show comparisons of a sphere rendered without and with silhouette correction using the two rectifications, namely the viewing ray rectification and the cone rectification. The images of Figure 25 are rendered with the viewing ray rectification approach and those of Figure 29 are rendered with the cone rectification approach. Figure 30 shows several 3D objects rendered with cone rectification using the same texture.

Figure 31 shows a comparison between the original cone tracing techniques and the addition of the viewing ray rectification and cone rectification. The figure shows clearly that the original techniques suffer from the silhouette problem. That is to say, during the search for the intersection point, the technique considers

that each processed 3D surface is flat, and does not take into consideration its curvature. Then, the reliefs at the edges of the 3D object are confused with its surface, which produces an incorrect rendering. The two proposed rectifications solved this problem.

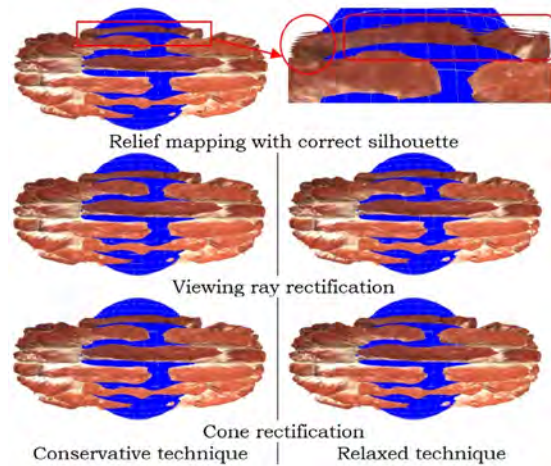


» **Figure 31:** Comparison of a cylinder rendered by the cone tracing techniques. In the case of the original techniques (Halli et al., 2008), the reliefs near the silhouette are not rendered correctly, that is to say, the reliefs are confused with the surface of the cylinder. On the other hand, with the help of the viewing ray rectification and the cone rectification, the silhouette is visible at the edges of the 3D objects

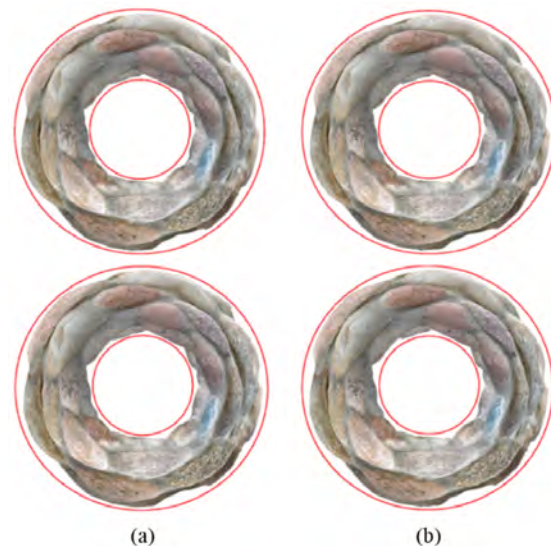
Concerning the comparison between relief mapping with correct silhouette (Oliveira & Policarpo, 2005) and cone tracing combined with the proposed rectifications, we have found that the major problem is related to the grazing angles. The combination of cone tracing with the quadratic approximation solves this problem.

Figure 32 shows the disappearance of the artifacts at the grazing angles in the images rendered by our rectifications. The same problem persists in the case of the interpenetration of 3D objects.

The images qualities of Figure 24, Figure 25, Figure 28, and Figure 29 are close, but in some cases, where the viewing ray or the depth scale is changed, small differences become visible as shown in Figure 33 and Figure 34. The figures show a comparison of a torus rendered with the approaches proposed in this paper.



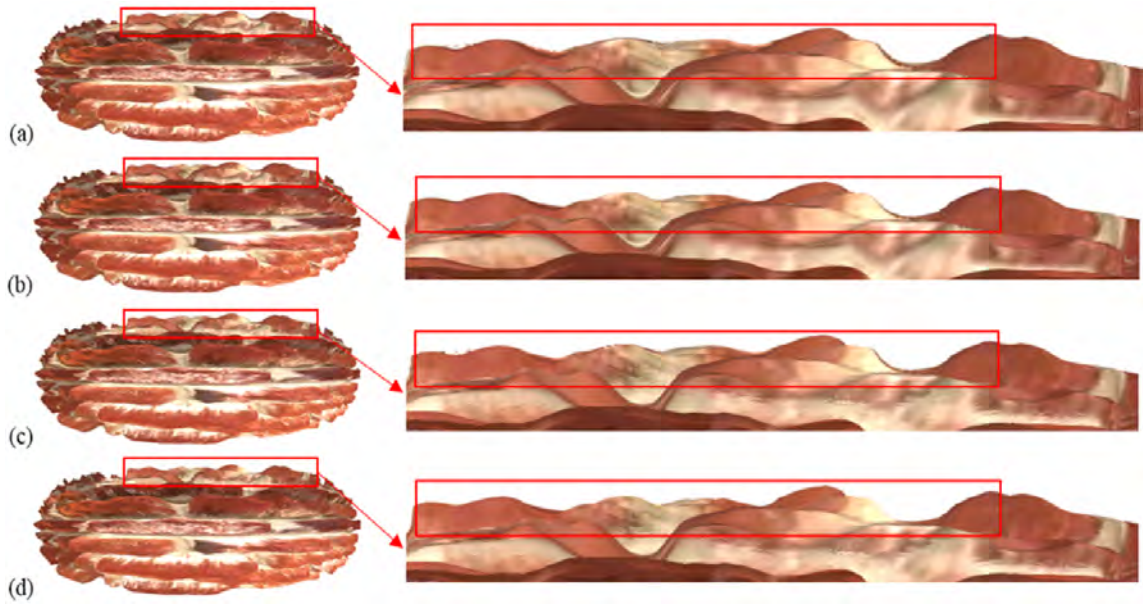
» **Figure 32:** The interpenetration of two 3D objects, a sphere, and a torus. We observe that the rendering done by the relief mapping with the correct silhouette present always the same problem related to the grazing angles, this problem is solved by our proposed rectifications as shown in the figure



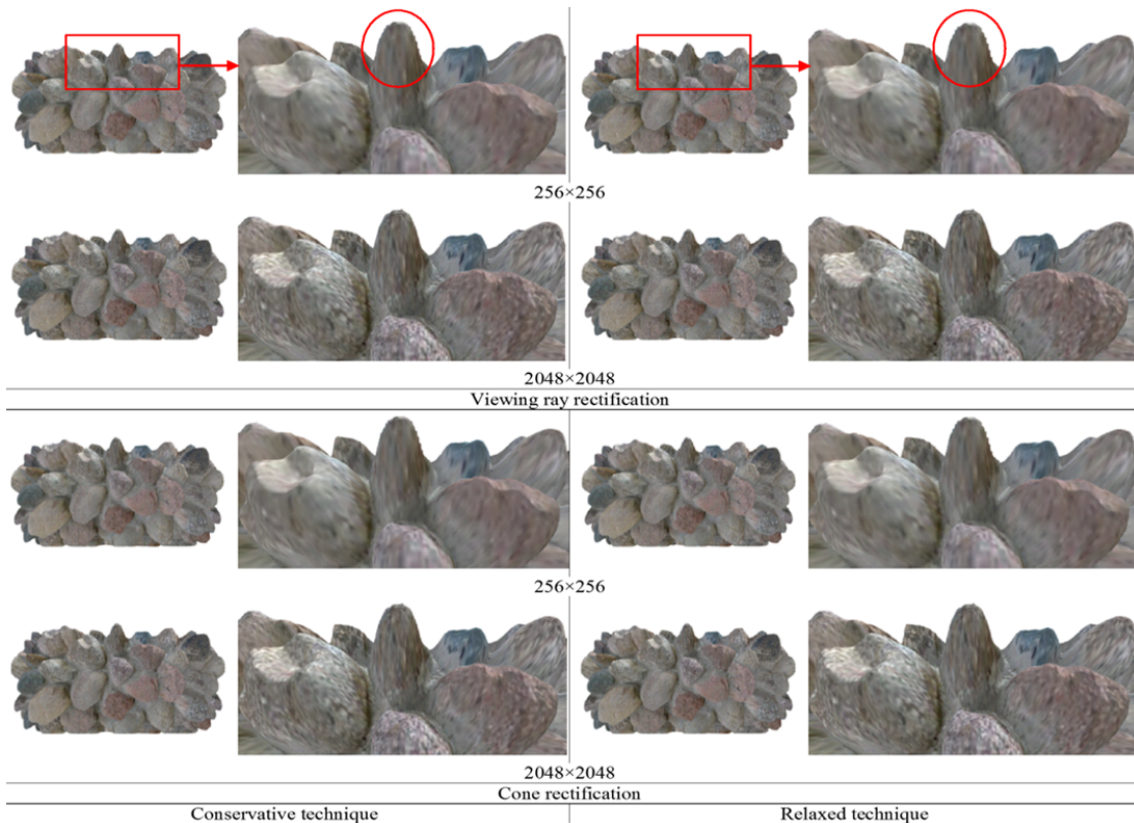
» **Figure 33:** Rendering of a torus by the approaches proposed in this paper with a depth scale equal to 0.4. (a) Conservative technique. (b) Relaxed technique. The approach by rectification of the viewing ray at the top and the approach by rectification of the cone at the bottom. Rendering differences are visible on the edges

The qualities of the images rendered by the two approaches (i.e. viewing-ray rectification and cone rectification) seem identical. Minimal differences can be observed when we use a minimal number of steps (i.e. linear steps ≤ 25 , binary steps ≤ 5), but when the number of steps is greater, the qualities of the rendering images become closer.

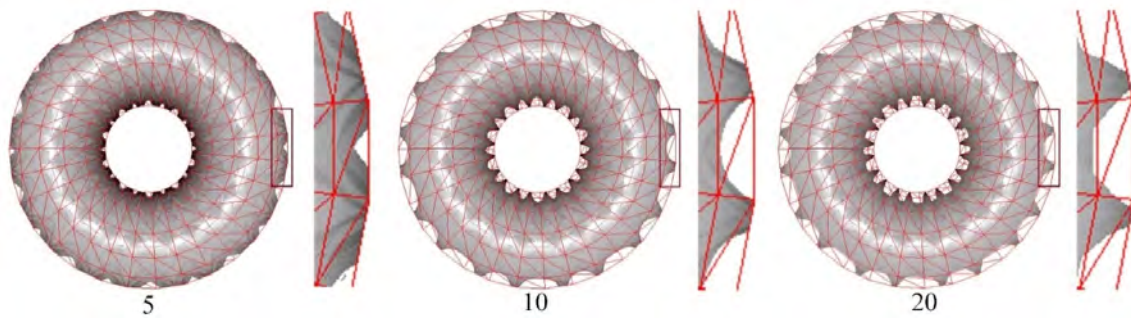
Figure 35 shows a cylinder rendered with the different approaches discussed in this paper using two resolutions



» **Figure 34:** Rendering of a torus by the four approaches of cone tracing with a depth scale equal to 0.6. (a) Conservative cone with viewing ray rectification. (b) Conservative cone with cone rectification. (c) Relaxed cone with viewing ray rectification. (d) Relaxed cone with cone rectification. We observe minimal differences at the edges between the different rendered images.



» **Figure 35:** Rendering of a cylinder with a texture resolution of 256x256 and 2048x2048 (depth map and color map have the same resolution). We observe that the resolution of the textures plays a very important role in the quality of the rendered images. The images rendered with a low resolution of texture present some aliasings which are corrected by using a texture with a high resolution



» **Figure 36:** Rendering of a torus by the cone tracing with correct silhouette using a different number of linear steps (5, 10, and 20). We observe that the appearance degree of the silhouette depends on the number of the steps. The image rendered with 20 steps presents the best correct silhouettes.

of the texture: 256×256 and 2048×2048 and two camera positions (far and near). The figure shows that the texture resolution plays a very important role in the quality of rendered images; a high resolution of texture allows having better quality and thus avoiding the aliasing problems.

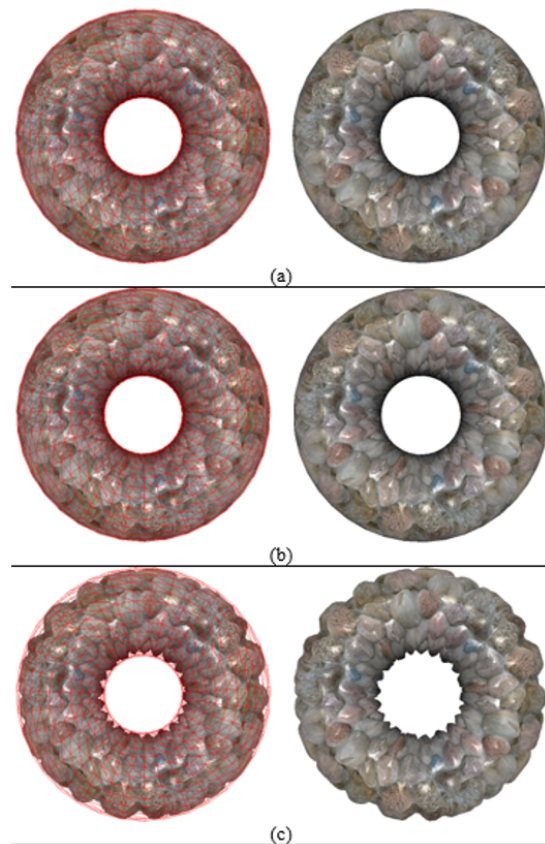
Figure 36 shows a torus rendered with the cone tracing with the correct silhouette using different steps number and by highlighting the polygonal meshes. We observe that the number of steps plays a very important role in the appearance of the microreliefs and the correct silhouette.

The proposal of the hybrid cone in (Ouazzani Chahdi et al., 2017) and the dynamic relief mapping in (Ouazzani Chahdi et al., 2018) made it possible to improve the rendering quality for flat surfaces. But when it is about curved surfaces, the silhouette is not treated correctly. Indeed, figure 37 shows the difference between these last two techniques and the proposed contributions.

Figure 38 shows the difference between a sphere and a cylinder which are rendered by revolution-bump mapping (Figure 38a), extrusion-bump mapping (Figure 38b), and cone tracing with a correct silhouette (Figure 38c).

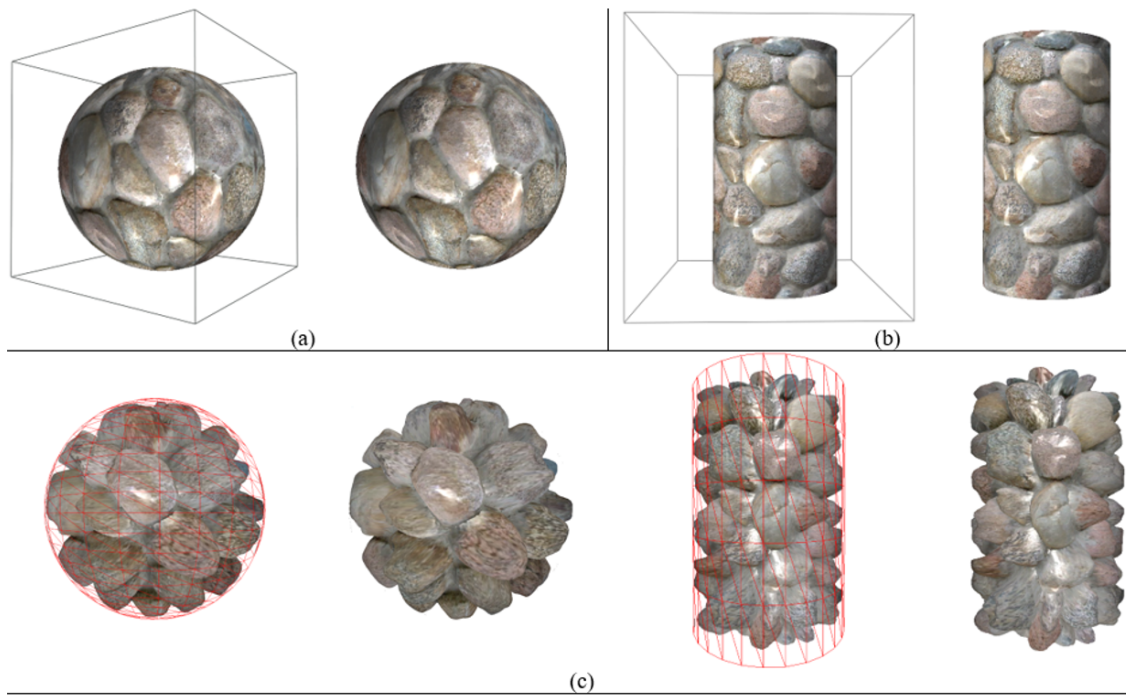
Revolution and extrusion are based on a shape box and the combination of the bump mapping allows adding a microrelief effect and does not create real displacements of the reliefs. Using a new ray-tracing algorithm, the revolution creates a 3D object around an axis of revolution based on a 2D form, and the extrusion extrudes this form upwards.

The objects created by these two techniques are not represented by any parametric surface which allows giving information on its curvature for each pixel, moreover, at the extrusion or revolution phase, the curvature of the extruded or the revolved form is not taken into account, and in this case, the treatment of the silhouette will be limited.



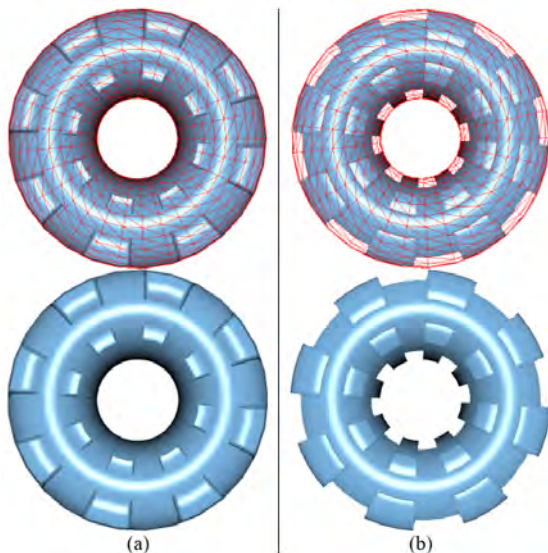
» **Figure 37:** Comparison of a torus rendered by the three techniques of cone tracing. (a) Hybrid cone (Ouazzani Chahdi et al., 2017). (b) Dynamic relief mapping (Ouazzani Chahdi et al., 2018). (c) Cone tracing with the correct silhouette. The problem concerning the silhouette is located at the edges of the torus rendered by the two techniques (a) and (b). This problem is solved with the help of the two proposed rectifications

In the case of per-pixel extrusion mapping, a new ray-tracing algorithm has been introduced in (Halli et al., 2009). Its advantage is the acceleration of the search for the intersection point, but the disadvantage is that it only deals with extrusion and does not take into account the silhouette treatment (Figure



» **Figure 38:** *Rendering of a cylinder and a sphere. (a) Revolution with bump mapping (Ragragui et al., 2018a; Ragragui, et al., 2018b). (b) Extrusion with bump mapping (Ragragui et al., 2017; Ragragui et al., 2020). (c) Cone tracing with the correct silhouette. Revolved or extruded objects are rendered using a shape box and the bump mapping allows just a microrelief effect (simulation of small displacements). The objects created by cone tracing are rendered using a polygonal mesh and the reliefs are displaced without modifying the mesh geometry, moreover, the proposed cone rectifications make the silhouette visible*

39a). The advantage of the algorithms proposed in this paper is that they are suitable for relief or extrusion and solve the silhouette problem (Figure 39b).



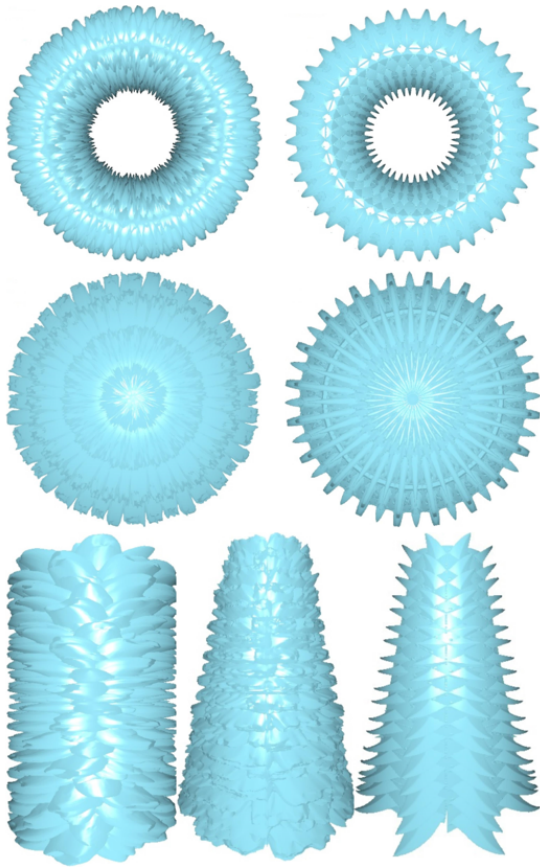
» **Figure 39:** *Comparison of a torus rendered by two techniques. (a) Per-pixel extrusion mapping (Halli et al., 2009). (b) Cone tracing with the correct silhouette. Both techniques use a basic polygonal mesh but the silhouette problem is corrected only in the torus rendered by our approach*

Figure 40 shows some extra examples with simple high-frequency displacements and no color texture. The 3D objects are rendered by the cone tracing technique with the correct silhouette and by using different depth maps and different depth values.

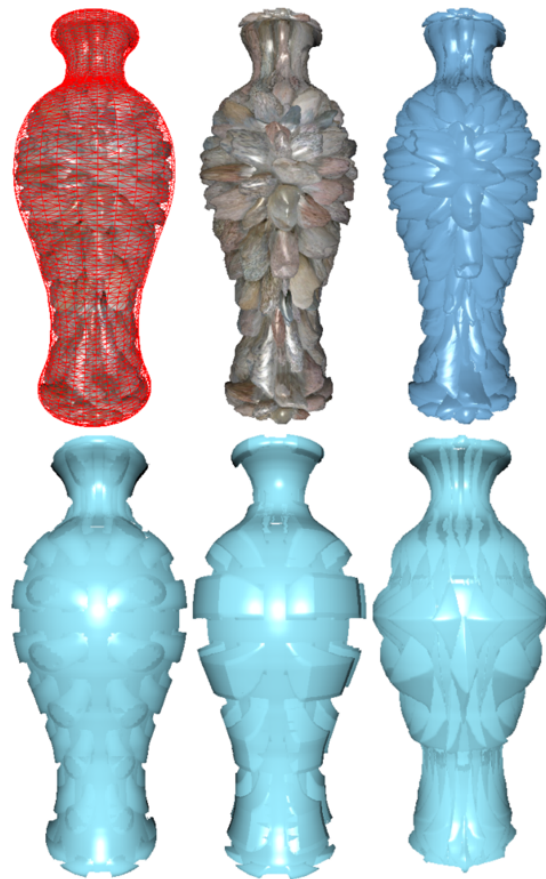
Figure 41 shows a vase rendered by the cone-tracing technique with the correct silhouette and by highlighting the basic polygonal mesh. The 3D object is rendered with different depth maps and different depth values. In the different images of the figure, we notice that the silhouette is corrected whatever the depth map used.

Generally, the combination of the quadratic approximation with the cone-tracing technique produces satisfactory results, but in some cases, this combination produces holes as shown in Figure 42. This problem is due to the use of the quadratic approximation for the local representation of the surface at each vertex. Because sometimes, the viewing ray pierces the relief in the object space and leaves it in the texture space. This problem has been also mentioned in (Jeschke, Mantler & Wimmer, 2007; Chen & Chang, 2008; Na & Jung, 2008).

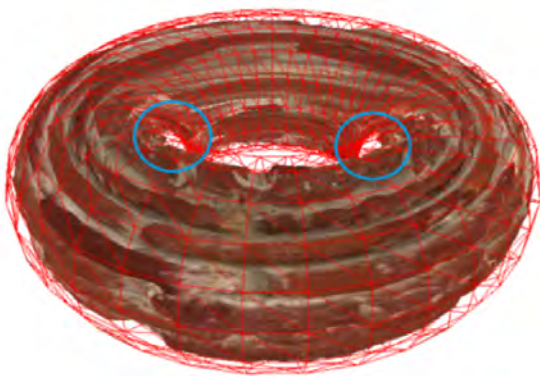
To surmount this problem, the quadratic approximation can be replaced by a local space at each vertex of the 3D mesh (Chen & Chang, 2008; Na & Jung, 2008).



» **Figure 40:** Rendering of different 3D objects by the cone tracing techniques with correct silhouette and by using simple high-frequency displacements and no color texture



» **Figure 41:** Rendering of a vase with the cone tracing technique with correct silhouette by highlighting the basic polygonal mesh and by using different depth maps and different depth values



» **Figure 42:** Distortions and holes are due to the quadratic approximation.

Indeed, this space makes it possible to give an idea of the curvature of the surface at each vertex, suddenly, its exploitation makes it possible to adapt the cone tracing so it takes into account the curvature of the surface.

To compare the rendering speed (Frames Per Second), we used high-resolution textures 1024×1024 and 2048×2048, 35 linear steps, 10 binary steps, and

a depth scale equal to 1. Table 1 shows the difference between the approaches discussed in this paper.

The table shows also the views on which the speed calculation is performed. It is clear that the approach by cone rectification is the fastest and relief mapping with correct silhouette remains always less fast compared to the proposed rectifications released during the cone tracing phase. It is also noted that the relaxed technique is always slower than the conservative one because its speed is slowed down by the binary search.

As shown in Table 1 and Table 2, the rendering speed decreases by a means of 37FPS for the viewing ray rectification and by 24FPS for the cone rectification compared to the originals cone tracing techniques. This slowdown is due to the processing concerning the correction of the silhouette. The stability of the images' quality rendered by per-pixel displacement mapping is influenced by the camera position and especially by the viewing angle, indeed, the ray-tracing algorithm uses the camera position to determine the viewing ray along which the searching for the intersection is performed.

Table 1

Comparison of the rendering speed FPS (Frames Per Second) between the discussed approaches with a torus. The approach by the cone rectification is the fastest.




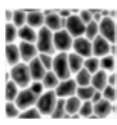
			Conservative Technique			Relaxed Technique			Relief Mapping With Correct Silhouette
Screen 1000×600	Texture	Resolution	Viewing ray rectification	Cone rectification	Without rectification	Viewing ray rectification	Cone rectification	Without rectification	
		1024 ²	210	225	227	198	210	226	202
		2048 ²	115	127	140	107	117	141	105
		1024 ²	230	258	280	211	227	262	197
		2048 ²	140	148	190	130	137	168	117
		Average	173	189	209	161	172	199	155

Table 2

The average FPS (Frames Per Second) number of the decrease in the rendering speed of the two proposed rectifications compared to the original cone tracing techniques.

	Viewing ray Rectification	Cone Rectification
Original Conservative Technique	36	20
Original Relaxed Technique	38	27

In the case of grazing viewing-angles, it is necessary to ensure that the silhouette is rendered correctly and that the iteration number of the ray-tracing algorithm is optimal. One of the solutions to have a stable quality is to determine the iteration number dynamically according to the viewing angle (Ouazzani Chahdi et al., 2018).

One must finally note that the improvements proposed in this article preserve all properties and characteristics of the cone-tracing technique with the latest improvements (Halli et al., 2008).

Conclusion

In this article, we have presented two new cone-tracing algorithms by combining the cone-tracing process with the quadratic approximation. This approximation consists of representing the 3D surface by approximate parameters at each vertex constituting the corresponding mesh.

During the cone-tracing phase, the first algorithm consists of using the parameters of the quadratic surface to

rectify the viewing ray. This rectification makes it possible to know whether the viewing ray pierces or leaves the relief and it is realized after each new displacement along the viewing ray. The second algorithm uses these parameters to rectify the cones parameters (i.e. depth and radius) to be influenced by the characteristics of the approximate surface. This rectification makes it possible to know whether the displacements along the viewing ray make it possible to have or not an intersection and it is realized before each new displacement.

In some cases, the qualities of the rendered images of the two approaches remain almost identical, except for minimal differences. However, when it is about the rendering speed (Frames Per Second), the approach by cone rectification remains the fastest. Also, the rendering quality of the microreliefs and the silhouette depends on the texture resolution and the number of steps of the cone-tracing algorithms. The choice between the conservative and the relaxed technique, the texture resolution, and the number of steps can be made according to the criterion of rendering quality/rendering speed.

The advantage of the cone tracing techniques is that they can be combined with any silhouette correction approach with several possible improvements. Indeed, the processing of the silhouette depends on the ray-tracing algorithm, and how the fragments, belonging to the silhouette, are determined. So, a good coupling makes it possible to have a better algorithm of ray tracing and which supports the treatment of the silhouette. Another advantage of cone tracing is that it is possible to integrate it into the pipeline of new graphics cards since they integrate today the ray-tracing technology.

References

- Baboud, L. & Decoret, X. (2006a) Rendering geometry with relief textures. In: *Proceedings of the 2006 Conference on Graphics Interface, GI '06, 7-9 June 2006, Quebec, Canada*. pp. 195–201.
- Baboud, L. & Décoret, X. (2006b) 'Realistic Water Volumes in Real-Time', In: *Proceedings of the Second Eurographics Conference on Natural Phenomena, NPH'06, 5 September, 2006, Vienna, Austria*. Goslar, Eurographics Association. pp. 25-32.
- Blinn, J. F. (1978) Simulation of wrinkled surfaces. *ACM SIGGRAPH Computer Graphics*. 12 (3), 286–292. Available from: doi: 10.1145/965139.507101
- Blinn, J. F. & Newell, M. E. (1976) Texture and reflection in computer generated images. *ACM SIGGRAPH Computer Graphics*. 10 (2), 266–266. Available from: doi: 10.1145/965143.563322
- Brawley, Z. & Tatarчук, N. (2004) Parallax Occlusion Mapping: Self Shadowing, Perspective-Correct Bump Mapping Using Reverse Height Map Tracing. In: Engel, W. (ed.) *ShaderX3: Advanced Rendering with DirectX and OpenGL*. Hingham, Massachusetts, Charles River Media, pp. 135-154.
- Catmull, E. E. (1974) *A subdivision algorithm for computer display of curved surfaces*. PhD thesis. The University of Utah.
- Chen, Y. C. & Chang, C. F. (2008) A prism-free method for silhouette rendering in inverse displacement mapping. *Computer Graphics Forum*. 27 (7), 1929–1936. Available from: doi: 10.1111/j.1467-8659.2008.01341.x
- Cook, R. L. (1984) SHADE TREES. In: *Proceedings of the 11th annual conference on Computer graphics and interactive techniques, SIGGRAPH'84, 23-27 July 1984, Minneapolis, Minnesota*. New York, Association for Computing Machinery. pp. 223-231.
- Danielsson, P. E. (1980) Euclidean distance mapping. *Computer Graphics and Image Processing*. 14 (3), 227–248. Available from: doi: 10.1016/0146-664X(80)90054-4
- Donnelly, W. (2005) Per-Pixel Displacement Mapping with Distance Functions. In: Pharr, M. (ed.) *GPU Gems 2: Programming Techniques For High-Performance Graphics And General-Purpose Computation*. London, Addison-Wesley Professional, pp. 123–137.
- Dufort, J., Leblanc, L. & Poulin, P. (2005) Interactive Rendering of Meso-structure Surface Details using Semi-transparent 3D Textures. In: *Vision Modeling and Visualization, 16-18 November 2005, Erlangen, Germany*. Amsterdam, IOS Press. pp. 399-406.
- Dummer, J. (2006) *Cone step mapping: An iterative ray-heightfield intersection algorithm*. Available from: <http://scholar.google.com/scholar?hl=en&btnG=Search&q=intitle:Cone+Step+Mapping:+An+iterative+ray-heightfield+intersection+algorithm#0> [Accessed: 20th October 2021]
- Ernst, I., Ruesseler, H., Schulz, H. & Wittig, O. (1998) Gouraud bump mapping. In: *Euro98: 1998 Eurographics/SIGGRAPH on Graphics Hardware, 31 August 1998, Lisbon, Portugal*. New York, Association for Computing Machinery. pp. 47-54. Available from: doi: 10.1145/285305.285311
- Halli, A., Saaidi, A., Satori, K. & Tairi, H. (2008) Per-Pixel Displacement Mapping Using Cone Tracing. *International Review on Computers and Software*. 3 (3), 1–11.
- Halli, A., Saaidi, A., Satori, K. & Tairi, H. (2009) Per-Pixel Extrusion Mapping. *IJCSNS International Journal of Computer Science and Network Security*. 9 (3), 118-124.
- Halli, A., Saaidi, A., Satori, K. & Tairi, H. (2010) Extrusion and revolution mapping. *ACM Transactions on Graphics*. 29 (5), 1–14. Available from: doi: 10.1145/1857907.1857908
- Hirche, J., Ehlert, A., Guthe, S. & Doggett, M. (2004) Hardware accelerated per-pixel displacement mapping. *Graphics Interface*, 153–160.
- Jean, S. P. (2002) A Survey of Methods for Recovering Quadrics in Triangle Meshes. *ACM Computing Surveys*. 34 (2), 211–262. Available from: doi: 10.1145/508352.508354
- Jeschke, S., Mantler, S. & Wimmer, M. (2007) Interactive Smooth and Curved Shell Mapping. In: *Rendering Techniques 2007: Eurographics Symposium on Rendering, EGSR'07, 25-27 June 2007, Grenoble, France*. Aire-la-Ville, Eurographics Association. pp. 351-360
- Kaneko, T., Takahei, T., Inami, M., Kawakami, N., Yanagida, Y., Maeda, T. & Tachi, S. (2001) Detailed Shape Representation with Parallax Mapping. In: *Proceedings of the ICAT 2001, 5-7 December 2001, Tokyo, Japan*. pp. 205–208.
- Kilgard, M. J. (2000) A Practical and Robust Bump-mapping Technique for Today's GPUs. In: *Game Developers Conference, GDC 2000, 9-13 March, San Jose, California*. pp. 1–39.
- Kolb, A. & Rezk-Salama, C. (2005) 'Efficient Empty Space Skipping for Per-Pixel Displacement Mapping. In: *Vision Modeling and Visualization, 16-18 November 2005, Erlangen, Germany*. Amsterdam, IOS Press.
- Lee, S. G., Park, W. C., Lee, W. J., Yang, S. B. & Han, T. D. (2007) An effective bump mapping hardware architecture using polar coordinate system. *Journal of Information Science and Engineering*. 23 (2), 569–588.
- Max, N. L. (1988) Horizon mapping: shadows for bump-mapped surfaces. *The Visual Computer*. 4 (2), 109–117. Available from: doi: 10.1007/BF01905562
- McGuire, M. & McGuire, M. (2005) Steep Parallax Mapping. In: *13D 2005 Posters Session, ACM SIGGRAPH 2005 Symposium on Interactive 3D Graphics and Games, 3-6 April 2005, Washington D.C., Washington*. Available from: <http://casual-effects.com/research/McGuire2005Parallax/mcguire-steep-parallax-poster.pdf> [Accessed 20th October 2021]
- Na, K.-G. & Jung, M.-R. (2008) Curved Ray-Casting for Displacement Mapping in the GPU. In: *Advances in Multimedia Modeling, 14th International Multimedia Modeling Conference - MMM 2008, 9-11 January 2008, Kyoto, Japan*. Berlin,

- Springer, Berlin, Heidelberg. pp. 348–357. Available from: doi: 10.1007/978-3-540-77409-9_33
- Oh, K., Ki, H. & Lee, C. H. (2006) Pyramidal displacement mapping: A GPU based artifacts-free ray tracing through an image pyramid. In: *Proceedings of the ACM Symposium on Virtual Reality Software and Technology, VRST 2006, 1-3 November 2006, Limassol, Cyprus*. New York, Association for Computing Machinery. pp. 75–82. Available from: doi: 10.1145/1180495.1180511
- Oliveira, M. M. (2000) *Relief Texture Mapping*. PhD thesis. University of North Carolina.
- Oliveira, M. M., Bishop, G. & McAllister, D. (2000) Relief texture mapping. *Proceedings of the 27th annual conference on Computer graphics and interactive techniques, SIGGRAPH '00, 23-28 July 2000, New Orleans, Louisiana*. New York, ACM Press/Addison-Wesley Publishing Co. pp. 359–368. doi: 10.1145/344779.344947
- Oliveira, M. M. & Policarpo, F. (2005) *An Efficient Representation for Surface Details*. 55 (51), 1–8.
- Ouazzani Chahdi, A., Ragragui, A., Halli, A. & Satori, K. (2017) Per-pixel displacement mapping using hybrid cone approach. In: *2017 International Conference on Advanced Technologies for Signal and Image Processing (ATSIP), 22-24 May 2017, Fez, Moorocco*. New York, IEEE. pp. 1–4. Available from: doi: 10.1109/ATSIP.2017.8075577
- Ouazzani Chahdi, A., Ragragui, A., Halli, A. & Satori, K. (2018) Dynamic relief mapping. In: *2018 International Conference on Intelligent Systems and Computer Vision (ISCV), 2-4 April 2018, Fez, Morocco*. New York, IEEE. pp. 1–6. Available from: doi: 10.1109/ISACV.2018.8354053
- Pagliaroni, D. W. & Petersen, S. M. (1994) Height Distributional Distance Transform Methods for Height Field Ray Tracing. *ACM Transactions on Graphics*. 13 (4), 376–399. Available from: doi: 10.1145/195826.197312
- Parker, S. G., Friedrich, H., Luebke, D., Morley, K., Bigler, K., Hoberock, J., McAllister, D., Robison, A., Dietrich, A., Humphreys, G., McGuire, M. & Stich, M. (2013) GPU ray tracing. *Communications of the ACM*. 56 (5), 93. Available from: doi: 10.1145/2447976.2447997
- Patterson, J. W., Hoggar, S. G. & Logie, J. R. (1991) Inverse Displacement Mapping. *Computer Graphics Forum*. 10 (2), 129–139. Available from: doi: 10.1111/1467-8659.1020129
- Peercy, M., Airey, J. & Cabral, B. (1997) Efficient bump mapping hardware. In: *Proceedings of the 24th annual conference on Computer graphics and interactive techniques, SIGGRAPH '97, 3-8 August 1997, Los Angeles, California*. New York, ACM Press/Addison-Wesley Publishing Co. pp. 303–306. Available from: doi: 10.1145/258734.258873
- Policarpo, F. & Oliveira, M. M. (2006) Relief mapping of non-height-field surface details. In: *Proceedings of the 2006 symposium on Interactive 3D graphics and games, SI3D '06, 14-17 March 2006, Redwood City, California*. New York, Association for Computing Machinery. pp. 55–62. Available from: doi: 10.1145/1111411.1111422
- Policarpo, F. & Oliveira, M. M. (2007) Relaxed cone stepping for relief mapping. In: Nguyen, H. (ed.) *GPU Gems 3*. London, Addison-Wesley Professional, pp. 409–428.
- Policarpo, F., Oliveira, M. M. & Comba, J. L. D. (2005) Real-time relief mapping on arbitrary polygonal surfaces. In: *ACM SIGGRAPH 2005 Papers, SIGGRAPH '05, 31 July - 4 August 2005, Los Angeles, California*. New York, Association for Computing Machinery, p. 935. Available from: doi: 10.1145/1186822.1073292
- Porumbescu, S. D., Budge, B., Feng, L. & Joy, K. I. (2005) Shell maps. *ACM Transactions on Graphics*. 24 (3), 626–633. Available from: doi: 10.1145/1073204.1073239
- Premecz, M. (2006) Iterative Parallax Mapping with Slope Information. In: *10th Central European Seminar on Computer Graphics, CESC 2006, 24-25 April 2006, Castá-Papiernicka, Slovakia*. Austrian Computer Society.
- Ragragui, A., Ouazzani Chahdi, A., Halli, A. & Satori, K. (2017) Per-Pixel Extrusion Mapping: The correction of the intersection point between the extrusion geometry and the viewing ray. In: *2017 Intelligent Systems and Computer Vision, ISCV 2017, 17-19 April 2017, Fez, Morocco*. New York, IEEE. Available from: doi: 10.1109/ISACV.2017.8054957
- Ragragui, A., Ouazzani Chahdi, A., Halli, A. & Satori, K. (2018a) Per-pixel revolution mapping with rectification of the texture projection. In: *2018 International Conference on Intelligent Systems and Computer Vision, ISCV 2018, 2-4 April 2019, Fez, Morocco*. New York, IEEE. Available from: doi: 10.1109/ISACV.2018.8354056
- Ragragui, A., Ouazzani Chahdi, A., Halli, A. & Satori, K. (2018b) Revolution mapping with bump mapping support. *Graphical Models*. 100, 1–11. Available from: doi: 10.1016/j.gmod.2018.09.001
- Ragragui, A., Ouazzani Chahdi, A., Halli, A. & Satori, K. (2020) Image-based extrusion with realistic surface wrinkles. *Journal of Computational Design and Engineering*. 7 (1), 30–43. Available from: doi: 10.1093/jcde/qwaa004
- Ritsche, N. (2006) Real-time shell space rendering of volumetric geometry. In: *Proceedings of the 4th international conference on Computer graphics and interactive techniques in Australasia and Southeast Asia, GRAPHITE '06, 29 November - 2 December 2006*. New York, Association for Computing Machinery, p. 265. Available from: doi: 10.1145/1174429.1174477
- Shirley, P. & Tuchman, A. (1990) A polygonal approximation to direct scalar volume rendering. In: Péroche, B. & Rushmeier, H. (eds.) *Proceedings of the 1990 Workshop on Volume Visualization, VVS 1990, 10-11 December 1990, San Diego, California*. New York, Association for Computing Machinery, pp. 63–70. Available from: doi: 10.1145/99307.99322
- Sloan, P.-P. J. & Cohen, M. F. (2000) Interactive Horizon Mapping. In: *Eurographics Workshop on Rendering Techniques, EGSR 2000, 26-28 June 2000, Brno*,

- Czech Republic. Vienna, Austria, Springer. pp. 281–286. Available from: doi: 10.1007/978-3-7091-6303-0_25
- Sung Kim, J., Hyun Lee, J. & Ho Park, K. (2001) A fast and efficient bump mapping algorithm by angular perturbation. *Computers & Graphics*. 25 (3), 401–407. Available from: doi: 10.1016/S0097-8493(01)00064-4
- Szirmay-Kalos, L. & Umenhoffer, T. (2008) Displacement Mapping on the GPU — State of the Art. *Computer Graphics Forum*. 27 (6), 1567–1592. Available from: doi: 10.1111/J.1467-8659.2007.01108.X
- Tatarchuk, N. (2006) Dynamic parallax occlusion mapping with approximate soft shadows. *Proceedings of the 2006 symposium on Interactive 3D graphics and games - SI3D '06, 14-17 March 2006, Redwood City, California*. New York, Association for Computing Machinery. pp. 63-69. Available from: doi: 10.1145/1111411.1111423
- Tevs, A., Ihrke, I. & Seidel, H. P. (2008) Maximum mip-maps for fast, accurate, and scalable dynamic height field rendering. In: *Proceedings of the Symposium on Interactive 3D Graphics and Games, I3D08, 15-17 February 2008, New York, New York*. New York, Association for Computing Machinery. pp. 183–190. Available from: doi: 10.1145/1342250.1342279
- Toledo, R., Lévy, B. & Levy, B. (2008) Visualization of Industrial Structures with Implicit GPU Primitives. In: *4th International Symposium on Visual Computing, ISVC08, 1-3 December 2008, Las Vegas, Nevada*. Berlin, Springer-Verlag. pp. 139-150. Available from: doi: 10.1007/978-3-540-89639-5_14
- Toledo, R., Wang, B. & Lévy, B. (2008) Geometry Textures and Applications. *Computer Graphics Forum*. 27 (8), 2053–2065. Available from: doi: 10.1111/J.1467-8659.2008.01185.X
- Wang, L., Wang, X., Tong, X., Lin, S., Hu, S., Guo, B. & Shum, H. Y. (2003) View-dependent displacement mapping. *ACM Transactions on Graphics*. 22 (3). Available from: doi: 10.1145/1201775.882272
- Wang, X., Tong, X., Lin, S., Hu, S., Guo, B. & Shum, H. Y. (2004) Generalized Displacement Maps. In: *Proceedings of the 15th Eurographics Workshop on Rendering Techniques, 21-23 June, Norköping, Sweden*. The Eurographics Association. pp. 227-233. Available from: doi: 10.2312/EGWR/EGSR04/227-233
- Welsh, T. (2004) *Parallax mapping with offset limiting: A per-pixel approximation of uneven surfaces*. Available from: http://page.mi.fu-berlin.de/block/htw-lehre/wise2015_2016/bel_und_rend/skripte/welsh2004.pdf [Accessed 20th October 2021]
- Yerex, K. & Jagersand, M. (2004) Displacement Mapping with Ray-casting in Hardware. In: *ACM Siggraph 2004 Sketches, SIGGRAPH '04, 8-12 August 2004, Los Angeles, California*. New York, Association for Computing Machinery. p. 2000. Available from: doi: 10.1145/1186223.1186410



